Electronic and Optoelectronic Devices based on 2-Dimensional Crystals

By

Haijie Tan

Supervised by

Professor Jamie H. Warner

Submitted in conformity with the requirements for the degree of

Doctor of Philosophy in Materials Science

Department of Materials

The Queen's College

University of Oxford



July 2017

Copyright © by Haijie Tan

Declaration

The material contained within this thesis has not previously been submitted for a degree at the University of Oxford or any other university. The research reported within this thesis has been conducted by the author unless indicated otherwise.

Copyright Notice

The copyright of this thesis rests with the author. No quotation from it should be published without the prior written consent of the author, and any information derived from it should be acknowledged.

Abstract

Two dimensional crystals including graphene and monolayer transition metal dichalcogenides such as molybdenum disulphide (MoS_2) and tungsten disulphide (WS_2) have attracted widespread attention for both basic scientific interest and potential in device applications. In this thesis, we investigate the electronic and optoelectronic devices based on 2D crystals grown using chemical vapour deposition.

In our study on graphene transistors, we show that surface charge transfer between graphene and vertically stacked WS_2 causes local modulation to doping levels of graphene, and can be further stimulated by photo-irradiation. We demonstrate the formation of an isotype junction in graphene, where two lateral sections of a graphene ribbon contain different dopant concentrations.

Ultrathin lateral photodetectors of 2 nm thickness are made by incorporating graphene as electrodes and WS_2 as active semiconductor. We show that graphene is different to conventional metal electrodes due to the finite density of states from the Dirac cones of the valence and conduction bands, which enables modulation of photoresponsivity through electrostatic gating and light input control.

We demonstrate photodetectors with laterally spaced graphene electrodes and vertically stacked WS_2/MoS_2 as active light-adsorbing component, achieving photoresponsivity as high as 2340 A W^{-1}. We observe in hybrid WS_2/MoS_2 photodetector massive enhancements in photogain compared to homobilayer and monolayer devices of MoS_2 or WS_2 due to efficient charge transfer between WS_2 and MoS_2 and long carrier lifetimes. Our results show that high performance photodetectors using all 2D materials can be realized using graphene electrodes and TMD heterostructures with type-II band alignment.

Acknowledgements

Scientific research may often be carried in solitude, but many hands helped moved this project forward. Since embarking on my journey as a DPhil graduate student in October 2013, I am blessed with the opportunity to interact with the brilliant individuals who helped me grow in my academic, professional and personal capacity. Here I thank the people who played instrumental roles throughout my time in Oxford, without whom this thesis would not be possible.

First and foremost, to my supervisor, Prof. Jamie Warner, for whom I have immense respect. His broad vision, acute observations and adept experimental skills never cease to inspire me. His sage advices and patient guidance have been as formative to my character as the DPhil itself. As Jamie shepherded my growth from a fresh science graduate to a professional researcher, he also models the kind of leader I aspire to become: where influence is based as much on supporting and empowering others as sharing my own work. It has been my great fortune and honour to work in his lab, and for this I will forever be grateful.

All my colleagues at the Nanostructured Materials Group have made my time here both productive and incredibly enjoyable. I would like to especially thank Dr. Ye Fan and Dr. Chit Siong (Aaron) Lau for their generous sharing of invaluable experiences that I may otherwise have had to learn the hard way. Ye has laid much of the groundwork in electronic applications and taught me almost everything I know about device fabrication. His vast knowledge, inquisitive spirit and sense of humour were also the source of countless enlightening and joyous moments over the coffee tables we shared. Aaron was first to introduce me to coding, which resulted in some gratifying experiences of automating

laborious and programmable works. The meaningful discussion we had also helped crystallize several of my research projects.

I also thank Dr. Youmin Rong, Dr. Shanshan Wang, Wenshuo Xu, Yuewen Sheng, Yingqiu Zhou and Qu Chen for their generous provision of high quality samples during the course of my project. Every novel electronic devices that were made in this thesis stems from their focused dedication in developing and optimising growth methods of novel 2D crystals. At the same time, I thank all other colleagues, including Dr. Alex Robertson, Dr. Kuang He, Dr. Zhengyu He, Dr. Jakyung Lee, Thomas Samuels, Xiaochen Wang, Sha Li, Hefu Huang, Martin Tweedie, Ren-Jie Chang, Si Zhou and Tongxin Chen for their kind support throughout these years. I also extend my gratitude to Mr. Paul Pattinson, who has successfully maintained the world-class cleanroom facilities which made the envisioned nano-devices a reality.

I would like to acknowledge Yayasan Khazanah for providing me with the scholarship to pursue my DPhil studies. I thank the administrative team for their orchestrated effort in organising annual workshops, gatherings and career engagement sessions, all of which helped me grow personally and forge valuable relationships back home in Malaysia.

Finally, I dedicate this thesis to my family. To my beloved partner Qu Chen, for energizing me with her spirit, quiet understanding and unyielding support. To my parents, Tan Thuan Ngee and Lua Eng Fong, as well as my sister, Haishan Tan, for being the unwavering pillars of my life. I am nothing without their unconditional love and the values they have instilled in me. They are the single most important thing in my life, and every accomplishment I achieve, I do it for them.

Publications

Presented here is a list of works published during the course of this DPhil project. First authored publications are discussed in Chapters 4-6. Some of the co-author works listed here lie beyond the purview of this thesis.

Chapter 4

Tan, H.; Fan, Y.; Rong, Y.; Porter, B.; Lau, C. S.; Zhou, Y.; He, Z.; Wang, S.; Bhaskaran, H.; Warner, J. H. Doping Graphene Transistors Using Vertical Stacked Monolayer WS_2 Heterostructures Grown by Chemical Vapor Deposition. *ACS Appl. Mater. Interfaces* **2016**, *8*, 1644–1652.

Chapter 5

Tan, H.; Fan, Y.; Zhou, Y.; Chen, Q.; Xu, W.; Warner, J. H. Ultrathin 2D Photodetectors Utilizing Chemical Vapor Deposition Grown WS_2 With Graphene Electrodes. *ACS Nano* **2016**, *10*, 7866–7873.

Chapter 6

Tan, H.; Xu, W.; Sheng, Y.; Lau, C. S.; Fan, Y.; Chen, Q.; Tweedie, M.; Wang, X.; Zhou, Y.; Warner, J. H. Lateral Graphene Contacted Vertically Stacked WS_2/MoS_2 Hybrid Photodetectors with Large Gain. *Adv. Mater.* **2017**, *29*, 1702917.

Co-Author

(1) Fan, Y.; He, K.; Tan, H.; Speller, S.; Warner, J. H. Crack-Free Growth and Transfer of Continuous Monolayer Graphene Grown on Melted Copper. *Chem. Mater*. **2014**, *26*, 4984–4991.

(2) Rong, Y.; Fan, Y.; Leen Koh, A.; Robertson, A. W.; He, K.; Wang, S.; Tan, H.; Sinclair, R.; Warner, J. H. Controlling Sulphur Precursor Addition for Large Single Crystal Domains of WS_2. *Nanoscale* **2014**, *6*, 12096–12103.

(3) Fan, Y.; Zhou, Y.; Wang, X.; Tan, H.; Rong, Y.; Warner, J. H. Photoinduced Schottky Barrier Lowering in 2D Monolayer WS_2 Photodetectors. *Adv. Opt. Mater.* **2016**, *4*, 1573–1581.

(4) Sheng, Y.; Tan, H.; Wang, X.; Warner, J. H. Hydrogen Addition for Centimeter-Sized Monolayer Tungsten Disulfide Continuous Films by Ambient Pressure Chemical Vapor Deposition. *Chem. Mater.* **2017**, *29*, 4904–4911.

Contents

Chapter 1 Introduction 1

1.1 Project Aims 1
1.2 The Scope of this Thesis 1

Chapter 2 Literature Review 3

2.1 Introduction 3
2.2 Fundamentals of Field-effect Transistors 4
2.3 Production Methods of 2D Crystals 8
2.3.1 Exfoliation 8
2.3.2 Chemical Vapour Deposition 9
2.4 Electronic Properties of 2D Crystals 11
2.4.1 Graphene 12
2.4.2 Transition Metal Dichalcogenides 15
2.5 Device Applications of 2D Crystals 17
2.5.1 Graphene FETs 17
2.5.2 TMD-based FETs 19
2.5.3 TMD-based Photodetectors 26

Chapter 3 Device Fabrication and Characterization Techniques 36

3.1 Introduction 36
3.2 Crystal Growth and Device Fabrication 36
3.2.1 Chemical Vapour Deposition of 2D Crystal 36
3.2.2 Transfer Techniques 37
3.2.3 Electron-Beam Lithography and Photolithography 38
3.2.4 Metal Evaporation 40
3.2.5 Plasma Etching 40
3.3 Characterization and Measurements 41
3.3.1 SEM 41
3.3.2 Photoluminescence and Raman 42
3.3.3 Atomic Force Microscopy 45
3.3.4 Electrical and Opto-electrical Measurements 46

Chapter 4 Doping Graphene Transistors Using Vertical Stacked Monolayer WS_2 Heterostructures Grown by Chemical Vapour Deposition 48

4.1 Introduction 48
4.2 Results and Discussions 50
4.2.1 Device Fabrication of Graphene FETs with Vertically Stacked WS_2 50
4.2.2 Raman & PL Characterization 51

4.2.3 Field Effect Measurements of Graphene FETs 54
4.2.4 Electronic Model of Laterally Separated Graphene FETs 56
4.2.5 Photo-induced Charge Transfer of Graphene-WS_2 Interface 59
4.3 Conclusion 60
4.4 Contribution Statement 61
Chapter 5 Ultrathin 2D Photodetectors Utilizing Chemical Vapour Deposition Grown WS_2 with Graphene Electrodes 62
5.1 Introduction 62
5.2 Results and Discussion 63
5.2.1 Device Fabrication of graphene-WS_2-graphene Photodetectors 63
5.2.2 Raman & PL Characterization 65
5.2.3 Opto-electrical Characterizations of graphene-WS_2-graphene Photodetectors 67
5.2.4 Comparative Study with Au-WS_2-Au Photodetectors 78
5.3 Conclusion 79
5.4 Contribution Statement 80
Chapter 6 Graphene-contacted WS_2/MoS_2 Hybrid Photodetectors with Large Gain Utilizing Interlayer Charge Transfer 81
6.1 Introduction 81
6.2 Results and Discussions 83
6.2.1 Device Fabrication 83
6.2.2 Raman and PL Analysis of WS_2/MoS_2 Heterostructure 85
6.2.3 Opto-electrical Characterizations 86
6.2.4 Figures of Merit Comparison 89
6.2.5 Gate dependence study 91
6.2.6 Cause of Large Gain in Hybrid graphene-WS_2/MoS_2-graphene Photodetectors 94
6.3 Conclusion 97
6.4 Contribution Statement 97
Chapter 7 Conclusion and Future Outlook 98
7.1 Thesis Summary 98
7.2 Future Outlook 99
References 101

Chapter 1 Introduction

1.1 Project Aims

This doctorate project aims to investigate the electronic properties of two-dimensional (2D) crystals, through the understanding of the Physics that governs their interfaces and the mechanisms of photocurrent generation. It involves implementing new types of device structures using semi-metallic graphene and 2D transition metal dichalcogenides (TMDs), such as MoS_2 and WS_2, grown by chemical vapour deposition, for highly efficient electronic and optoelectronic devices.

1.2 The Scope of this Thesis

This thesis includes the research findings over the time span of four years of DPhil degree at the Materials Department, University of Oxford. It starts with a literature review in Chapter 2 that provides an overview of field-effect transistors and the relevant properties of 2D crystals including graphene, MoS_2 and WS_2, and reviews the progress of device applications of 2D crystals in electronics and optoelectronics applications. Methodology in Chapter 3 covers the characterisation and device fabrication techniques essential for making devices based on 2D crystals.

Chapter 4 summarises my work on graphene field-effect transistors doped by WS_2 domains. It reports the n-type doping of graphene transistors due to surface charge transfer from WS_2, as is evident through various characterizations and modelling results. The interlayer charge transfer, which can be further induced by illumination on the graphene-WS_2 heterostructure, plays an important role for facilitating high photoconductive gain found in the 2D-photoconductors described in following chapters. Chapter 5 demonstrates all-2D lateral photodetectors that use graphene as contacts, and WS_2 as the active

photodetector. Monolayer and bilayer WS_2 devices, as well as graphene-contacted- and gold-contacted-devices, are compared. Chapter 6 introduces photodetectors that are based on graphene lateral contacts sandwiched by a WS_2/MoS_2 vertical stack. The significant photoresponsivities found in the hybrid graphene-WS_2/MoS_2-graphene photodetectors are compared with other 2D photodetectors. The cause of photoconductive gain is discussed by looking into the charge transfer between WS_2 and MoS_2 and the photogating mechanism at the graphene-TMD interface.

The final chapter summarises the DPhil thesis and concludes by addressing the opportunities and challenges in future studies of devices based on 2D crystals.

Chapter 2 Literature Review

2.1 Introduction

Graphene is a single-layer of sp^2-hybridized carbon atoms packed in a hexagonal arrangement.[1] Since its discovery in 2004,[2] this 2D material has garnered wide interest because of its unique material properties unfound in its 3D counterparts.[3] Despite its atomic thinness, graphene exhibits extra-ordinary mechanical property with a breaking strength of 42 N m^{-1} (corresponding to a Young's modulus of 1.0 TPa),[4] making it one of the strongest materials ever measured. It is, however, the exceptional electronic properties that have prompted the numerous investigations of graphene's device applications. For example, electrons are found to behave as massless relativistic particles on a graphene sheet,[5] resulting in a ballistic transportation with carrier mobilities exceeding 100,000 $cm^2V^{-1}s^{-1}$ at room temperature.[6,7]

Although graphene features many interesting properties, it lacks a band gap necessary for digital electronic applications.[8] Engineering a band gap in graphene often involves high operating voltage[9] and results in compromised mobilities.[10] After the discovery of graphene, the scope of research soon extended to other 2D layered materials which includes hexagonal boron nitride (h-BN), TMDs and black phosphorous.[11–14] Together, these 2D materials are seen as building blocks for a new generation of nanoscale devices based on van der Waals (vdW) heterostructure.[15–17] Among them, TMDs isolated in their monolayer form have been intensively studied owing to their natural abundance and sizable band gaps.[18] For example, monolayer MoS_2 and WS_2 have direct band gaps of around 1.9 eV and 2.1 eV respectively,[19] and exhibit strong light-matter interactions. These features make them appealing for both electronic and optoelectronic applications.[20]

Over the past few decades, the microelectronics industry has relentlessly driven down the cost and size of transistor components, following a trend known as Moore's Law.[21] This has led to circuit features as small as 14 nm as of 2016.[22] However, on a nanoscale, sustaining the same pace of miniaturization becomes much more challenging. It is speculated that the future of microelectronics will have to adopt new device architectures and alternative materials which could complement or even replace Si on a sub-10 nm scale.[23] Following the view expressed by Schwierz,[24] alternative materials are expected to meet the following four requirements for digital electronics applications: 1) wide enough band gap, combined with excellent carrier transport and high thermal conductivity; 2) compatibility with conventional microfabrication processes; 3) high contact quality with dielectrics; and 4) low contact resistance. Since the discovery of 2D materials, it has been of great interest to investigate whether they fit the aforementioned requirements to qualify as potential candidates for microelectronics beyond Si.

This Chapter is devoted to review the developments in electronics and optoelectronics based on graphene and TMDs. Based on the thesis subject, it starts by introducing the fundamentals of conventional field-effect transistors (FETs), including their working mechanisms, characteristics and scaling limitations. This is then followed by a review on the production, electronic properties, and device applications of 2D graphene and TMDs.

2.2 Fundamentals of Field-effect Transistors

Metal-oxide-semiconductor FETs (MOSFETs) are among the most widely used electronic devices in digital integrated circuits. A MOSFET operates as an electric switch, utilising a gate electrode potential (V_G) to control the conductivity of the semiconductor between the source and drain electrodes. **Figure 2.1** gives a schematic view of a

conventional n-channel MOSFET. In this device, source and drain electrodes are deposited on n-type Si regions on a p-type Si substrate. When a $+V_G$ is applied, electrons within the semiconducting channel are attracted by the gate, forming an inversion layer that enables charge carrier transport. When the applied gate voltage is larger than the threshold voltage V_{th}, an inversion layer connects the source and the drain, allowing conduction through the channel and thus switching on the transistor.

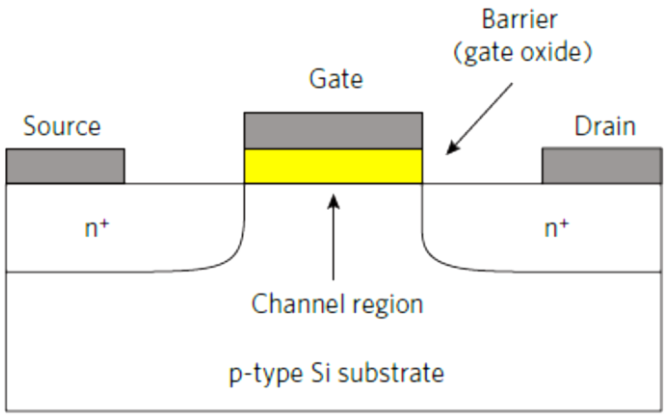


Figure 2.1 Cross-section of an n-channel Si MOSFET. Reproduced with permission.[24] Copyright 2010, Macmillan Publishers Ltd.

Ideally, MOSFETs switch would have no current flow along the channel in the OFF state and no resistance in the ON state; the perfect switch would also be capable of instant transition between the OFF/ON states. In reality, MOSFETs are far from ideal, exhibiting non-zero off-currents and non-negligible operation resists. Furthermore, the switching does not occur at a clear-cut threshold but rather takes place gradually within a voltage range. In these transistors, I_{on}/I_{off} ratio, which is the ON state current I_{on} divided by the OFF state current I_{off}, is regarded as the maximum current modulation factor possible.

Figure 2.2 shows the typical output characteristics of a MOSFET at different gate voltages. While the transistor is switched on ($V_G > V_{th}$), the channel current initially increases linearly with V_{ds}, following the Ohm's law. As V_{ds} continues to increase, the gate potential

difference within the channel reduces from V_G at the source to $V_G - V_{ds}$ at the drain. Once $V_G - V_{ds} \leq V_{th}$, the inversion layer near the drain end is no longer sustained, and the point where the inversion charge is nearly zero is known as the "pinch off" point.[25] Beyond this point the drain current becomes independent of V_{ds} and saturates at $I_{ds(sat)}$, with only a slight increase due to various effects such as channel length modulation and drain-induced barrier lowering.

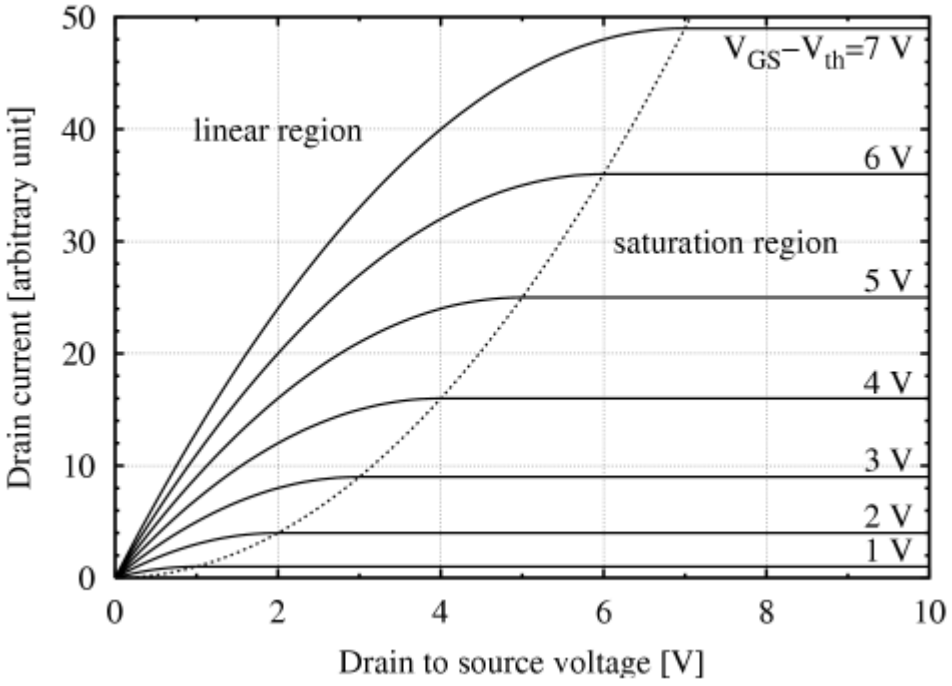


Figure 2.2 *I-V* characteristics of MOSFETs. Reproduced with permission.[25] Copyright 2006, John Wiley & Sons.

Figure 2.3 shows a typical n-type transistor's I_{ds} as a function of gate bias V_G. Two curves with identical data are plotted on a linear scale (blue curve; y axis, right) and a logarithmic scale (red curve, y axis, left). Before the gate voltage reaches the threshold voltage V_{th}, the drain current increases exponentially with V_G on a logarithmic scale with a slope known as the subthreshold slope. The inverse of the subthreshold slope is often referred to as subthreshold swing (*SS*), given in units (mV/decade). A typical value of a scaled MOSFETs *SS* at 300 K is about 70 mV/decade, which means that a 70 mV increase in gate voltage is required to raise the subthreshold drain current by tenfold. A small SS is

desirable as it improves the I_{on}/I_{off} ratio and lowers the power consumption of a chip in the idle state. The subthreshold swing can be expressed as $SS = \ln(10)\frac{kT}{q}(1 + \frac{C_d}{C_{ox}})$,[26] where C_d is the depletion layer capacitance, C_{ox} is the gate-oxide capacitance, and $\frac{kT}{q}$ is the thermal energy divided by the elementary charge. To determine the minimum *SS* of a conventional device, simply let $C_{ox} \rightarrow \infty$, which yields 60 mV/decade at room temperature (300 K). Thus a *SS* of 60 mV/decade is generally considered as the fundamental limit in conventional MOSFETs.

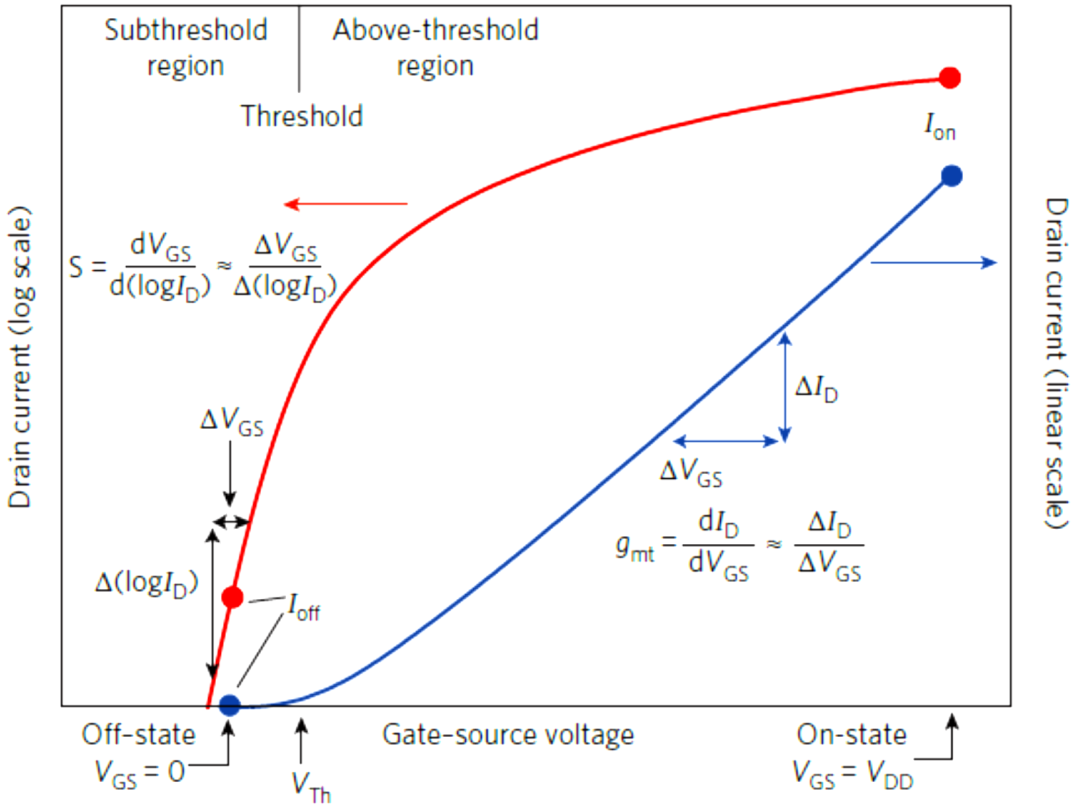


Figure 2.3 Drain current as a function of gate voltage. Reproduced with permission.[24] Copyright 2010, Macmillan Publishers Ltd.

2.3 Production Methods of 2D Crystals

Individual layer of graphene and TMDs can be obtained using top-down or bottom-up approaches. The top-down strategy commonly involves exfoliation from the bulk layered crystals, whilst bottom-up approach grows the crystals through vapour deposition. In this section, an overview of the techniques within these two categories will be given.

2.3.1 Exfoliation

2.3.1.1 Mechanical Exfoliation

Graphene was first realised using the "scotch-tape" method,[2] which involves peeling off layers of carbon atoms from graphite using an adhesive tape. The cleaving process is repeated over again until all that remains are one or several layer(s) of graphite. Mechanical exfoliation is now generally applied to produce 2D crystals beyond graphene.[27–29] This method yields high quality layers free from dopants introduced from chemical processes. Therefore, mechanical exfoliation is ideal for studies on intrinsic physical properties of 2D materials and the fabrication of proof-of-concept devices. However, the disadvantages of this method are its improbable industrial scaling and limited crystal sizes.

2.3.1.2 Liquid Exfoliation

Sonicating bulk layered materials in liquids provides a promising route to obtain large quantities of exfoliated nanosheets. The nanosheets dispersed in solution can be easily applied in material coating, inkjet printing, and the making of composites or hybrids using a mix of dispersed materials. Direct sonication of layered materials in common solvents such as N-methylpyrrolidone (NMP) and dimethylformamide (DMF) have been reported to obtain few-layer graphene, BN, MoS_2 and WS_2.[30–32] These direct sonication methods require solvents with high surface energies to overcome the cohesive energy between the adjacent crystal layers, and face difficulty for high-yield production of monolayer flakes.

One of the most effective ways to improve yield is through intercalation of the crystals using ions.[33] The typical procedure involves soaking bulk TMD powder in lithium-containing solution, followed by exposing the intercalated material in water.[34,35] A vigorous reaction of water with lithium between the layered material produces H_2 gas and separates the layers more easily. Further optimization has been made for faster and more controllable lithium intercalation by using a lithium foil anode and TMD-containing cathode.[36] Intercalation in this method only takes place during galvanic discharge within the electrochemical cell, permitting the process to be monitored and controlled. The use of Li-ion exfoliation gives a higher yield to quality monolayer nanosheets.[34] However, the flammability of Li compounds, as well as the increasing price of Li resources beg for alternative intercalants.[18] In general, liquid exfoliation methods can be useful for solution-based or printable electronics, yet it may unavoidably introduce extrinsic defects or alter crystal structure of thin TMDs, and require additional post-treatment steps for lattice reconstruction.[34]

2.3.2 Chemical Vapour Deposition

As discussed previously, the mechanical exfoliation of layered materials may produce high quality crystals, but it is difficult to scale up due to its labour-intensiveness and low-yield nature. Liquid-exfoliation may lead to a higher yield, but it still faces limitations in its solution-based processes, smaller crystal sizes and varying qualities. For these reasons, bottom-up approach using chemical vapour deposition (CVD) may be the only scalable route in obtaining high-quality, large-area and continuous 2D crystals necessary for wafer-scale device fabrications.[37] All 2D crystals used within the scope of this thesis were made with CVD, and the detailed processes for growing monolayer graphene, MoS_2 and WS_2 will be described in Chapter 3.

2.3.2.1 CVD Synthesis of Monolayer Graphene

Wafer-scale synthesis of graphene by CVD has been demonstrated on various substrates including SiC,[38] Pt,[39] Ni,[40–42] Pd,[43] and Cu.[44,45] Among them, copper is the most commonly-used catalyst substrate for growing large-area, high-quality monolayer graphene.[44] There are two main growth mechanisms during a CVD growth process. The first is a "segregation" process in which diffused/dissolved carbon atoms within a heated substrate start to segregate to the surface and form graphene sheets when cooled down.[41,42] Another mechanism relies on the "absorption" process on the substrate surface which makes use of the nucleation and lateral growth of carbon atoms as a result of decomposition of catalysed hydrocarbon (usually methane) under high temperature.[43–45] With suitable growth conditions, graphene growth can be self-limiting, under which the growing process terminates once the substrate is covered by a single layer of carbon atoms, namely, monolayer graphene.[46]

2.3.2.2 CVD Synthesis of MoS_2 and WS_2

CVD methods have also been utilised for obtaining large-area ultrathin TMD crystals with controllable thickness and domain sizes. Monolayer TMDs usually come in a typical triangular morphology, with side lengths of the triangular domains reaching over 100 μm.[47] The reported methods can be classified into three main categories based on their growth mechanisms.

The first is the vaporization and decomposition of metal and chalcogen precursors, followed by the deposition of TMD on a substrate.[48–50] Pioneering work based on this mechanism has been demonstrated by Lee *et al.* in 2011 for MoS_2 growth. MoO_3 and S powders were used as reactants to synthesize MoS_2 directly on SiO_2 substrates.[48] Graphene-like molecules such as reduced graphene oxide, perylene-3,4,9,10-tetracarboxylic acid

tetrapotassium salt (PTAS) and perylene-3,4,9,10-tetracarboxylic dianhydride (PTCDA) were used to pre-treat the SiO_2 substrate for promoting growth of MoS_2.[48] Further progress was made when Lee *et al.* applied a similar technique to other substrates including quartz and sapphire.[49] Around the same time, Zande *et al.* [50] developed a method to grow MoS_2 on ultraclean SiO_2 substrate without seeding pre-treatment, revealing the critical roles that surface cleanliness and smoothness of substrate play in CVD-growth of TMD crystals.

The second mechanism is based on direct sulfurization of metal films. In 2012, Zhan *et al.* accomplished the growth of MoS_2 thin film by direct transformation of Mo thin layer into MoS_2 by reacting with sulphur under elevated temperature.[51] In this way, the obtained MoS_2 film is determined by the thickness of the deposited Mo film, which is precisely controlled by an e-beam evaporator. This provides a way for preparing large-area high-quality MoS_2 films with controllable thicknesses.[51]

Thirdly, CVD growth can be based on the conversion of metal oxide to metal disulphide through sulfurization. Synthesis of thin-layer MoS_2 was achieved on sapphire substrate with thermally deposited MoO_3 thin films with desired thickness. Similar to the previous approaches, sulphur was introduced into the furnace under high temperature over 1000 ^oC for sulfurization which results in a few-layer MoS_2 film.[52]

2.4 Electronic Properties of 2D Crystals

With single-atomic-layer thickness, 2D crystals take up very little space in the vertical direction compared with conventional channels, allowing more compact designs of integrated circuits. As ultra-thin-body semiconductors, they are also expected to have resilience to short-channel effects, as suggested by several theoretical simulation studies,[53,54] which could enable further miniaturisation of transistors. In the following section, the properties of graphene and TMDs relevant to FET applications are introduced.

2.4.1 Graphene

2.4.1.1 Band gap Engineering

The discussion on electronic structure of graphene dates back to 1947 by Wallace, who first revealed the semi-metallic behaviour of such material.[55] The cone-shaped valence and conduction bands of graphene touch at the six K points of the Brillouin zone, known as the Dirac points. Therefore, graphene is usually described as a zero-gap semiconductor.[1,24] This gapless nature of graphene is often seen as a major drawback that limits graphene's application in logic devices, which prompted much efforts in the band gap engineering of graphene.

A possible route to open a band gap in graphene is to constrain it in one dimension, forming a graphene nanoribbon. This confinement in width is anticipated to lead to a splitting in the original 2D energy dispersion of graphene into multiple 1D modes. Some of these 1D modes do not cross the Dirac point thus resulting in a finite gap.[56] First experimental evidence was shown by Han *et al.* demonstrating band gaps of 300-400 meV for graphene nanoribbons with width under 15 nm.[10] The size of such band gaps points to a promising step towards FET applications.[24,57] Smaller widths in these nanoribbons are found to result in larger band gaps. This inverse relationship between the ribbon width and the band gap has been predicted theoretically and verified experimentally.[24,58–60] One major challenge associated with fabricating graphene nanoribbons is that the edges of the ribbons are generally not perfect, which causes uncertainty in device performances. To address this issue, Jiao *et al.* devised a process to 'unzip' carbon nanotubes, which reportedly leads to nanoribbons with more uniform width and reduced roughness.[61]

Another approach for the band gap engineering is by applying a vertical electric field to bilayer graphene. As shown in **Figure 2.4** (iii), intrinsic bilayer graphene is also gapless,

with the two bands featuring a parabolic shape near the K point. When a perpendicular electric field is applied, a band gap opens with the size depending on the electric field. This effect enables a gate-tunable band gap of 200-250 meV in bilayer graphene.[62,63] An I_{on}/I_{off} ratio of 100 under room temperature has been reported by using this method.[64]

Other options demonstrated for effective band gap opening include applying strain to graphene[65,66] and beam ionization of graphene.[67]

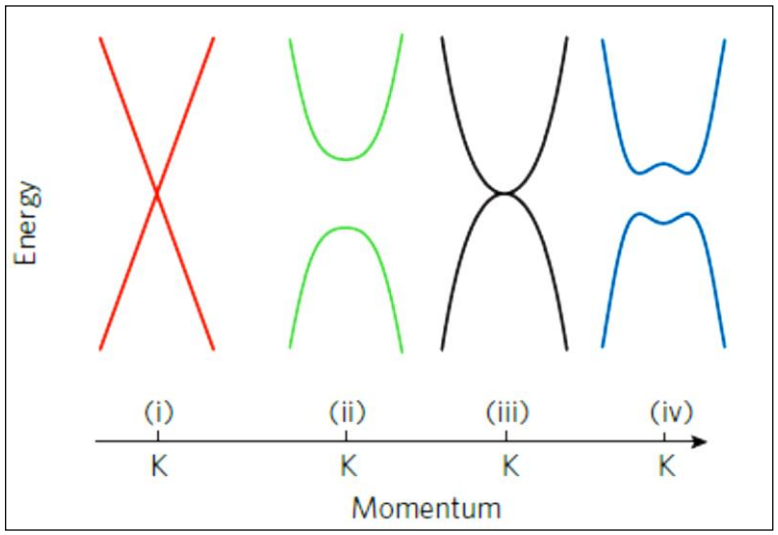


Figure 2.4 Band structure around the K point for (i) large area graphene (ii) graphene nanoribbons (iii) unbiased bilayer graphene and (iv) bilayer graphene with perpendicular electric field. Reproduced with permission.[24] Copyright 2010, Macmillan Publishers Ltd.

2.4.1.2 Carrier Transport

Mobility

Charge carriers on graphene possess small effective mass,[5] resulting in high mobility which is extremely attractive for electronic applications. For graphene that are mechanically exfoliated onto SiO_2 substrates, measured mobilities are reported to be around 10,000 $cm^2 V^{-1} s^{-1}$, with an upper limit of 70,000 $cm^2 V^{-1} s^{-1}$.[68,69] It is predicted that without charged impurities and ripples in graphene, carrier mobility can be improved up to 200,000 $cm^2 V^{-1} s^{-1}$.[70] An example of this is the use of atomically flat and chemically inert h-BN as a

substrate/encapsulating layer for graphene, which successfully enhanced graphene's carrier mobility to over 500,000 $cm^2 V^{-1} s^{-1}$.[7] So far, suspended graphene has yielded the highest mobility of around 2×10^6 $cm^2 V^{-1}s^{-1}$.[71]

As previously discussed, it is possible to open a band gap in graphene by fabricating graphene nanoribbons. However, a general phenomenon associated with the opening of band gap is the degradation of mobility. This inverse relationship is because of the shape change of the valence and the conductance band when graphane's dimension is reduced. Shown in Figure 2.4(i-ii), graphene nanoribbons have more parabolic rather than cone-shaped bands, which is associated with larger carrier effective mass and lower mobility.[72,73] Whilst a 14 nm wide graphene nanoribbon has a mobility of 1500 $cm^2 V^{-1} s^{-1}$,[10] the mobility of ribbons with a 1-10 nm width drops to around 200 $cm^2 V^{-1} s^{-1}$.[9] It is predicted that graphene nanoribbons with a band gap of over 500 meV will have no significant advantage over silicon (~400 $cm^2 V^{-1} s^{-1}$).[60]

High Field Transport

As transistors continue to scale down to a few nanometers, a high electric field across the channel is expected even at a low source-drain voltage. At such high fields, the peak or saturation velocity, rather than mobility, is normally used for evaluating carrier transport.[24] Experimental study done by Meric *et al.* reported high saturation velocities up to 5.5×10^7 cm/s in graphene,[74] in accord to theoretical predictions based on Monte Carlo simulations.[75,76] In terms of saturation velocity, graphene outperforms conventional Si, with a saturation velocity of around 1×10^7 cm/s,[77] and is comparable to other promising semiconductor candidates such as GaN, GaAs and InAs, with reported peak velocities of 6×10^7, 4×10^7 cm/s and 3×10^7 cm/s respectively.[78,79].

2.4.2 Transition Metal Dichalcogenides

2.4.2.1 Crystal Lattice Band Structure

TMDs appear in the form of MX_2, with transition metal M from group IV (Ti, Zr, Hf), group V (V, Nb, Ta) or group VI (Mo, W) covalently bonded with chalcogen X (S, Se, Te) (**Figure 2.5**a). TMD layers are weakly bounded by vdW interactions, each consisting transition metal atoms sandwiched between two layers of chalcogenide atoms, forming a X-M-X structure in vertical direction.[80] Bulk TMDs exhibit diverse electronic properties, ranging from metals to semiconductors to insulators, depending on the metal type. For example, MoX_2 and WX_2 compounds are semiconducting while NbX_2 and TaX_2 are metallic.[81] The diversity in TMDs properties arises from the differently filled non-bonding d bands of the transition metals.[80,81] Monolayer TMDs usually exhibit only two polymorphs, trigonal prismatic (2H) or octahedral (1T) phase.[81] MoS_2 and WS_2, which are the main focus of this thesis, are most commonly found in 2H phase (Figure 2.5b-c).

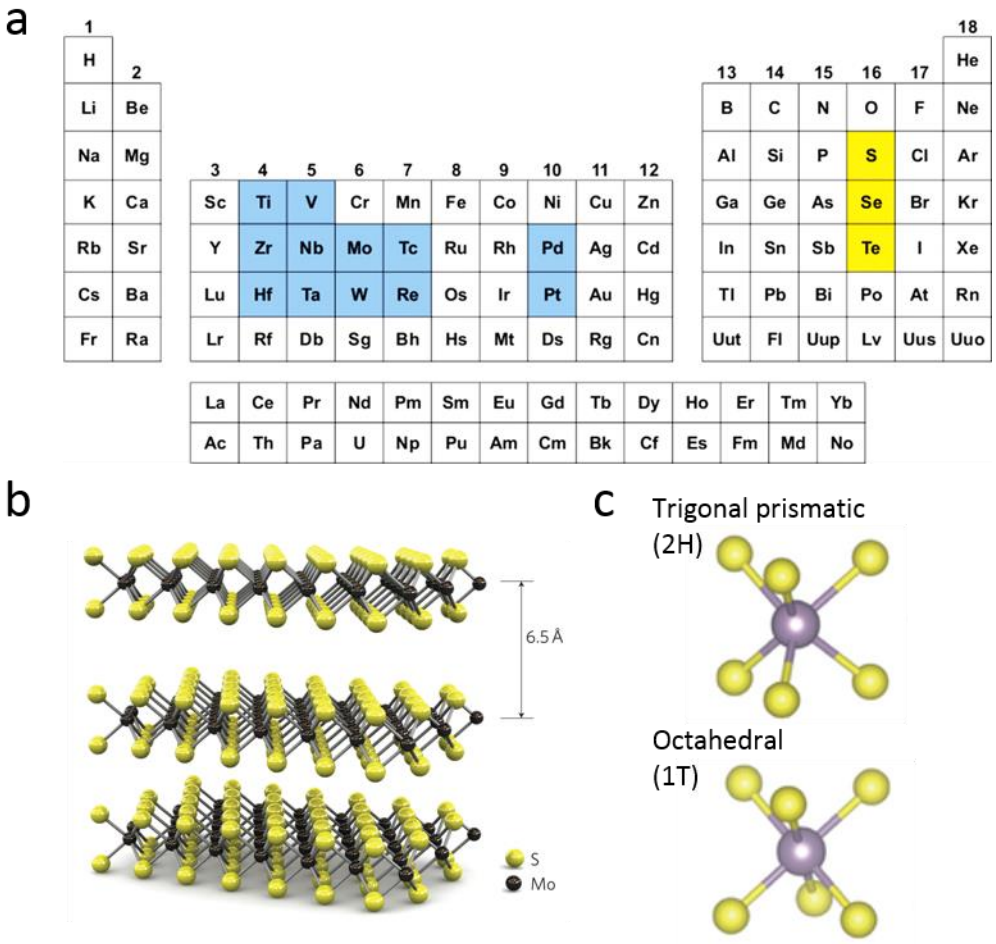


Figure 2.5 Crystal Structure of TMDs. (a) Periodic table with highlighted transition metal (blue) and chalcogen (yellow) elements that can form layered MX_2 compounds. Reproduced with permission.[82] Copyright 2015, Royal Society of Chemistry. (b) Schematic of atomic model of layered MoS_2 Reproduced with permission.[83] Copyright 2011, Macmillan Publishers Ltd. (c) Schematic of two common TMD crystal structures, trigonal prismatic (top) and octahedral configuration (bottom). Reproduced with permission.[81] Copyright 2013, Macmillan Publishers Ltd.

One prominent feature of TMDs is the layer dependence of their band structure. The band structures calculated from density functional theory (DFT) of both MoS_2 and WS_2 are shown in **Figure 2.6**.[84] Whilst in bulk form MoS_2 and WS_2 have indirect band gaps of ~1.2 eV, in monolayer form they exhibit direct band gaps of 1.9 eV and 2.1 eV respectively. According to theoretical calculations, the valence band maximum (VBM) for bulk TMDs is at Γ point and gradually shifts to K point in monolayer TMDs, while the conduction band minimum (CMB) shifts from mid-way between Γ and K points to K point.[84] A direct band gap allows the electron-hole pair recombination process to occur without the involvement

of phonons. Therefore, a direct band gap results in a greater efficiency in photon generation from an excited state. For this reason, monolayer MoS_2 and WS_2 are observed to have strong photoluminescence effect upon optical excitation.[20,85]

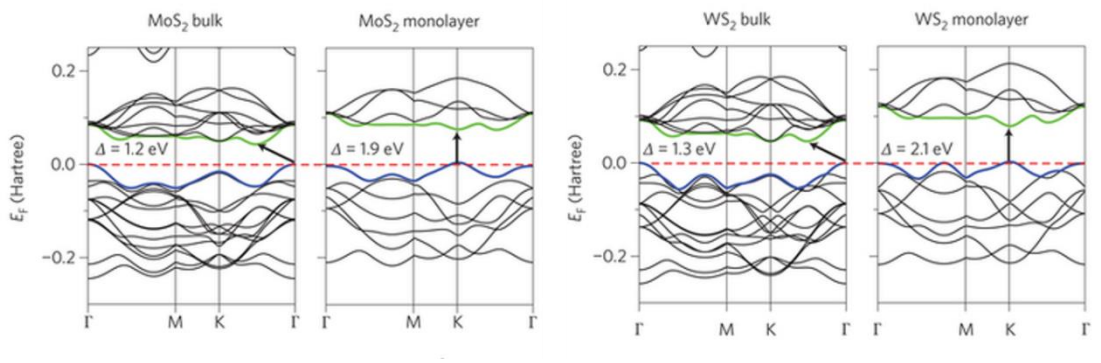


Figure 2.6 TMD Band structures. Band diagram calculated from first-principle DFT bulk and monolayer MoS_2 and WS_2. Horizontal red dashed lines represents the Fermi level, the valence band maximum and conduction band minimum are coloured in blue and green respectively. The change in arrow direction from bulk TMD to monolayer TMD shows the transition from indirect to direct band gap. Reproduced with permission.[84] Copyright 2011, American Physical Society.

2.5 Device Applications of 2D Crystals

2.5.1 Graphene FETs

Graphene-based FETs usually exhibit an ambipolar characteristic, with the type of transport carriers determined by the gate-induced electric field. A positive gate potential lowers the electron energy of graphene, leading to electron transportation, while a negative gate leads to a p-type (hole) conduction. This characteristic is clearly depicted in **Figure 2.7**, where the peak of the ρ-V_G curve is the Dirac point. Although the density of states vanish at the Dirac point for intrinsic graphene,[1] graphene transistors do not switch off entirely due to the presence of residual conductivity brought by charged-impurities.[86] This leads to a small I_{on}/I_{off} ratio of around 10 in graphene transistors, far from 10^4 required for logic applications.[87]

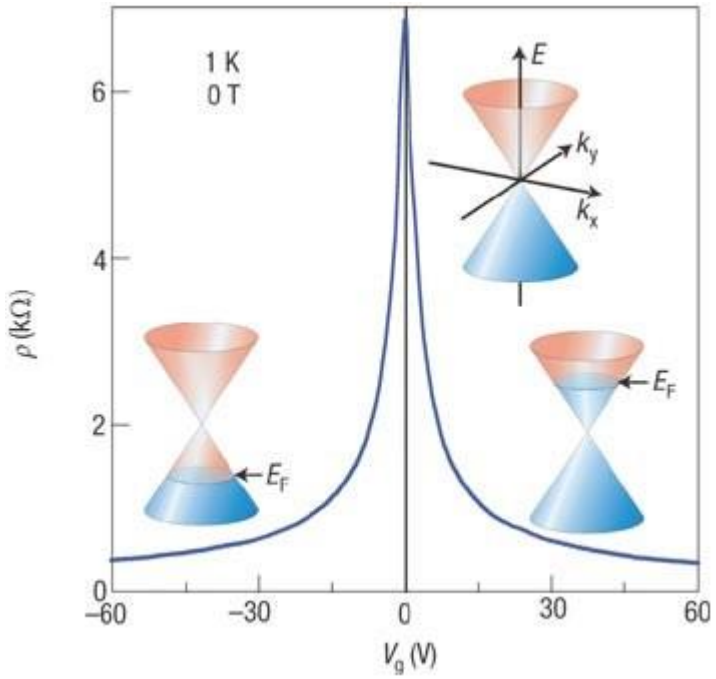


Figure 2.7 Electrical behaviour of graphene FET. Due to the cone-shaped band structure, graphene FET has the highest resistivity when Fermi level lies in between the conduction and valence band where carrier density is the smallest. For exfoliated graphene, the Dirac point is positioned at V_G=0 V. Reproduced with permission.[3] Copyright 2007, Macmillan Publishers Ltd.

Other than logic devices, many studies have investigated the use of graphene in radio-frequency (RF) analog devices, as switching off during RF operations is not required. Since 2008, graphene MOSFETs with gigahertz capabilities have been reported, with graphene channel fabricated via exfoliation [88,89] and epitaxial growth.[90] In 2010, Avouris *et al.* reported a 100 GHz transistor using a 240-nm gate,[91] soon overtaken by Duan *et al.* who developed smaller devices with a cut-off frequency of 300 GHz.[92] Theoretical studies made in 2011 projected a cut-off frequency of graphene transistors exceeding 500 GHz.[93] Up until 2012, graphene transistors with 400 GHz capability had been demonstrated.[94] Graphene RF transistors with real life applications were demonstrated by an IBM team in 2014.[95] Using a "passive-first active-last process", graphene was transferred lastly in the manufacturing process for a multi-functional RF integrated circuit. The circuit managed to perform practical wireless communication functions, which include receiving and restoring digital text transmitted with a carrier signal of 4.3 GHz.[95]

2.5.2 TMD-based FETs

The investigation of the electronic properties of bulk semiconducting TMD has been going on for decades.[96] However, it was only after the successful isolation of graphene in 2004 that monolayer semiconducting TMDs start to draw attention. Band gap exists naturally in many members of 2D TMDs, thus they do not require complex approaches to open a band gap as with graphene. The properties of 2D semiconducting TMDs such as MoS_2 and WS_2, including sizable band gaps, high thermal stabilities and the absence of dangling bonds make them suitable candidates for transistors applications.

In order to yield optimal results in devices' contact resistance, the I_{on}/I_{off} ratio and also the carrier, many studies have been devoted to understand what factors contribute to a high-performing TMD-based device. It is found that the combination of gate structure, dielectric layer, substrate, metal contacts, and the environment of measurement can determine the performance and stability of the TMD devices. In the following, studies on TMD device optimisation and new device architectures based on 2D crystals are reviewed.

2.5.2.1 Contact engineering

With reduced transistor channel length, contact resistance ultimately dominates charge transport. Metal electrodes thus play a critical role in determining the conductance of the fabricated devices based on 2D crystals. The Schottky barrier, which exists at the metal-semiconductor interface between source/drain electrodes and TMDs, not only limits the charge injection in the device's on-state but also impacts the off-state current.

A systematic study of metal contacts on carrier transportation was conducted by Das *et al.* on multilayer MoS_2 FETs.[97] Both high work function metals including nickel (Φ_{Ni}=5.0eV) and platinum (Φ_{Pt}=5.9eV), and low work function metals including scandium (Φ_{Sc}=3.5 eV) and titanium (Φ_{Ti}=4.3 eV) were investigated. It was initially expected that

electrodes of low work function would enable n-type device characteristic, while the high work function electrodes would enable a p-type device since in the latter case the Fermi energy lies closer to the valence band of MoS_2. Interestingly, all four groups exhibit the characteristics of an n-type FET, which suggests a strong pinning at the interface. For Pt, Ni, Ti and Sc, the Schottky barrier heights are 230, 150, 50 and 30 meV accordingly, the transconductance of 0.03, 0.14, 0.20 and 0.28 $\mu S/\mu m$ respectively and the effective field-effect mobility values of 21, 36, 125, and 184 $cm^2V^{-1}s^{-1}$.[97] These findings clearly suggest the importance of good metal contacts in extracting the intrinsic properties of 2D TMDs. The result also suggests that the mobility can often be underestimated due to contact resistance and that the correct choice of metal contacts can yield a higher (and more accurate) mobility.

It is worth noting that the existence of a Schottky barrier does not necessarily indicate a non-linear *I-V* relationship in devices. It is commonly observed that MoS_2 devices with Au contacts show a linear *I-V* curve,[83,98,99] which seems counterintuitive since Au has a high work function (5.1 eV), while n-type MoS_2 has an electron affinity of around 4.0 eV. An explanation for this is that the Schottky barrier at the metal-TMD interface is thin enough to allow low resistance tunnelling.[97] This results in a linear and seemingly "ohmic" transport characteristics for monolayer MoS_2 FETs even though high work function metals are used as contacts.

2.5.2.2 Influence of top/bottom interfaces

The ultrathin nature of 2D crystals leads to an extraordinarily high surface-volume ratio. Therefore, it can be expected that 2D TMDs are very sensitive to external influences brought by to their top and bottom interfaces.

An important aspect of a FET's performance relies on how effectively its channel conductivity responds to gate potential. Using a parallel plate capacitor model to represent the gated transistor, one can expect to achieve better gate control with increased capacitance of the dielectric layer, which can be expressed as $C_{ox} = \frac{\kappa \varepsilon_0 A}{t}$, where κ is the dielectric constant of the insulating layer, ε_0 is the dielectric constant of free space, *A* is the capacitor area and t is the thickness. Therefore, it is possible to increase gate control by fabricating thinner insulating layer, or incorporating high-κ dielectric for top/bottom gates.

Encapsulation of TMDs with dielectric layer can also lead to improved mobility of the TMD channel due to dielectric screening of the charge impurities.[100] Early work has shown that the mobility of monolayer MoS_2 was at least 3 orders of magnitude smaller than graphene (<10 $cm^2V^{-1}s^{-1}$), limiting its application in electronic devices.[54] The interest in monolayer semiconducting TMDs was renewed in 2011 when Radisavljevic *et al.*[83] demonstrated a high mobility MoS_2 FET using a top-gated structure, as shown in **Figure 2.8**a. A 30 nm HfO_2 layer was deposited as top gate dielectric layer. This led to a moderate mobility of around 70 $cm^2V^{-1}s^{-1}$, large I_{on}/I_{off} ratio (10^8) and relatively low *SS* of 74 mV/decade.[83,101] This finding suggests an effective approach for mobility engineering of TMD semiconducting channel by using a top-gate high-κ dielectric layer.

Some other top-gate structures include the use of ionic gel, which enables ambipolar characteristic in devices that would otherwise be unipolar transistors. Braga *et al.*[102] fabricated top-gated WS_2 FETs using ionic liquid 1-butyl-1-methyl pyrrolidinium tris-(pentafluoroethyl) trifluorophosphate $[P14]^+[FAP]^-$ as electrolyte dielectric. The extremely high capacitance of the electrical double layer enables tuning of Fermi level across the band gap to allow carrier injection into either the valence or conduction band, resulting in an ambipolar transport as shown in Figure 2.8b. To date, different top gate dielectric materials

including HfO_2,[54,83,103] AlO_2,[97] ZrO_2,[104] BN,[105] and ionic gel[102,106] have been employed in TMD-based FETs.

At the bottom interface of TMD devices, the choice of growth substrates of CVD-grown crystals can affect the built-in strain,[107,108] composition[109] and morphology[110,111] as it alters the reaction process and growth dynamics. When 2D crystals are transferred onto a substrate, they conform to the morphology of the substrate surface. Therefore the roughness of surface may affect the long- and short-range scattering parameters, affecting carrier mobility.[112] Moreover, certain substrates are known to induce charge transfer doping, which can further impact the transport and optical properties of TMD transistors.[113,114]

In an experiment carried by Withers *et al.*,[115] it was found that the large hysteresis measured on a 4-layered WS_2 transistor on SiO_2 can be fully supressed by using h-BN as the device substrate. Shown in Figure 2.8c-d, the field-effect mobility of the WS_2 transistor with a h-BN substrate (80 $cm^2V^{-1}s^{-1}$) is larger than that of WS_2 transistor on SiO_2 (~17 $cm^2V^{-1}s^{-1}$) by more than a factor of 4. Similarly, Bao *et al.*[112] reported that using PMMA as the substrate can yield higher mobility for MoS_2 transistors. The mobility was found to be further improved when the MoS_2 crystals are sandwiched between PMMA layers. These evidences reaffirm the strong influence on TMD transistors' performance brought by dielectric layers.

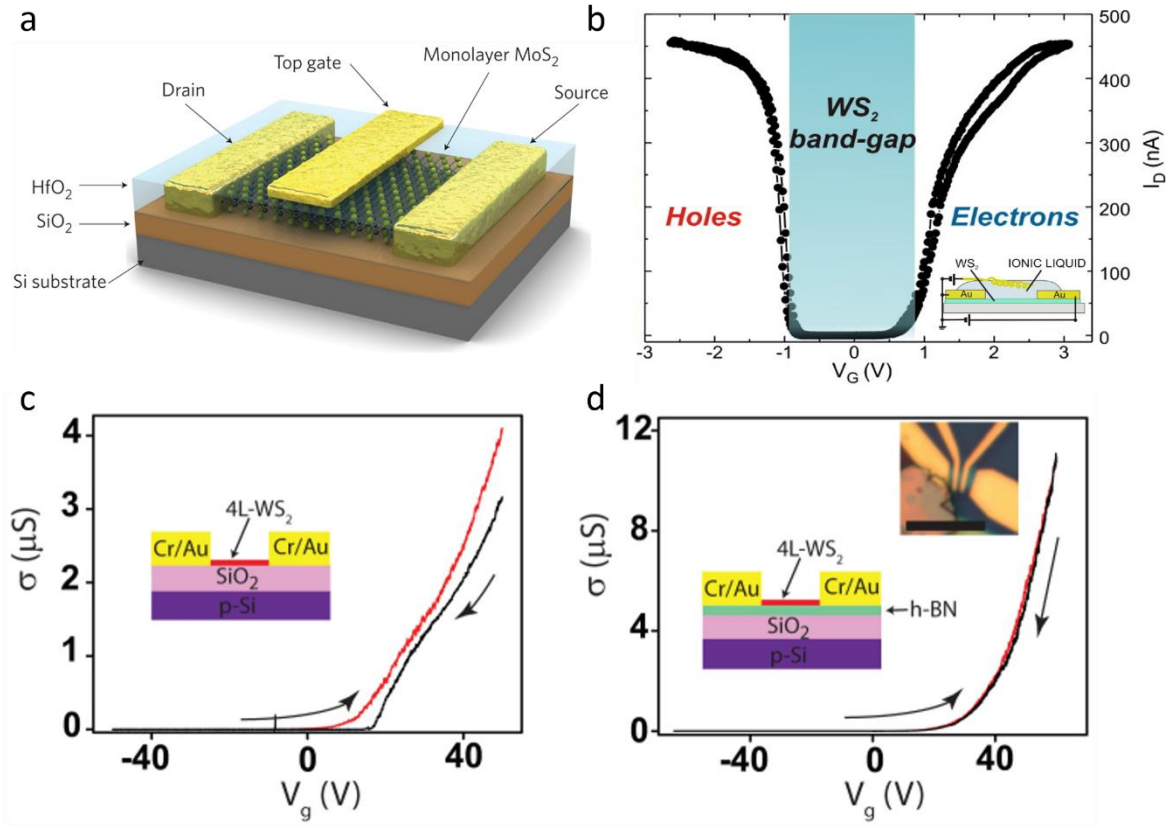


Figure 2.8 Dielectric layer of TMD-based FETs. (a) Schematic of monolayer MoS_2 FET encapsulated by 30 nm of deposited HfO_2 that acts as a gate dielectric and a mobility booster. Reproduced with permission.[83] Copyright 2011, Macmillan Publishers Ltd. (b) Ambipolar characteristics of WS_2 FET due to enhanced gate control using ionic liquid. Reproduced with permission.[102] Copyright 2012, American Chemical Society. (c-d) Comparison in field effect of few layer WS_2 transistor on SiO_2 and h-BN substrates. Mobility of device was improved on a h-BN substrate. (c,d) Reproduced with permission.[115] Copyright 2014, Macmillan Publishers Ltd.

The environment in which the measurements are carried out also influences the device performances. Absorbed H_2O and O_2 on TMDs surface are known to affect their carrier transport properties of FETs.[98,116] **Figure 2.9**a shows a device consisting of single-layer WS_2 FET with gold contacts. The field-effect behaviours of monolayer WS_2 FET obtained under different atmospheric pressures are shown in Figure 2.9b. The measurement suggests that a high vacuum condition and long hours of device annealing can result in a smaller threshold voltage V_{th} and higher I_{on}/I_{off} ratio (>10^4), while devices measured in air respond poorer to gate.[117] Surface adsorbates present under ambient conditions can also induce trap states, leading to hysteresis in TMD FETs measurements. In a controlled

experiment carried out by Late *et al.*, the I_{ds}-V_G measurement of WS_2 FET was conducted under vacuum, dry air and air with different levels of humidity.[118] As shown in Figure 2.9c-d, the hysteresis obtained under vacuum is smaller, and increases with increasing humidity. It was found that the hysteresis can be minimised by encapsulating the device with a dielectric layer, essentially isolating the 2D crystals from air. This led to hysteresis-free measurements and high mobilities of the encapsulated devices even under high humidity.[118]

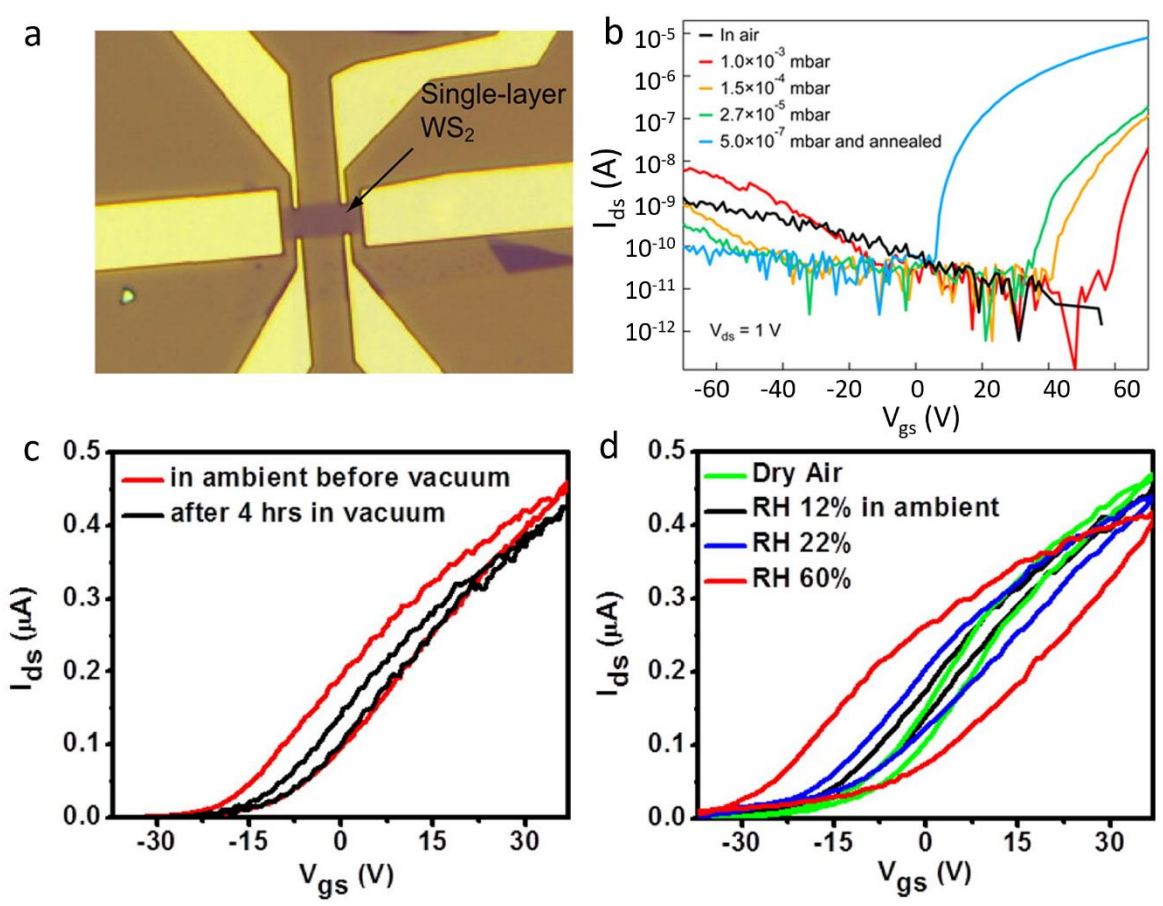


Figure 2.9 Influence of ambient environment to TMD-based FET. (a) Optical image of monolayer WS_2 FET contacted by gold electrodes. (b) I_{ds}-V_G measurements of WS_2 FET in (a) under ambient condition and different pressure. (a,b) Reproduced with permission.[117] Copyright 2014, American Chemical Society. (c) Hysteresis of transport curve under ambient condition and vacuum. (d) Hysteresis of transfer curve under dry air and different relative humidity (RH) levels. (c,d) Reproduced with permission.[118] Copyright 2012, American Chemical Society.

2.5.2.3 All-2D Field-effect Transistors

To achieve a truly ultrathin device based on 2D crystals, graphene electrodes are used in replacement of conventional bulk metal contacts. In an attempt of realizing a FET made of all 2D crystals, Roy *et al.* demonstrated the use of graphene as the source, drain and gate electrodes (**Figure 2.10**a).[105] Few-layer exfoliated MoS_2 was used as the channel and exfoliated BN as the top gate dielectric. The device exhibits an n-type transport behaviour, an I_{on}/I_{off} ratio of $>10^6$ and mobility of ~33 $cm^2V^{-1}s^{-1}$ as shown in Figure 2.10b.

Instead of using laterally-separated electrodes, devices can also employ vertically-stacked electrodes, to form a 2D vertical heterostructure with tunable electrical current along the z-direction. 2D tunnel field-effect transistors (TFETs) are examples of such devices. The ultrathin characteristics of 2D crystals allow electric fields to partially penetrate through the vertical stack, enabling gate control of the tunnelling current.

In previous studies, TFET devices with barriers comprising thin layers of h-BN[119] or semiconductor/metal Schottky interface[120,121] demonstrated current flow that can be modulated by applied V_G. In 2012, an all-2D TFET was demonstrated by Georgiou *et al.*[122] by sandwiching TMD with top and bottom graphene layers to form vertical a graphene-TMD-graphene heterostructure. As shown in Figure 2.10c, the TMD layer acts as a tunnelling barrier, through which the tunnelling probability can be tuned by changing the Fermi level of the graphene using V_G. A current modulation of up to 10^6 for I_{on}/I_{off} was achieved in such vertical device configuration.[122]

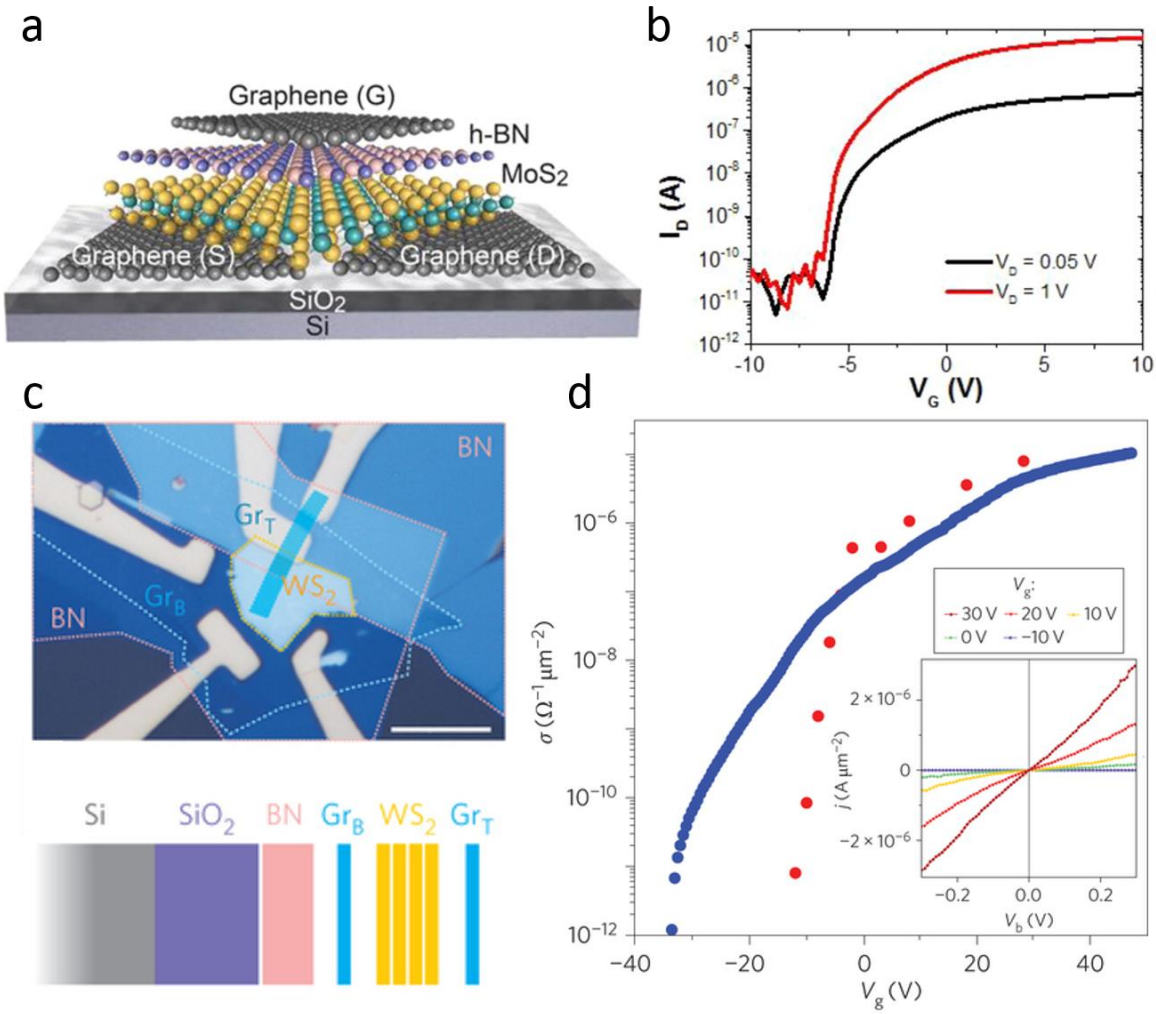


Figure 2.10 All-2D Field-effect transistors. (a) Schematic of a FET with lateral Gr-MoS_2-Gr configuration. h-BN is used as gate dielectric, and graphene is used for source, drain and gate electrodes. The field effect measurement of such a device is shown in (b), with an I_{on}/I_{off} ratio of over 10^6. (a,b) Reproduced with permission.[105] Copyright 2014, American Chemical Society. (c) Optical image added colour (Scale bar represents 10 μm) and side view schematic of FET with vertical graphene/WS_2/graphene configuration. The vertical device utilises tunnelling current across the few layer WS_2 barrier, which is tunable by applied gate potential as shown in transfer curve (d). (c,d) Reproduced with permission.[122] Copyright 2013, Macmillan Publishers Ltd.

2.5.3 TMD-based Photodetectors

Photodetectors convert light into electrical signals and are at the core of many imaging and optical sensing applications. Compared with graphene photodetectors, TMD-based photodetectors provide lower dark current and larger photoresponsivity (defined as $R=I_{photo}/P_{opt}$, where I_{photo} is photocurrent and P_{opt} is optical input power).[123] Down to a few atomic layers, TMDs have sizable optical absorption edge between 1 to 2 eV which are

desirable for infrared to visible light detection. TMDs are also considered as promising candidates for solar cells, because strong optical absorption per layer and overlapping of their band gaps within the visible spectrum.[124] Additionally, their natural abundance and chemical stability are appealing for low-cost productions of solar cells.[18]

The physical mechanisms that contribute towards photocurrent generation in TMD-based photodetectors usually consists of the photoelectric[125] and photo-thermoelectric effect.[126] Photoelectric effect is the separation of photo-excited electron-hole pairs under an electric field. This can be either an external electric field that is applied to the device (photoconductive effect),[127–131] or a built-in electric field (photovoltaic effect) which arises in p-n junctions[132–135] and TMD-metal (Schottky) interfaces.[136] Photo-thermoelectric effect occurs when there is a temperature gradient in the photodetector, usually induced by non-uniform light illumination. The temperature gradient results in a voltage difference V_{PTE} due to Seebeck effect, defined as $V_{PTE} = (S_1\text{-}S_2)\Delta T$, where S_1, S_2 are Seebeck coefficients of the two substances. The temperature gradient is usually caused by a localized illumination on a measured device, or a global illumination on a device that has varying absorption on different parts. In TMD photodetectors, currents generated by photothermoelectric effect are usually very small compared to those generated by the photoelectric effect.[125,126] Here we focus on the photoelectric effects, which are mainly studied in TMD-based photodetectors, and review the devices categorised by their different working mechanisms.

2.5.3.1 Photoconductor/Phototransistor

A photoconductor (or phototransistor) is the simplest form of photodetector. It typically shares the same metal-semiconductor-metal (MSM) configuration with an FET, and operates under the photoconductive effect relying on applied electric field for photo-excited carrier separation. Other than photoresponsivity, photoconductive gain (G), defined

as number of photocarriers collected by electrodes over the number of incident photons, is another important figure of merit of photoconductors. Photoconductors can achieve gain larger than unity, which is facilitated by charge traps, where one type of photocarrier (holes or electrons) are trapped within localized states at defects or surface adsorbates, while the oppositely-charged carriers contribute to the channel current.[137,138] The trapped charges may act as local gates and modulate conductance of the semiconductor similar to a gated transistor, a mechanism known as the photogating effect.[139]

Figure 2.11a shows a TMD photoconductor with an MSM configuration employed by several studies on MoS_2,[127–131] WS_2,[140–142] $MoSe_2$,[143] WSe_2[144–146] photoconductors. In this work done by Lopez-Sanchez *et al.* on exfoliated monolayer MoS_2, a high photoresponsivity of 880 A W^{-1} was achieved under a low illumination power.[127] However, the high responsivity came at the price of long response time of 4 s. The response time can be effectively reduced to 600 ms using a gate pulse to reset the conductivity of the transistor. During a similar time, Zhang *et al.* achieved a record-high photoresponsivity of 2200 A W^{-1} based on CVD-grown monolayer MoS_2.[129] The measurement was conducted under vacuum, with a large applied gate of +50 V, using interdigited Ti electrodes for decreased resistance. Under vacuum, the decay time constant of the photoconductor decreases with lower temperature, from 500 s under 300 K to 0.055 s under 153 K. This is because the thermal energy of the carriers within trap states is much smaller than the activation energy under lower temperatures, and thus cannot contribute to the collected photocurrent under such conditions.[129] Several studies have reported that the response times of TMD-based photodetectors can be effectively reduced by encapsulation of a passivation layer. For example, Kufer *et al.* reported that by encapsulating MoS_2 photodetectors with HfO_2, decay time dropped from 120 ms to 8 ms (Figure 2.11c-d), which is an improvement by over an order of magnitude.[131] Similar improvements have been observed with Al_2O_3

encapsulation.[131] Overall, reducing the device resistance with suitable metal contacts,[147] electrostatic gating,[127,131,148] or encapsulation of device with dielectric layer,[131,149] seems to yield better performances. Responsivities and response times of MoS_2 photodetectors are typically in the range from 10^{-1} to 10^{3} A W^{-1}, and 10^{-3} s to 10 s respectively depending on different crystal synthesis methods, layer numbers, device geometries, operating conditions, and the type of trap states facilitating photocarrier generation.[127–131]

As discussed previously, the term "photoconductive gain" refers to the fact that the number of charge carriers collected for every absorbed photon on a photodetector can be greater than one.[150] This feature is enabled by the existence of trap states, which prolongs the carrier lifetime by capturing one of the photo-excited carriers upon illumination, hence inhibiting the electron-hole recombination rate and allowing the opposite photocarrier to circulate within the circuit. For this reason, photoconductors rely on long-lived trap states for high photoconductive gain.[137] In trap-dominated detectors, photocurrent generation usually follows a sub-linear relation with the illumination power. This is attributed to the saturation of available trap states, and increased recombination of free carriers due to a more populated conduction band under increasing power.[125,127,129] This results in a negative power dependence of photoresponsivity as shown in Figure 2.11e.

However, under certain conditions the opposite trend may occur. In a study conducted by Kufer *et al.*, an anomalous trend was observed in the sub-threshold region of a MoS_2 transistor under low power, and photoresponsivity increased as light power increased to a certain extent before its eventual drop (Figure 2.11f).[131] This is because much of the trap states near the band edge are initially unoccupied owing to a lower Fermi level, and subsequently filled upon illumination, effectively prolonging carrier lifetime and consequently raising photoresponsivity. During this process, photogating effect may also contribute to a lower overall resistance and result in an enhanced responsivity.[131]

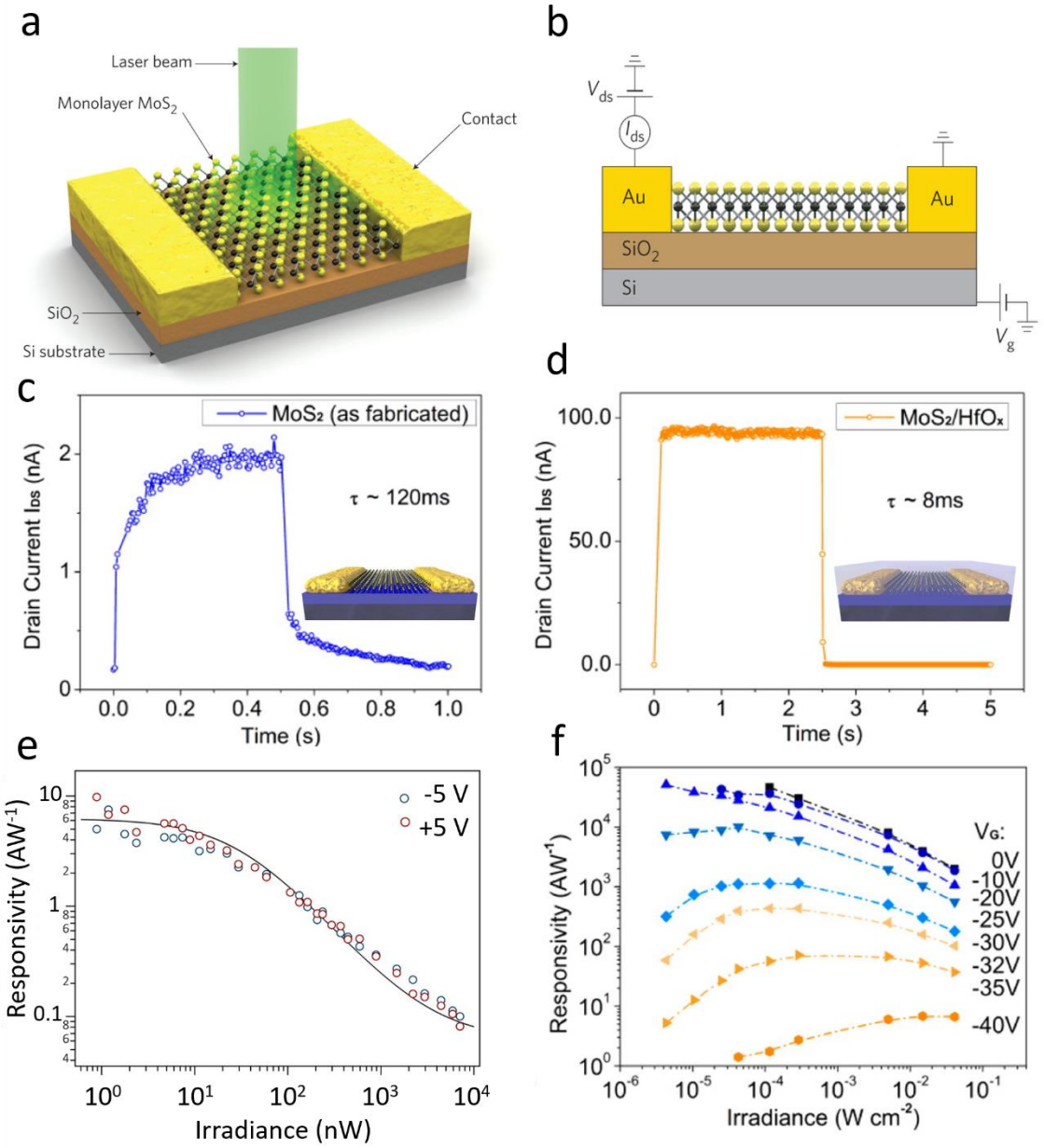


Figure 2.11 Monolayer TMD phototransistors. (a) 3D illustration and (b) side view schematic of a MoS_2 phototransistor. (a,b) Reproduced with permission.[127] Copyright 2013, Macmillan Publishers Ltd. (c) Transient photocurrent measurement over one cycle of light modulation on as fabricated MoS_2 device and (d) HfO_2 encapsulated MoS_2 device. The encapsulation improves photocurrent by a factor of ~40 and reduces decay time by over an order of magnitude. (d,e) Reproduced with permission.[131] Copyright 2015, American Chemical Society. (e) Power dependence of MoS_2 phototransistor's photoresponsivity. Reproduced with permission.[125] Copyright 2015, American Chemical Society (f) Power dependence of MoS_2 phototransistor under different gate voltage. When $V_G<V_{th}$, a more complex mechanism in trap-assisted photocarrier generation in found. Photoresponsivity rises under low power with increasing light, and eventually drops at large power when most trap states are saturated. Reproduced with permission.[131] Copyright 2015, American Chemical Society.

2.5.3.2 Photodiodes and Photovoltaic

As discussed previously, other than relying on the external electric field provided by applied V_{ds} (photoconductive mode), photodiodes can also operate via photovoltaic mode, which relies on a built-in electric field at a junction interface to extract photocarriers. For this reason, photodiodes working under photovoltaic mode can generate photovoltage (open-circuit voltage, V_{oc}), or short-circuit current (I_{sc}), without external sources. Exploitation of such photovoltaic effect is the basis of solar cells, which converts solar energy to electricity. Generally, the built-in potential are formed at p-type/n-type semiconductor (p-n) junctions or metal-semiconductor (Schottky) junctions. An important parameter of a photovoltaic device is the extrinsic quantum efficiency (*EQE*), defined as the ratio of the number of charge carriers generated to the number of incident photons. This can be expressed in terms of the photocurrent I_{photo}, incident power per unit area P, and excitation wavelength λ by $EQE = \frac{hc}{e}\frac{I_{photo}}{P\lambda}$, where h is the Planck constant, c the speed of light in vacuum, and e the elementary charge unit.

Applying a local electrostatic gate is one way to artificially create a p-n junction along a semiconductor channel. 2D crystals with ambipolar properties such as WSe_2[132,133,151] and black phosphorous[152] have been studied as photodiodes using separate gate modulation. As shown in **Figure 2.12**a, a layer of WSe_2 crystal is transferred onto a substrate with pre-defined split gate electrodes. The split gate electrodes are used to induce a p-n junction on the WSe_2 channel through individual control of the carrier types and concentrations at different parts. Figure 2.12b-c show the *I-V* characteristics of such dual-gated device in dark and illuminated conditions. Controllable junction within the device can be achieved with varied gate bias configurations, resulting in various behaviours including p-n, n-p, n-n and

p-p type junctions. Reported responsivities using this method are between 0.7 mA W^{-1} to 270 mA W^{-1} with the *EQE* values in the range of 0.1 – 0.2%.[132,133,151]

When placed together, TMDs with different conductive types (p-type and n-type) usually form heterostructures with a type-II band alignment. Upon illumination, it is observed that photo-excited electron-hole pairs that are generated within these junctions undergo efficient and ultra-fast separation within 50 fs to sub-picosecond.[153–155] This charge transfer can be utilized in optoelectronics and energy harvesting.[153]

To date, devices based on TMD/TMD vertical heterostructures including MoS_2/WS_2,[156] MoS_2/WSe_2,[134,135] $MoSe_2/WSe_2$[157] and WS_2/WSe_2[158] have been widely studied for light sensing applications. Shown in Figure 2.12d, Lee *et al.*[135] used n-type MoS_2 and p-type WSe_2 to form a vertical heterostructure, contacted by aluminum and palladium respectively for electron and hole injection. V_{oc} as large as 400 mV has been observed as shown in Figure 2.12e, and spatial photocurrent mapping under V_{ds}=0 V indicates that the photocurrent is primarily generated at the heterostructured region (Figure 2.12e inset).

Laterally stitched TMD heterostructures such as MoS_2/WS_2[159] MoS_2/WSe_2[160] and $MoSe_2/WSe_2$[161] were grown and studied. Similar to the vertical TMD/TMD heterostructures, lateral heterostructures also exhibit a diode-like behavior and photovoltaic responses as shown in Figure 2.12f-g. Together, photodetectors based on vertical and lateral TMD/TMD heterostructures show a wide ranging performance with photoresponsivities ranging from several 10^{-3}A W^{-1} to 10^4 A W^{-1}, and response times between 10^{-2} ms to 10 ms.[134,135,156–161]

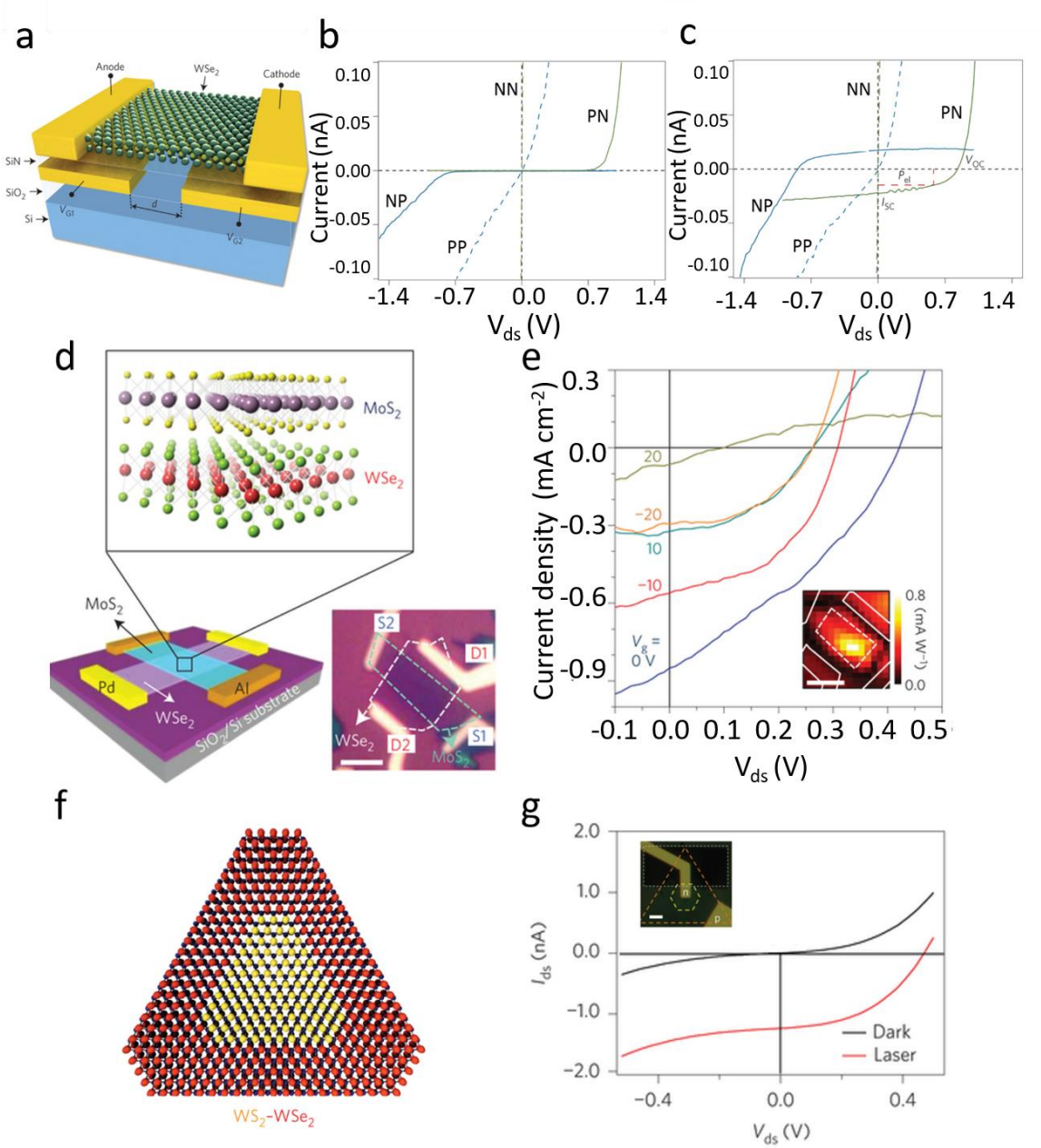


Figure 2.12 Photodetectors based on TMD p-n junctions. (a) 3D schematic of a dual-gated single-layer WSe_2 photodetector with local electrostatically defined p-n junctions. I_{ds}-V_{ds} characteristics of the device under varied gate bias configurations (b) in darkness and (c) under optical illumination, respectively. (a-c) Reproduced with permission.[132] Copyright 2014, Macmillan Publishers Ltd. (d) Bottom left: 3D schematic of vertically stacked MoS_2/WSe_2 heterojunction device. Top: atomic structure illustration of MoS_2 and WSe_2 stacks. Bottom right: Optical image of fabricated device. (e) I_{ds}-V_{ds} characteristics of vertical heterostructure device in (d) with photo-illumination under different gate voltages. Inset: scanning photocurrent mapping of the heterostructure at V_{ds}=0. (d,e) Adapted with permission.[135] Copyright 2014, Macmillan Publishers Ltd. (f) Atomic structure illustration of a lateral WS_2-WSe_2 heterostructure. (g) I_{ds}-V_{ds} characteristics of lateral heterostructure device in (f) under dark and illuminated conditions. Inset: optical image of a heterojunction p–n diode device. Adapted with permission.[162] Copyright 2014, Macmillan Publishers Ltd.

Photodiodes can also make use of the built-in potential at the Schottky interface, or rather the asymmetry of the two Schottky junctions. This can be achieved by using two

dissimilar metals for source and drain electrodes, where the sum of the built-in potential formed at the interface on both ends of the semiconductor channel is non-zero. In **Figure 2.13**a, Fontana *et al.*[136] reported the photovoltaic effect in devices based on thin MoS_2 flakes with source/drain electrodes using gold and palladium respectively. Owing to the different work functions of Au and Pd, the Schottky barrier asymmetry effectively creates a built-in electric field that facilitates photocurrent generation. The *I-V* characteristics of such device are plotted in Figure 2.13b. The device exhibits a rectifying behavior under dark conditions and a V_{oc} of up to 100 mV under irradiation.[136]

2D photodetectors can also utilize the asymmetry of junctions in a vertical graphene-TMD-graphene heterostructure where the TMD layers acting as adsorption layers are sandwiched between semi-metallic graphene layers, as depicted in Figure 2.13c. Figure 2.13d shows an example of the *I-V* characteristics of such device under dark and illuminated conditions, as a function of different gate bias. Under a suitable gate potential, photovoltaic response is observed with a considerable V_{oc}. This is attributed to the built-in potential between the top and bottom graphene, which can be modified by V_G.[163,164] As shown in Figure 2.13e, graphene is distinct from bulk metals owing to its limited density of states, resulting in a work function that is tunable by gate potential and chemical dopants. As the top graphene is less susceptible to the electric field brought by the back-gate due to dielectric screening, the Fermi level of the top and bottom graphene can be positioned differently via electrostatic gating (Figure 2.13e**,** bottom), resulting in a built-in potential within the TMD necessary for electron-hole pair dissociation. This particular device concept is explored in the works of Britnell *et al.*[163], Yu *et al.*[164] and Massicotte *et al.*[165] where the top and bottom graphene electrodes were employed to sandwich a thin (<50 nm) layer of WS_2, MoS_2, and WSe_2 respectively. These vertically stacked graphene/TMD/graphene heterostructure devices demonstrate gate tunable built-in electric fields, and exhibit photoresponsivity

between ~10^2 to 10^5 A W^{-1}, *EQE* values in the range of 7.3%-55%, with very fast response times between ~1.6 ns to ~50 μs owing to the atomically thin carrier transient paths and efficient charge separation.[163–165]

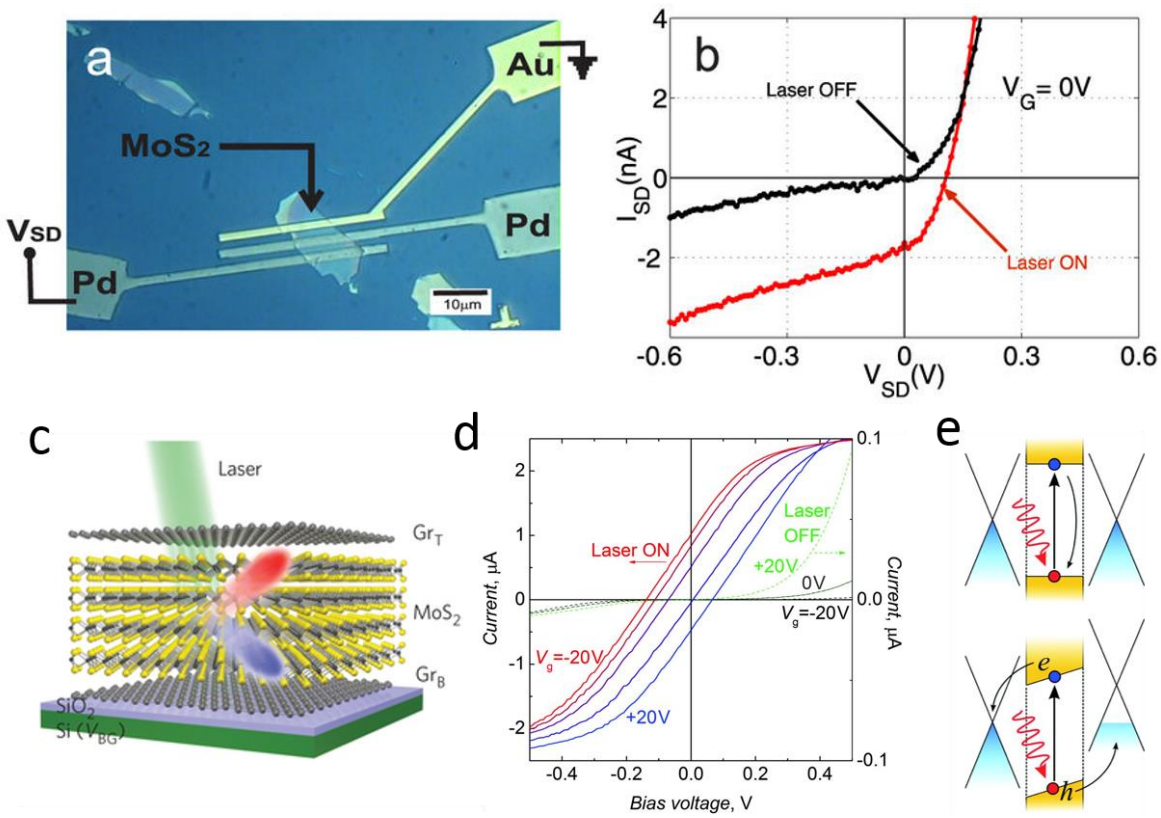


Figure 2.13 Photodetectors based on Schottky junctions. (a) Optical image of a lateral device based on MoS_2 with Au and Pd as source and drain electrodes respectively. (b) I_{ds}-V_{ds} characteristics of the Pd-MoS_2-Au device under dark and illuminated conditions. Reproduced with permission.[136] Copyright 2013, Macmillan Publishers Ltd. (c) 3D schematic of a graphene/MoS_2/graphene vertically stacked heterostructure. Reproduced with permission.[164] Copyright 2013, Macmillan Publishers Ltd. (d) I_{ds}-V_{ds} characteristics of a graphene/WS_2/graphene vertical heterostructure as a function of gate bias under dark (green traces) and illuminated conditions (blue and red traces). (e) Schematic band alignments in equilibrium (top) and under gate biasing (bottom). (d,e) Reproduced with permission.[163] Copyright 2013, American Association for the Advancement of Science.

Chapter 3 Device Fabrication and Characterization Techniques

3.1 Introduction

This thesis aims to investigate the electronic properties of 2D crystals and their heterostructures. As means to reach this goal, multiple characterization and fabrication techniques are used to determine the quality of 2D crystals, and implement them into electronic devices for electrical/opto-electrical measurements. In this chapter, we will go through the fabrication methods and characterization techniques that are used.

3.2 Crystal Growth and Device Fabrication

The ability to synthesize 2D crystals on a large wafer scale using CVD allows us to integrate conventional device fabrication techniques into our processes. These include the wet transfer technique and lithography patterning which allow us to fabricate hundreds of devices on a 1 cm^2 silicon chip for batch measurements.

3.2.1 Chemical Vapour Deposition of 2D Crystal

3.2.1.1 Graphene

Monolayer graphene was grown using copper (Cu) as catalyst and tungsten (W) as substrate.[166] Precursor gases were introduced at a temperature beyond the melting point of Cu, and directly deposited on liquid-form copper. Cu and W films were cut into 1 cm^2 pieces and rinsed in acetone and IPA. Hydrochloric acid (HCl) was applied to Cu before rinsing to eliminate the oxide layer. Cu was mounted on W and placed in the furnace. 100 sccm of Hydrogen (25%) and 200 sccm of Argon was used to anneal the sample at 1090 ^oC for 30 min before growth. Graphene was grown on the melted Cu with a flow of 200 standard cubic

centimetres per minute (sccm) argon, 30 sccm hydrogen (25%) and 10 sccm of methane (1%) gas for 90 min. The sample was then removed from the heating zone and cooled to room temperature. Crack-free graphene films can be grown using an optimised growth method by introducing a secondary growth procedure at 1060 ºC for 30 min.[167]

3.2.1.2 MoS_2 and WS_2

Monolayer MoS_2 was grown on a 300 nm SiO_2/Si substrate using molybdenum trioxide (MoO_3) and sulfur powder under atmospheric pressure.[168] The two precursors, MoO_3 and sulfur powder were positioned in an internal and external tube respectively within a double-walled-quartz-tube, and heated individually by two furnace systems. Argon was used as the carrier gas for the vaporised precursors. The S, MoO_3 and SiO_2/Si substrate were heated to 180, 300, and 800 ºC, respectively, and the reaction occurred for 30 min. Monolayer WS_2 was grown using a similar method [169] using Tungsten trioxide (WO_3) and sulfur powder as precursors. An optimised recipe with the addition of hydrogen allows the growth of thin WS_2 films, which enables a higher yield in wafer-scale device fabrication in Chapter 5.[170]

3.2.2 Transfer Techniques

A wet transfer technique is commonly used to transfer CVD-grown crystals onto arbitrary substrate for further processing.[171,172] In this thesis, the wet transfer process involves the use of a polymer scaffold, poly(methyl methacrylate) (PMMA) (8 wt% in anisole, 495k molecular weight), which is spin-coated on each as-grown samples. The original substrates were removed in a chemical etchant, resulting in a floating PMMA/2D crystal film on the aqueous solution. The transfer process is then completed by mechanically scooping the film onto a target substrate.

Graphene was grown on copper with a tungsten substrate. The tungsten substrate was electrochemically etched in NaOH (2 M) by applying a 2.4 V potential to the sample and using a Cu foil as anode.[167] The PMMA/graphene film was then separated from Cu substrate by $(NH_4)_2S_2O_8$ etching (0.1 M).

MoS_2 and WS_2 were grown on SiO_2 substrate, which can be etched using KOH solution (1 M) at 60 ^oC for 30 min.

After the transfer process was completed, the sample with PMMA was baked at 150 ^oC for 30 min for sample adhesion. This was then followed by soaking sample in hot acetone of 45 ^oC for PMMA removal.

3.2.3 Electron-Beam Lithography and Photolithography

Electron-beam lithography (EBL) technique uses a focused beam of electrons to expose an electron sensitive resist film, while photolithography uses ultraviolet (UV) light to irradiate a photoresist film. Both are commonly used techniques for making micro- or nano-electronics. Electron beam or UV exposure induces a change in the structure or chemical composition of the resist, changing their solubility in developing agents known as "developer". A positive resist refers to those with molecules that turn more soluble in developer upon exposure, thus are removed if exposed. On the contrary, negative photoresist refers to those with molecules that would crosslink and remain un-removed by developer if exposed by light. The developing process results in a patterned coating on the substrate surface that will allow further fabrication processes, which in our work can be either metallization or plasma etching.

For photolithography, MicroPosit S1813 G2 photoresist was used as positive resist and MicroChem MaN 1420 photoresist was used as the negative resist. Resist was spin-coated for 1 minute at 4500 rpm, resulting in a film thickness of 1.2 μm for S1813 positive

resist and 2 μm for MaN1420 negative resist. Subsequent to spin-coating, the positive resist was baked at 115 ^{o}C and negative resist was baked at 90 ^{o}C, both for 1 min. This was followed by light exposure. UV light source were placed at the top of the equipment to irradiate the resist-coated substrate over a photomask, which has Cr reflection layer to block certain regions of the substrate from exposure. The photomask and the sample were aligned and pressed into contact for exposure on the Karl Suss MJB3 mask aligner.

For EBL, a bilayer PMMA recipe was used for positive photoresist. A PMMA with lighter molecular weight (495 K) in anisole solvent was first spin-coated on the substrate, followed by spin-coating of PMMA with larger molecular weight (950 K). As exposed PMMA 495 K dissolves quicker in developer, the bilayer configuration enables an undercut profile which is suitable for lift-off after metal deposition. Both PMMA 495 K and 950 K were spin-coated at 4500 rpm for 45 s, and baked at 180 ^{o}C for 90 s before exposure. MaN2304 was used as negative electron resist, spin-coated at 3000 rpm for 30 s on the substrate, and subsequently baked at 90 ^{o}C for 60 s before exposure. The JEOL JBX-5500FS EBL system was used for patterning. Device patterns were drawn on the resist-coated sample substrates according to imported designs created by computer-aided-designs (CAD) software such as AutoCAD (**Figure 3.1**).

In these two systems that are used, the EBL has a higher resolution and can achieve sub-50 nm device features while photolithography has difficulty patterning sub-1 μm features. By eliminating a mask in the process, EBL is suitable for customized designs, although this flexibility usually comes at the expense of longer processing time and higher cost.

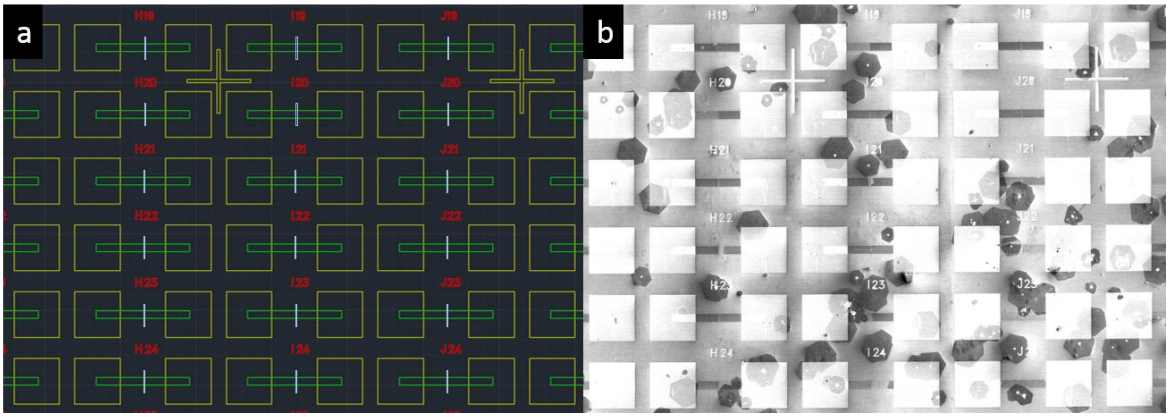


Figure 3.1 EBL: From software to hardware. (a) AutoCAD design of a device array for EBL patterning, illustrating metal bond pads (gold squares), graphene ribbons (green rectangle) and the gaps between electrodes (cyan rectangle). (b) SEM image of the fabricated device using design of (a) with deposited Cr/Au bond pads, graphene electrodes and transferred WS_2 domains.

3.2.4 Metal Evaporation

The Edward 360 thermal evaporator was used for depositing thin layer of metals which form the electrodes and bond pads of the devices. Following lithography patterning, the samples were placed upside down on a target plate above the source material (Cr, Au) in a vacuum chamber. In a thermal evaporator, metal sources are heated to high temperature through Joule heating, and evaporated onto the target substrate. This was followed by a lift-off process, where unwanted regions of metal film that lie on top of the resist were removed altogether by soaking the metallized sample in warm acetone at 45 ^{o}C for about 3 hours.

3.2.5 Plasma Etching

Plasma etching is a common technique in semiconductor processing used to remove a given substrate material. The plasma etcher stimulates electrons of gas atoms through a high frequency electric field to form a plasma state. The plasma etching can be realized through physical ion bombardment, chemical reaction or a combination of both.[173]

For this work, the Diener plasma etcher with a 40 kHz RF electromagnetic field was used for plasma generation. O_2 plasma was used for the removal of excess 2D material to create well-defined device structures on Si chip. The plasma chamber was first pumped

down and flushed with O_2 gas with a flow rate of 40 L_n/h. During the etching process, the chamber pressure was maintained between 0.3-0.4 mbar. Graphene was etched under a 60 W *RF* power for 30 s, graphene protected by a bilayer PMMA resist was etched at 80 W for 300 s. MoS_2 and WS_2 were more difficult to remove than graphene, and required power of 90 W for over 100 s etching time.

3.3 Characterization and Measurements

Device fabrication may be a laborious and time-consuming effort, and for this reason it is crucial to select only the suitable 2D crystal samples to undergo the fabrication process. Primary observations using optical microscopes and scanning-electron microscopes (SEM) allowed us to weed out non-ideal samples where crystals were absent, sparse, contaminated, inhomogeneous or were simply too thick. Furthermore, the chemical composition, layer number and continuity of selected samples can be determined using more precise techniques such as atomic-force microscopy (AFM), Raman and photoluminescence (PL). These techniques are also helpful in characterizing fabricated devices, as they provide insights into how crystal structure and fabrication processes affect the device properties and performances. Herein we present the characterization techniques and measurement setups used in this thesis.

3.3.1 SEM

SEM is a typical microscopy technique used to characterize the surface morphology of a given solid material, and is a common tool to reveal the crystal structure, orientation, continuity and homogeneity of 2D materials. Accelerated electrons under high voltage (up to 30 kV) are directed at the sample, producing signals including secondary electrons and backscattered electrons that are commonly used for SEM imaging. Secondary electrons refers to electrons emitted by an atom put into an excited state by the incident electron beam.

It is surface sensitive and therefore reveals the morphology and topography of the solid surface.[174] Back-scattered electrons are collected when incident electrons collides with the sample atoms and re-emerge from the surface. The amount of collected back-scattered electrons correlates to the mean atomic number of the sample, and thus carry information about the chemical composition of a given material.[174]

In this work, a Hitachi S-4300 cold emission SEM is commonly used. A 2-3 kV acceleration voltage is used for the observation of 2D crystals on Si substrates, with a resolution that can reach down to 100 nm. For finer observations, we use the Zeiss Merlin SEM, which has a resolution of down to 1 nm for secondary electrons imaging.

3.3.2 Photoluminescence and Raman

As discussed previously, both MoS_2 and WS_2 go through an indirect-to-direct band gap transition when reduced to their monolayer forms. In these single layer TMDs, strong PL signal exhibiting a single peak corresponding to direct excitonic transition is expected, as revealed in previous studies.[85,175] In few-layer TMDs where competition exists between direct and indirect electronic transition, this PL peak is dramatically reduced and accompanied by other features related to indirect transitions.[85]

Raman spectra is the result of the inelastic scattering process. During laser excitation, a small fraction of photons excites the vibrational or rotational modes of the crystal, and are inelastically scattered, giving rise to Raman lines known as the Stokes lines. The energy difference of the incident photons and the Stokes signal corresponds to the energy required to excite vibrational modes of the lattice, which are dependent on the atoms and bond force constants that form the crystal. Raman spectroscopy has been an effective tool in providing qualitative assessment of doping level,[176,177] strains[178–180] and thickness[27,181,182] of 2D crystals.

The E^1_{2g} and A_{1g} are the two main first-order modes observable in Raman spectra of monolayer MoS_2 and WS_2.[27,183] E^1_{2g} mode corresponds to the in-plane motion of sulfur and metal (Mo, W) atoms in opposite directions, and A_{1g} mode is associated with the out-of-plane displacements of the sulfur atoms. For monolayer WS_2, a prominent second-order peak ($2LA$ mode) arises and overlaps with E^1_{2g} peak with a ~4 cm^{-1} separation. **Figure 3.2**a-b show the typical Raman spectra of monolayer WS_2 under two different excitation wavelengths.

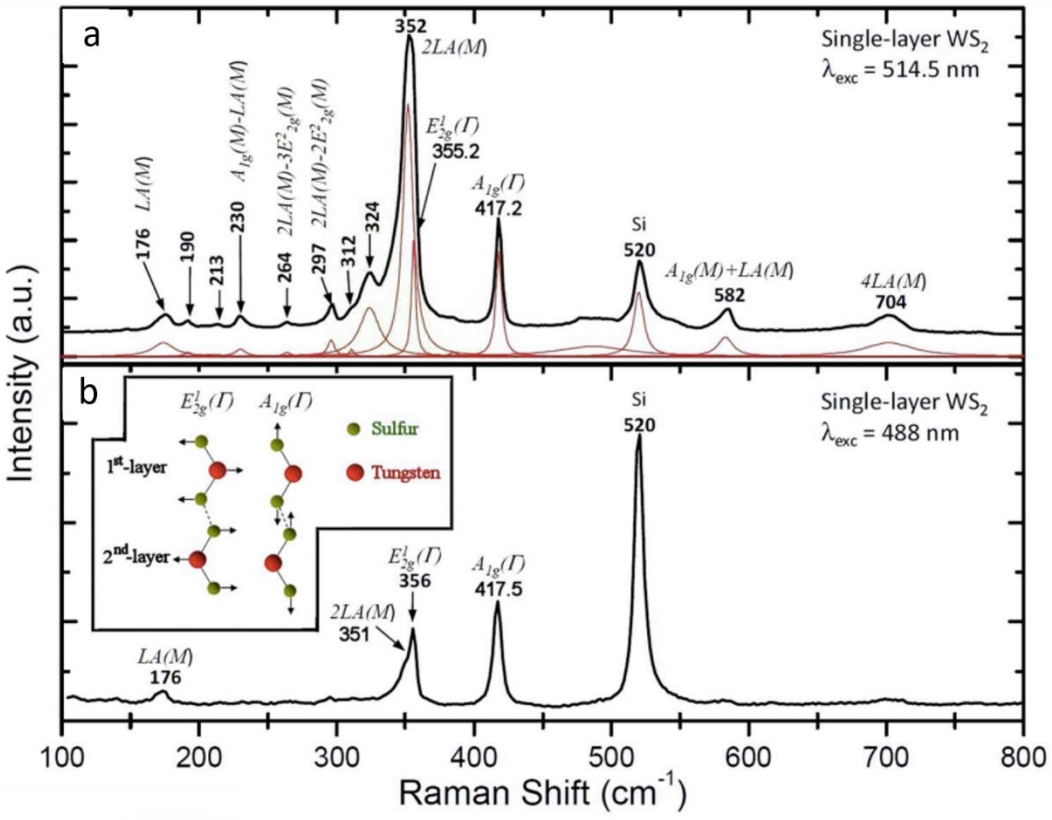


Figure 3.2 Room temperature Raman spectra of monolayer WS_2 acquired using 514.5 nm and 488 nm laser respectively. Red lines in (a) are results of multi-Lorentzian fitting used for separating individual mode contributions. The inset in (b) illustrates the atomic displacements under in-planed E^1_{2g} mode and out-of-plane A_{1g} mode. Adapted with permission[182], Copyright 2013, Macmillan Publishers Ltd.

The frequency difference (Δω) between E^1_{2g} and A_{1g} of TMD has a certain degree of layer dependence and is thus commonly used as an indicator for TMD thickness.[27,182] The layer dependence of Raman spectra and Δω of MoS_2 are shown in **Figure 3.3**a and 3.3b

respectively. As demonstrated by Molina-Sanchez *et al.*,[184] the shift in E_{2g}^{1} phonon frequency with increasing layer can be explained by the stronger dielectric screening of long range Coulomb interaction, while the stiffening of A_{1g} mode can be explained by stronger interactions between sulfur atoms in adjacent layers. It should be noted that considering $\Delta\omega$ alone is not a definitive route for identify layer number of TMDs, as its value may vary with different processes of sample preparation.[179]

According to previous studies, $\Delta\omega$ of monolayer and bilayer WS_2 is around 62 and 64 cm^{-1} respectively.[182,185,186] The $\Delta\omega$ of monolayer MoS_2 are observed to lies within the range of 18-20 cm^{-1}.[27,175,187] $\Delta\omega$ of bilayer MoS_2 is usually reported to be over 21 cm^{-1}.[27,175] These values are used to compare with the CVD-grown TMD crystals studied in Chapter 5 and Chapter 6.

Although following a similar trend, the thickness dependence of $\Delta\omega$ is found to be less pronounced in heavier TMD compounds such as WS_2 and WSe_2, and thus may not serve as an ideal fingerprint for layer number identification.[188] Raman spectroscopy is therefore usually considered along with other characterization techniques such as optical microscopy, AFM, PL and TEM when determining TMD crystals' thickness.[11,27,85,182,188]

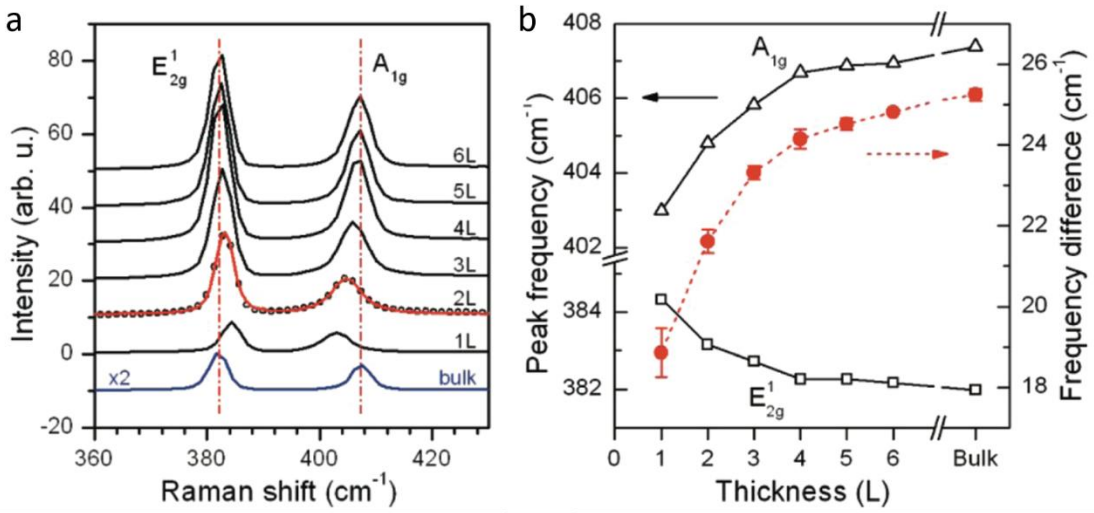


Figure 3.3 Layer-dependent Raman study of MoS_2. (a) Raman spectra of few-layer (nL) and bulk MoS_2. (b) Peak frequencies of A_{1g} and E^1_{2g} mode (left axis) and their frequency difference Δω as a function of layer number. Reprinted with permission.[27] Copyright 2010, American Chemical Society.

The Horiba JY LabRAM ARAMIS spectrometer was used for both PL and Raman acquisition. A 532 nm green laser generated by a frequency-doubled Nd:YAG laser source was used for excitation. Samples were illuminated through a ×50 objective lens with a laser beam spot size of ~5 μm. Other than single spectra acquisition, spatial information of the 2D crystals can also be obtained by scanning the spatial distribution of PL and Raman signals across the crystal domain.

3.3.3 Atomic Force Microscopy

AFM utilizes the subtle changes in van der Waals force between a tip and the sample to provide a profile of the surface topography with atomic resolution.[189–191] Brought into proximity (several nm), the vdW interaction between the tip and sample leads to an attractive force, if the distance becomes even smaller, repulsive force starts to dominate as dictated by Pauli exclusion principle. The vdW forces of varying proximity causes the cantilever to deflect in varying degree. Most AFM systems perform a beam-deflection measurement, where a laser beam is reflected off the back of the cantilever and collected by a position-sensitive photodetector, with an output signal proportional to the degree of cantilever

deflection.[191] In this way, small variations in the vdW force can be amplified and detected, allowing very high sensitivity.

The Asylum Research MFP-3D atomic force microscope was used for AFM measurement in this work. A Cr/Pt plated cantilever with a spring constant of 2.17 N/m and resonance frequency of 67.12 kHz was used. AFM measurements were conducted under the tapping mode, in which the cantilever oscillates at its resonant frequency and taps on the sample periodically. Changes in the vdW interactions cause the oscillation amplitude to change. The height of the tip above the sample is adjusted by a z-piezo to maintain a constant oscillation amplitude throughout each measurement. The voltage applied to the z-piezo can thus be used to reconstruct the topographic profile of the scan.

3.3.4 Electrical and Opto-electrical Measurements

The screening and batch measurements of graphene transistor arrays in Chapter 4 were performed using a HP4156 Semiconductor Parameter Analyzer synchronized with a Cascade Microtech probe station. This set up allows automatic measurements to be carried on hundreds of devices under ambient conditions.

Most electrical and opto-electrical measurements discussed in Chapter 5 and Chapter 6 were performed using a custom-built probe station. A Keithley 2400 source meter was used for measuring *I*-*V* and *I*-V_G characteristics of the devices as FETs. Opto-electrical measurements were done in a similar way with the addition of laser for illumination. A 532 nm diode-pumped solid-state laser (Thorlabs, DJ532-40) that was coupled into a confocal microscope was used as a light source. The power values of the output laser were recorded by a manually fixated power meter (Thorslab Optics PM100D, $\pm$3 % accuracy), placed above the devices before each measurement. Tungsten tips (Signatone SE-T) connected to the source meter were used to probe source and drain bond pads of each device to apply

potential bias, while the back-gate potential was applied directly to the doped silicon substrate from a third terminal for field-effect measurements.

Chapter 4 Doping Graphene Transistors Using Vertical Stacked Monolayer WS_2 Heterostructures Grown by Chemical Vapour Deposition

4.1 Introduction

As discussed previously, 2D crystals can serve as building blocks for new flexible electronics and optoelectronic devices.[15–17] Forming heterojunctions of 2D vdW crystals is a common approach to modulate the electronic properties of the materials for device applications. These heterojunctions based on vdW interactions rather than covalent bonding are not limited by crystal lattice mismatch, offering a wider range of choices in materials systems. Furthermore, the lack of dangling bonds on the monolayer crystal surfaces also enables high quality, atomically regulated interfaces.[135]

To date, multiple studies have investigated the device applications of graphene/TMD heterostructures by artificially stacking the 2D crystals. Reports on TFETs,[192] biosensors,[193] photodetectors and photovoltaic cells,[132,194] have demonstrated the unique electronic properties and enhanced light-matter interactions that the graphene/TMD heterojunctions could offer. Prior investigations have revealed optical and electronic properties of these graphene/TMD heterostructures. In particular, PL quenching on TMDs and a n-doping effect on graphene were observed in the mechanically exfoliated 2D crystals.[195,196] Mechanically exfoliated samples are often free from polymer residue and this enables atomically sharp interfaces between each 2D crystal in the vertical heterostructure. However, the prospect of utilizing mechanically exfoliated samples in commercial applications is small, and this promotes the investigation of similar properties in CVD grown 2D material vertical heterostructures. 2D crystals grown by CVD normally show properties different from their

pristine form due to unintentional doping during growth and transfer process. Obtaining atomically sharp 2D heterointerfaces is more challenging using CVD materials due to residues that may form during transfer. Thus exploring whether such strong interlayer coupling exists in these of vdW crystals grown by CVD is essential for large-scale manufacture and would warrant potential industrial applications for such heterostructures.

In the following, I demonstrate the fabrication of a p^+-p isotype junction on graphene channels utilizing the charge transfer in graphene/WS_2 heterostructure. The doping effect of graphene brought by WS_2 can be further tuned by illumination. Both graphene and WS_2 were grown using CVD method and a total of 220 devices were fabricated. The doping effect on graphene was investigated through examining the transistors' electronic characteristics when altering the spatial coverage of WS_2 on graphene FETs.

The observed surface transfer doping, unlike conventional doping methods of graphene that involves electrostatic modulation,[197–200] chemical interaction,[201] or intercalation,[202] relies on charge transfer between interfaces without introducing significant structural defects to the as-doped material.[203] This finding offers an alternative method to selectively and controllably tune the Fermi level of graphene regions that could potentially form lateral p-n junctions on graphene transistors using other 2D vdW crystals. The doping asymmetry at these junction interfaces are found to be essential for effective photoresponsivity in graphene.[171,204] The controllable doping of graphene proposed in our study may also facilitate researches on the mechanisms of photocurrent generation in graphene-based photodetectors.[205,206] As no additional gate voltage is required in modulating the charge carrier density, the junctions created in our devices using graphene/TMD 2D heterostructure can therefore be applied in fully transparent and flexible photodetectors.[207]

4.2 Results and Discussions

4.2.1 Device Fabrication of Graphene FETs with Vertically Stacked WS_2

Both graphene and WS_2 were grown by CVD methods as described previously in Chapter 3. Graphene/WS_2 hybrid devices were made by transferring graphene onto a silicon chip with 300 nm oxide, pre-patterned with more than 500 pairs of Cr/Au pads that act as source and drain electrodes. The graphene channels are made using EBL patterning and oxygen plasma etching. A WS_2/PMMA film is subsequently transferred on top of the chip containing the graphene channels. **Figure 4.1**a shows a SEM image of one typical device consisting of graphene/WS_2 heterostructures. As the CVD-grown WS_2 crystals are randomly distributed across the region, multiple WS_2 crystals are transferred directly onto the graphene channels, forming vertical heterostructures that have spatially different coverage amounts along the graphene transistors. Figure 4.1b-c show a SEM image with false colour as well as a side view schematic of such a device. The WS_2 domain may extend across the three different surfaces of SiO_2, graphene and gold, allowing further characterization on both graphene transistors as well as the WS_2 domain.

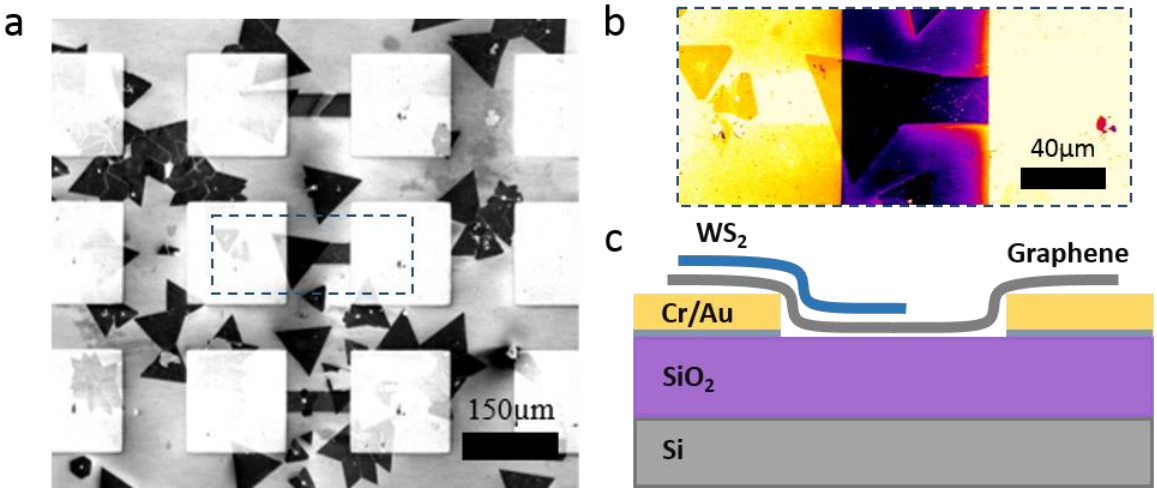


Figure 4.1 PL intensity spatial map of graphene/WS_2 heterostructure. (a) SEM image of devices with graphene channel and vertically stacked WS_2 crystals. Bright square regions are Cr/Au electrodes which are used as source/drain contacts of the graphene FETs. Dark triangular domains are WS_2 crystals. (b) SEM image with false colour of the region indicated in the blue dashed rectangle in (a). (c) Side view schematic of device structure.

4.2.2 Raman & PL Characterization

Monolayer graphene and WS_2 can be confirmed using Raman and PL spectroscopy. The Raman spectra of graphene is shown in **Figure 4.2**a, with a 2D/G ratio of 1.5, showing that the graphene is mostly monolayer. For WS_2, Figure 4.2b shows a strong photoluminescence signal with a peak centered at around 630 nm, indicative of excitonic recombination enhanced by the emergence of direct band gap in monolayer WS_2. This is also confirmed by the Raman spectra in Figure 4.2b inset, under excitation laser with a wavelength of 532 nm, with characteristic peaks of in-plane vibrational mode (E_{2g}^1) and out-of-plane vibrational (A_{1g}) mode occurring at around 350 and 416 (cm^{-1}) respectively. The difference in wavenumbers between the two modes are measured to be around 66 cm^{-1}, which is consistent with previous reports on monolayer WS_2.[169,208]

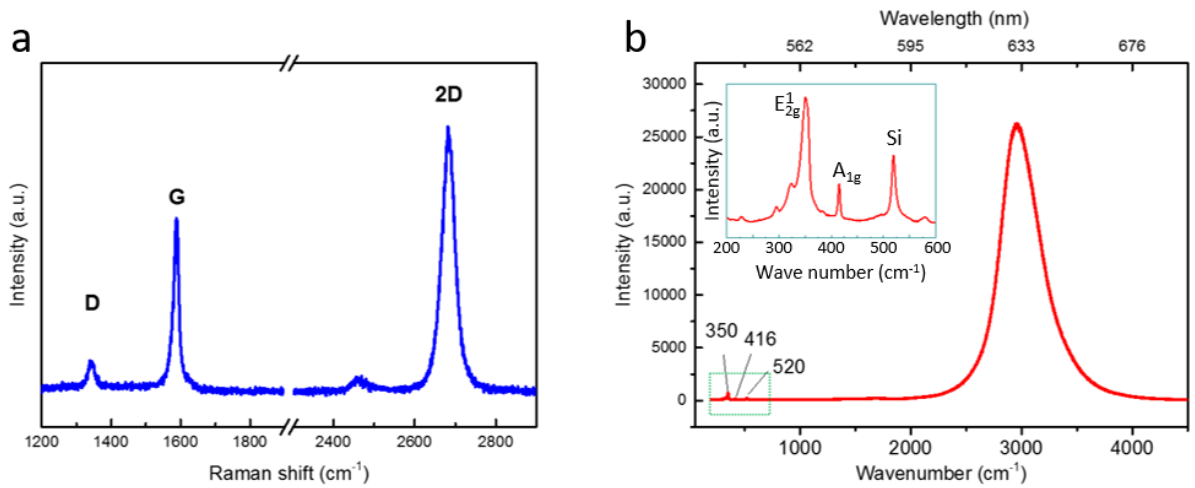


Figure 4.2 Raman and PL characterization of graphene and WS_2. (a) Raman spectra of graphene. (b) PL spectra and Raman spectra (inset) of monolayer WS_2.

The optical image of a WS_2 domain along with its corresponding spatial map of integrated PL signal are shown in **Figure 4.3**a-b. The PL signal drops by over 50 % at the regions where the WS_2 domain lies above the graphene channel and gold electrode. PL quenching occurs when photo-excited carriers on WS_2 are able to transfer onto gold or graphene, resulting in a suppressed recombination process of electron-hole pairs which contributes to the PL signal. This phenomenon agrees well with previous reports on the quenching effects at metal-semiconductor interfaces of 2D crystals.[195,209] The quenching of PL is an indicator that a good contact between graphene/WS_2 vertical stacks are formed.

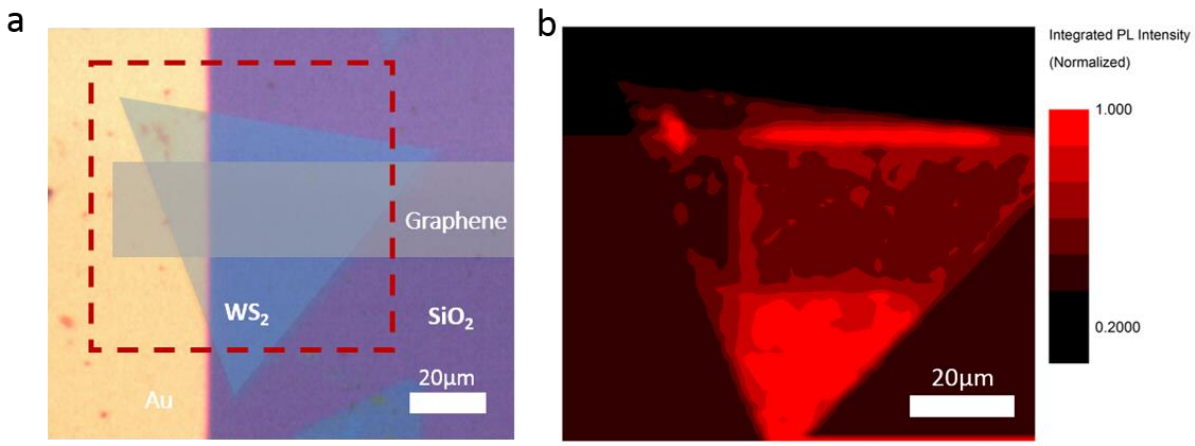


Figure 4.3 PL intensity spatial map of graphene/WS_2 heterostructure. (a) Top view optical image of the graphene FET device with WS_2 partial coverage, with added colour overlay to help identify the different regions. (b) Spatial map of the integrated PL intensity of WS_2 in the red dashed rectangle in (a).

Figure 4.4a shows the PL peak position map of the same heterostructured region shown in Figure 4.3. A blue shift of PL signal is observed when the WS_2 domain lies above the graphene ribbons. The PL peak signals of WS_2 on graphene and SiO_2 substrates are plotted for further analysis in Figure 4.4b. Using Lorentzian fitting, the main peak of photoluminescence signal can be deconstructed into two separate peaks, attributed to the exciton (X) and negative trion (X^-) emission with corresponding photon energies of around 2.01 eV and 1.97 eV respectively. The energy difference of around 40 meV in the two peak positions is attributed to the binding energy of excitons to form negatively charged trion, which is consistent with previous reports of trion binding energy ranging from 20 to 40 meV.[210–212] For WS_2 on the graphene ribbons (*i.e.* the vertical heterostructured region), the spectral weight of negative trion emission decreases relative to that of the exciton peak (Figure 4.4b), suggesting that electrons are depleted from WS_2 within the region. The PL measurements in Figure 4.3 and Figure 4.4 demonstrate a significant interaction between the WS_2 and graphene layer that results in changes in the local charge carrier densities.

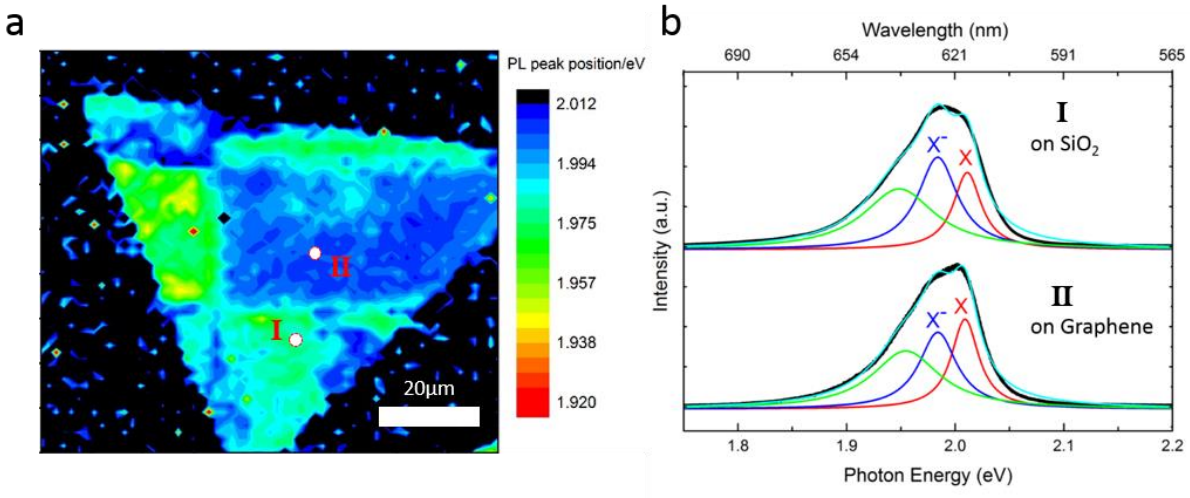


Figure 4.4 PL composition analysis of graphene/WS_2 heterostructure. (a) Spatial PL peak position map of WS_2 in heterostructure device. (b) PL spectra of WS_2 domain on Si substrate and graphene. Lorentzian fitting was used to decompose the PL peak to compare the spectral weight of negative trion (blue curve) and exciton (red curve).

4.2.3 Field Effect Measurements of Graphene FETs

To further explore the interlayer coupling of WS_2 and graphene, the electronic properties of graphene FETs are examined. **Figure 4.5** shows the change in field-effect measurements of graphene channels with different levels of WS_2 coverage. The CVD-grown graphene on SiO_2 substrate has a Dirac point at around 70 V, which is a typical value among the CVD-grown graphene measured and indicative of p-doping. When graphene is partially covered by a WS_2 crystal, a second Dirac point at back gate potential of ~20 V is observed. The appearance of two Dirac points in the gate sweeps suggests electron transfer from WS_2 to graphene, which reduces the level of p-doping of the graphene at the heterostructured region, forming a lateral separation on the graphene channel with different Fermi levels. When graphene is fully covered by WS_2 domains, the entire graphene channel has reduced p-doping compared to uncovered graphene and only one Dirac point is observed in the gate sweeps at much lower voltages.

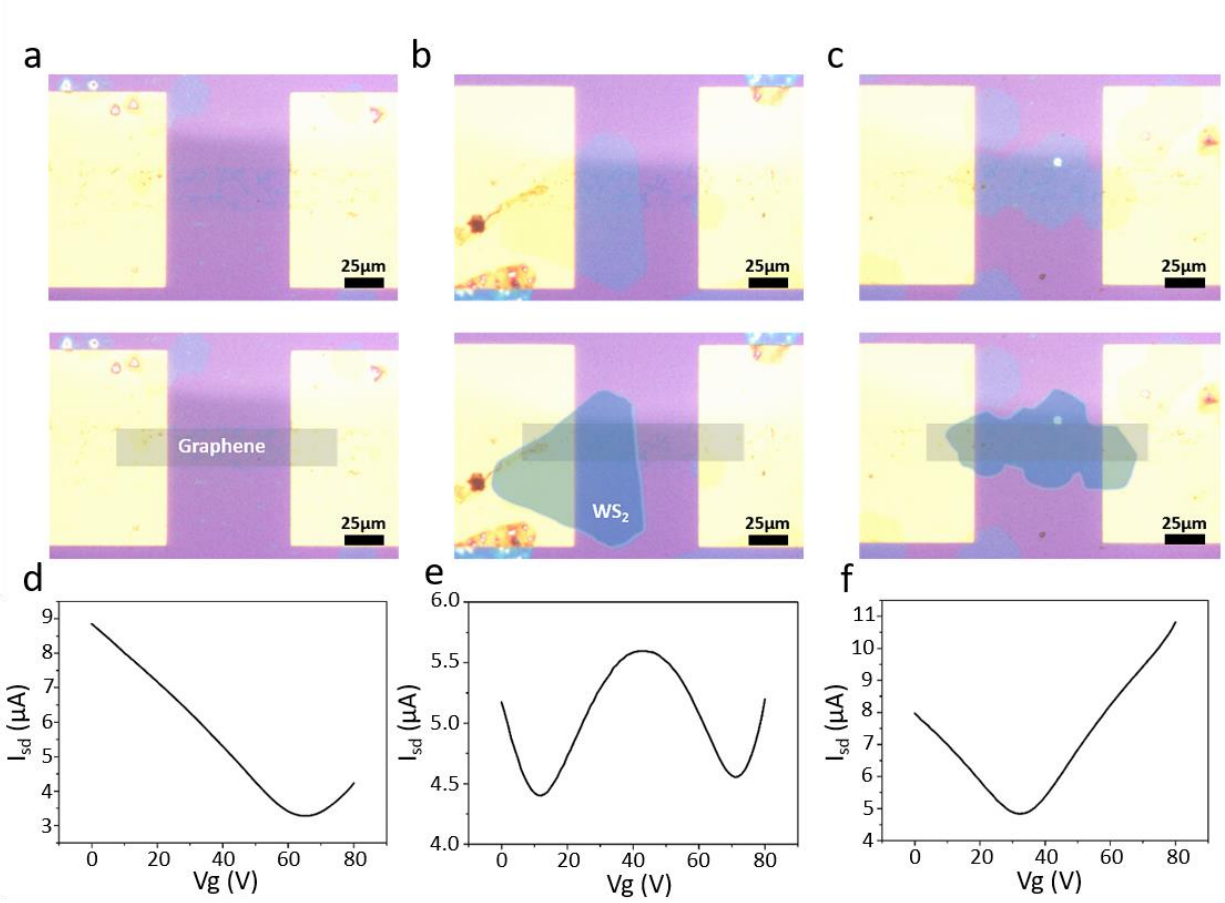


Figure 4.5 Gate dependence of graphene FETs. (a-c) Optical images with added schematic of 3 different types of graphene channels according to WS_2 coverage (no coverage, partial coverage and full coverage). (d-f) are corresponding field effect measurements of the different graphene transistors.

To investigate the relationship of Dirac point positions and the coverage of WS_2 on graphene channels, I studied a total of 220 graphene FET devices with variable WS_2 coverage. The graphene FETs can be classified into three different types, which are graphene channels without WS_2 coverage, graphene channels that are fully covered with WS_2, and graphene channels with partial WS_2 coverage. The average value of the Dirac point positions and the standard deviation are shown in **Table 4.1**. Compared with uncovered graphene channels and channels that are fully covered by WS_2 domains, graphene channels which are partially covered by WS_2 have corresponding Dirac points of around the same position at around 70 V and 20 V. This suggests that the difference in WS_2 coverage on graphene does

not affect the positions of Dirac point significantly, but rather affects the relative weighting contribution of the two Dirac points in the gate sweeps.

Table 4.1 Dirac point position of 3 types of graphene channels.

Graphene channels	No. of devices	Dirac point position (V) (average ± s.d.)
No WS_2 coverage	93	70.9 ± 6
Full WS_2 coverage	12	22.9 ± 10.7
Partial WS_2 coverage (a)	115	76.9 ± 8.9
Partial WS_2 coverage (b)	115	22.2 ± 8.2

4.2.4 Electronic Model of Laterally Separated Graphene FETs

4.2.4.1 Series Circuit Model for Laterally Separated Graphene Channel

The explanation to the existence of a double Dirac point in partially WS_2 covered graphene FETs can be given by a model where two resistors are connected in series as shown in **Figure 4.6**a. The overall channel resistance in such a configuration would be the sum of the contact resistance and two laterally separated graphene regions, one covered with by WS_2 and the other without, expressed as R_{w} and R_{g} respectively. The total channel resistance (R_{T}) of the graphene can therefore be expressed using the equation $R_{\mathrm{T}} = k \cdot R_{\mathrm{w}} + (1-k) \cdot R_{\mathrm{g}} + R_{\mathrm{C}}$, where k is the percentage area of WS_2 coverage on graphene channel, R_{C} the contact resistance, and R_{w}, R_{g} the resistance of doped graphene covered by WS_2 and plain graphene respectively.

Figure 4.6b shows a schematic illustration of the band structures of these two graphene regions under different applied back gate potentials. The doped graphene reaches its neutrality point at around +20 V, transitions from p-type towards a n-type transistor with increasing positive gate potential, while the uncovered graphene that is initially more p-doped reaches neutrality point at a larger back gate potential of around +70 V.

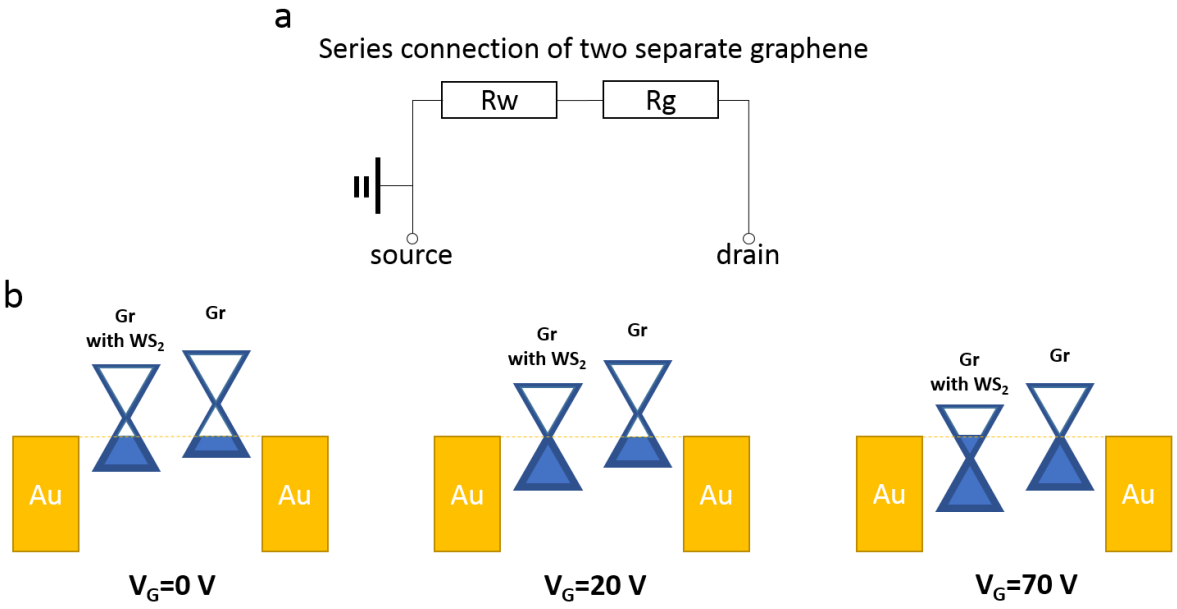


Figure 4.6 Series circuit model of laterally separated graphene channel. (a) Simplified resistance model of graphene channel where R_w and R_g, which represent the resistance of doped and un-doped graphene respectively, are series connected within the transistor channel. (b) Schematic illustration of band structure of the two distinct graphene regions under different applied back gate potential.

4.2.4.2 Graphene Electron-Hole Puddle Model

To understand in quantitative terms how the resistance of graphene changes according to applied gate potential, a model is introduced to account for the electron-hole puddle density, which was used in previous reports on double Dirac points on graphene transistors.[199] The total charge carrier concentration of either holes or electrons on graphene are approximated using the equation $n_{\mathrm{T}} = \sqrt{{n_0}^2 + {n_{\mathrm{G}}}^2}$, where n_0 is the residual charge carrier density while n_{G} is the carrier concentration induced by the back-gate electric field. n_G can be further determined by gate electrostatic potential using $e \cdot n_{\mathrm{G}} \cdot L \cdot w = C_{\mathrm{ox}} \cdot$

$(V_G - V_{CNP})$, where e is the elementary charge unit, L and w the channel length and width respectively, C_{ox} is the oxide capacitance, V_G the applied back-gate potential, and V_{CNP} the position of graphene charge neutrality point, also known as Dirac point. In this way, our measurement can be fitted using the equation:

$$R_T = R_C + k \cdot \frac{A_1}{\sqrt{1+\frac{(V_G - V_{CNP})^2}{{B_1}^2}}} + (1-k) \cdot \frac{A_2}{\sqrt{1+\frac{(V_G - V_{CNP})^2}{{B_2}^2}}} \quad \textbf{(Eq. 4-1)}$$

where R_C is the contact resistance, k the coverage percentage of WS_2 on graphene channel, $A = \frac{L}{w \cdot e \cdot n_0 \cdot \mu}$ and $B = \frac{e \cdot t \cdot n_0}{\varepsilon}$. Using **Eq. 4-1**, the fitting parameters (*i.e.* contact resistance R_C, residual charge carrier density n_0, charge carrier mobility μ) can be obtained. The excellent agreement between the measured channel gate-sweep characteristics and modelled curves shown in **Figure 4.7**d-f confirmed the local tuning of graphene's Fermi level due to transfer of electrons from WS_2 onto graphene.

The p-doping of CVD-grown graphene is often attributed to charge impurities unintentionally introduced by substrates, polymer residual and absorbents under ambient conditions.[213] Reports have shown that the encapsulation of graphene using TMDs and other 2D crystals remove the absorbed water molecules by a vdW self-cleaning process,[214,215] and thus a less p-doped graphene would be expected with transfer of WS_2 on graphene. However, this does not seem to be the main mechanism for what is observed in our graphene-WS_2 heterostructure.

In the statistical analysis of charge carriers derived from the fitting results of 115 graphene devices with double-Dirac points using the proposed models, the concentration of residual charge carriers (n_0) of graphene with WS_2 coverage is on average 1.85×10^{12} cm^{-2}, while graphene without WS_2 coverage has 1.15×10^{12} cm^{-2}. It can be concluded from the fitting results that the residual charge carrier density of graphene have in most cases increased after the stacking of WS_2 domains. This suggest that the main reason for the

observed n-doping of graphene is more likely to be an introduction of charge carriers rather than just a cleaning process via the removal of absorbed gas and water molecules, which would have resulted in a more pristine graphene with a lower residual charge carrier.

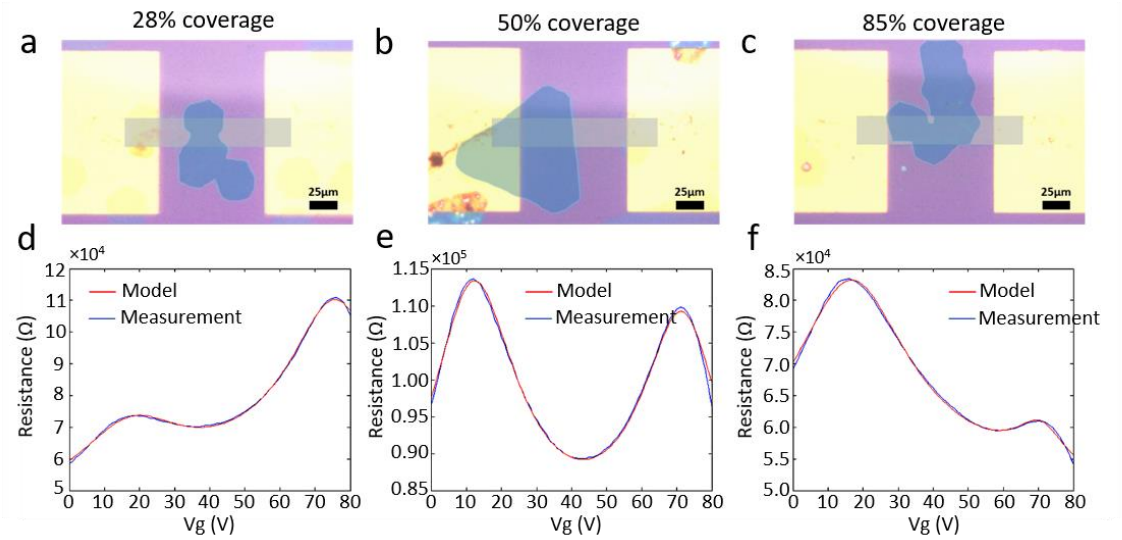


Figure 4.7 Modelled results *versus* experimental results of different graphene FETs. (a-c) Optical images with added schematic of graphene channels with 28%, 50% and 85% WS_2 coverage. (d-f) Corresponding field effect measurements and simulated resistance using model.

4.2.5 Photo-induced Charge Transfer of Graphene-WS_2 Interface

The observed charge carrier transfer is found to be further induced via photo-irradiation on the heterostructured region. **Figure 4.8**c demonstrates gradual shift of Dirac point of graphene under increasing illumination. The field effect characteristics of the graphene transistors with partial WS_2 coverage is highly responsive to the input laser power. However, the two Dirac points, which are attributed to the WS_2-doped region and uncovered graphene respectively, shift at different rates with increasing laser power, resulting in a split of the two Dirac points (Figure 4.8d). This suggests that graphene is further n-doped from photo-excited carriers transferring from the WS_2/graphene under illumination. This photo-induced charge transfer between WS_2/graphene also corresponds well with the PL quenching observed at the WS_2/graphene interface. The splitting of photo-excited electron-

hole pairs at the interface, where electrons are transferred to the graphene and holes reside at the WS_2, essentially prohibits the radiative recombination process and results in quenching of PL signal.

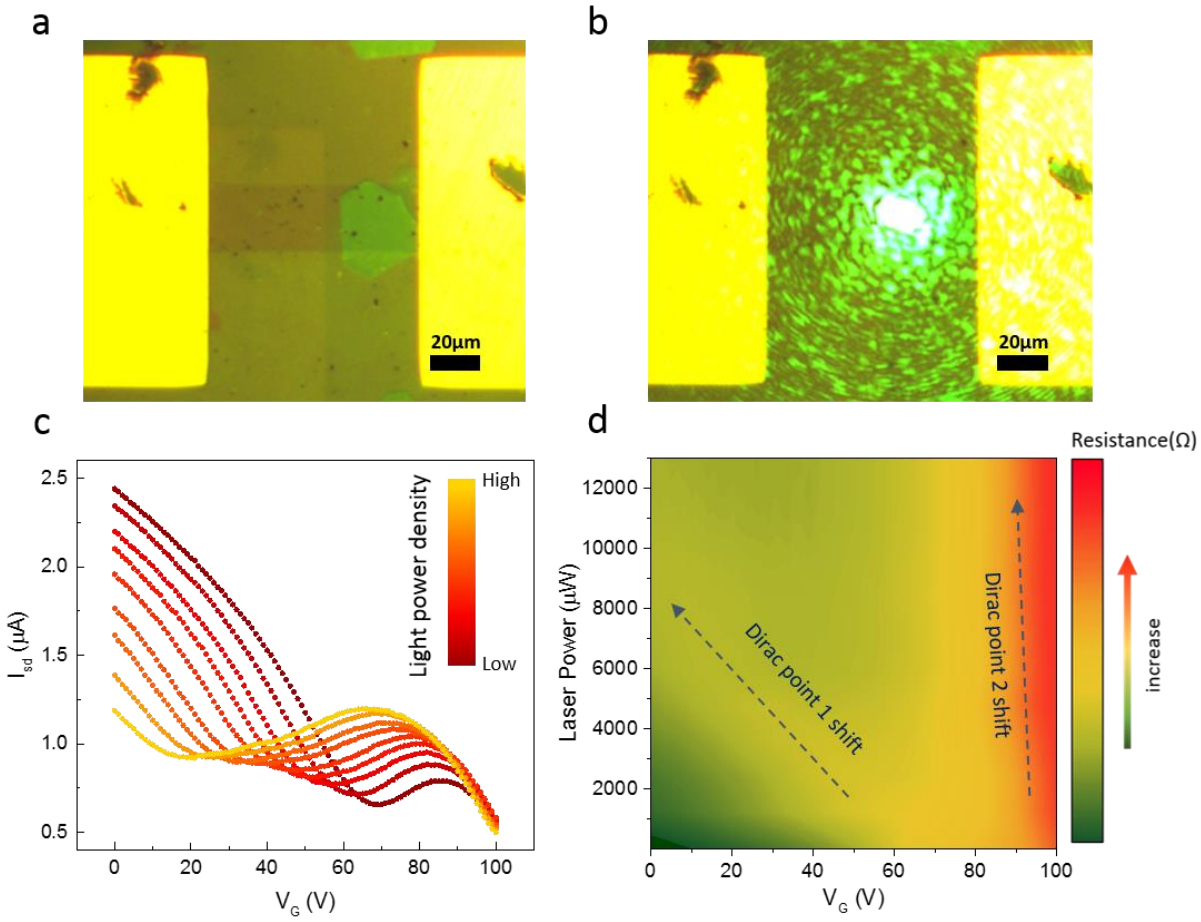


Figure 4.8 Photo-irradiation of WS_2/graphene interface. (a) Optical image of a graphene transistor partially covered by WS_2. (b) Optical image of device illuminated with 532 nm laser. The laser is centered at the edge of the WS_2 domain so that both graphene and heterostructured region are illuminated. (c) Field effect measurement device under increasing laser power. (d) Contour plot of the resistance of graphene channel in response to the illumination power and applied back-gate voltage.

4.3 Conclusion

In summary, graphene/WS_2 vertical heterostructures were created using all CVD grown materials and characterized the interlayer coupling of the vdW crystals using optical spectroscopy and electronic measurements. Strong quenching of the PL is observed for WS_2 on graphene, indicative of strong interactions between the two layers, which is also

supported by the electronic transport measurements of graphene and the photoinduced doping effect. By only partially covering graphene with WS_2, it is possible to locally modulate the doping of graphene and construct graphene FETs with double-Dirac points. Our work shows that CVD grown WS_2 can be transferred on top of the graphene and still exhibit strong interactions in both optical and electronic properties. The doping effect can be further modulated by controlling the laser power illuminating the heterostructure. This opens up the possibility of large scale device fabrication based on all CVD materials that cannot be achieved with 2D materials isolated by mechanical exfoliation. Our findings can serve as ground work for novel photodetectors using surface charge transfer between 2D crystals.

4.4 Contribution Statement

Dr. Ye Fan provided training in device fabrication and established the software interface for electrical characterization. Dr. Youmin Rong provided CVD-grown WS_2 for this study. Dr. Zhengyu He built up the opto-electrical measurement platform and provided constructive comments for analysis of spectroscopy (Raman and PL) results.

Chapter 5 Ultrathin 2D Photodetectors Utilizing Chemical Vapour Deposition Grown WS_2 with Graphene Electrodes

5.1 Introduction

A critical challenge in fabricating high-quality scalable opto-electronics with 2D TMDs is making optimized metal contacts without damage or the introduction of Fermi level pinning at the interface that causes large Schottky barrier formation.[97,216] The contact resistance at the metal-semiconductor interface is often a dominating factor in TMD based electronic devices and the ability to control this interface is essential to realizing the full potential of scalable 2D TMD based electronics.[217]

To date, substantial research has been carried on MSM structured devices to investigate the contact properties between TMD and different metal electrodes.[97,147,216] However, not many studies have incorporated graphene as an electrode into these MSM devices. While prior studies have focused mainly on the electronic applications such as FETs and logic gate,[105,106,218] the opto-electronics characteristics such as the photosensing capabilities of a graphene-TMD-graphene lateral photodetectors have yet to be fully explored.

Unlike bulk metals such as Ti and Au, which are conventionally used as electrodes in TMD based electronics, graphene is highly stable and chemically inert, thus act as ideal contacts in the absence of diffusion and reaction with TMD crystals.[219] Due to graphene's finite density of states, the Fermi level of graphene can be tuned for low contact resistance[220] or even a barrier-free contact with a semiconductor.[221] For this reason, successful

modulation of graphene's work function has been achieved by applying a back-gate potential,[222] electrical stressing,[199] or through defect engineering [202] and molecular doping of graphene that relies on surface charge transfer within heterostructures.[196,223–226] In this study graphene-WS_2-graphene photodetectors are fabricated using all CVD grown materials and examine their behavior.

5.2 Results and Discussion

5.2.1 Device Fabrication of graphene-WS_2-graphene Photodetectors

Figure 5.1a depicts the flow chart of the device fabrication process. Details of the fabrication process is previously described in Chapter 3. As shown in Figure 5.1b, CVD-grown WS_2 crystals are randomly distributed across the region after the transfer process, and we select the devices with WS_2 domains transferred at the center of each device, bridging the gap between the graphene electrodes, together forming a graphene-WS_2-graphene lateral photodetector. Figure 5.1c shows an SEM image of such a device. To better understand and characterize the performance of the photodetectors, device channels with two different lengths (200 nm and 5 µm) are made, as shown in Figure 5.1d-e, and explored the difference between layer number(s) (monolayer *versus* bilayer). Among the CVD-grown WS_2 there are a majority of monolayer domains, but also a small number of bilayer regions, which naturally lead to a distribution of photodetector devices containing each of these types of domains. From the 500 devices on a 1 cm^2 silicon chip, about half of them have sufficient graphene coverage to make working electrodes.

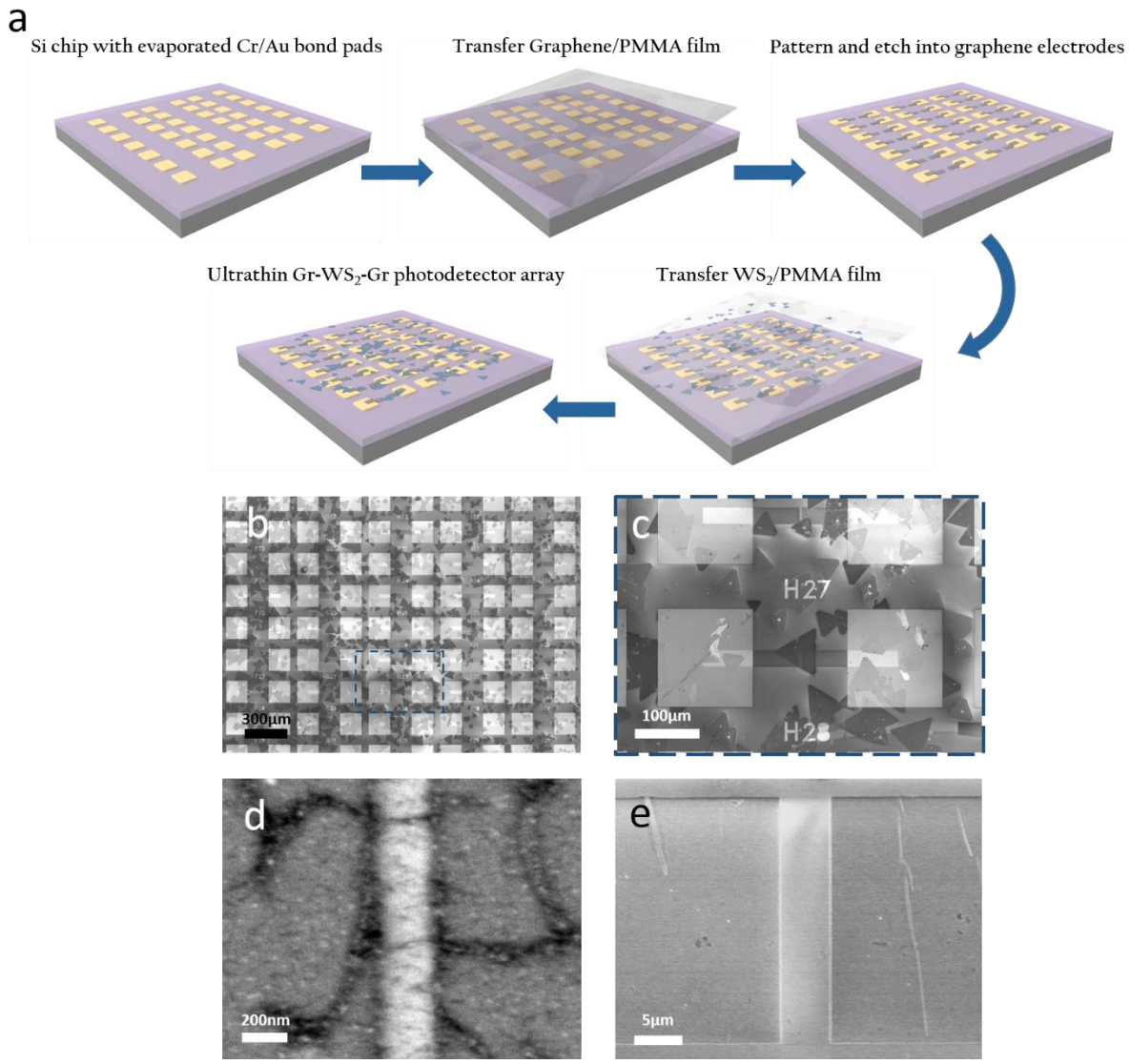


Figure 5.1 Fabrication and characterization of graphene-WS_2-graphene photodetector array. (a) Fabrication process schematic of the photodetector array. (b) SEM image of fabricated photodetector arrays. (c) Enlarged image of framed region (blue dotted line) in (b) of a graphene-WS_2-graphene device. (d) SEM image of graphene electrode with a 200 nm wide gap. (e) SEM image of graphene electrode with a 5 μm gap. The gap between the electrodes determine the channel length of the device.

The subsequently transferred WS_2 step yields a ~ 20 % success rate, which allows us to characterize as many as 50 graphene-WS_2-graphene devices per chip, which is more than suitable for investigations on the fundamental study of the photodetectors' performances. It is also worth noting that the thinnest of the devices fabricated are based on

monolayer graphene and WS_2, resulting in extreme thinness of 2 nm as characterized with an AFM topographical scan (**Figure 5.2**).

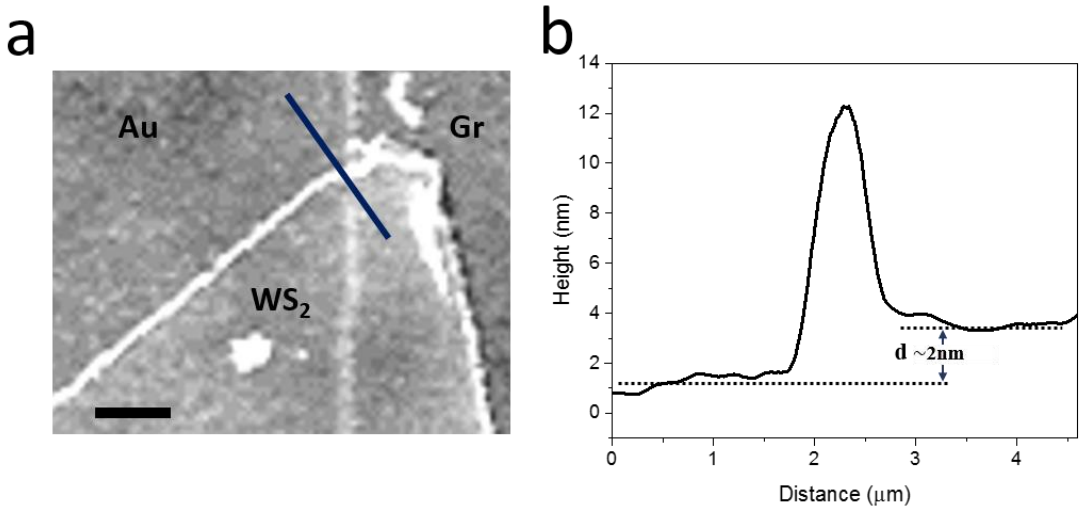


Figure 5.2 AFM profile of graphene-WS_2 heterostructure. (a) AFM image of WS_2 domain on graphene channel transferred onto SiO_2/Si chip with pre-patterned bond pads. Scale bar represents 2μm**.** (b) Line profile of blue line in (a).

5.2.2 Raman & PL Characterization

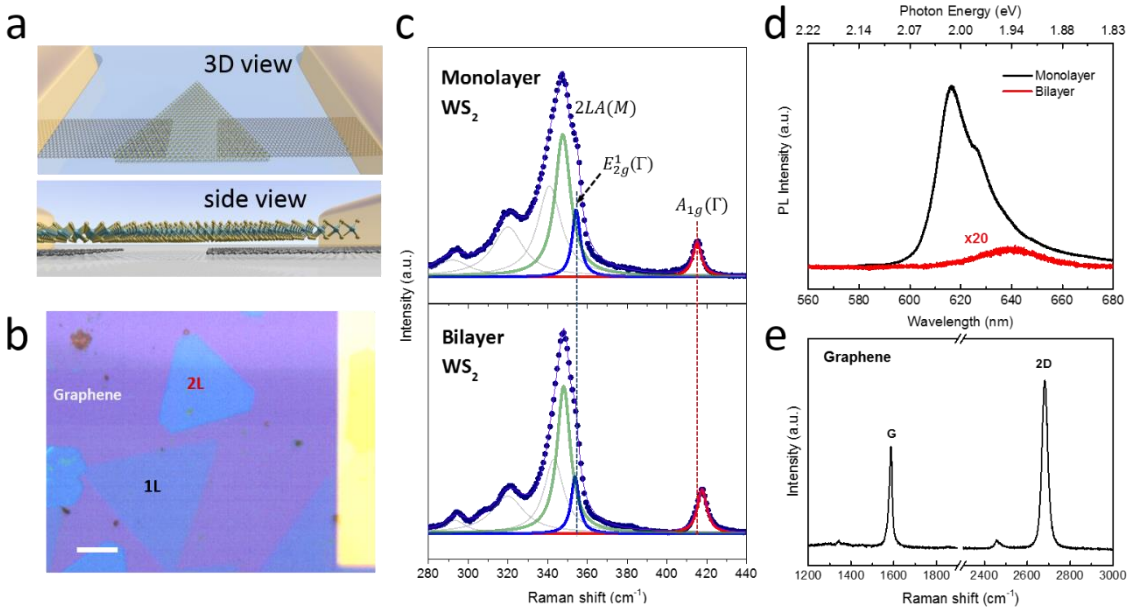


Figure 5.3 Raman and PL characterization of CVD-grown WS_2 and Graphene. (a) Schematic 3D and side views of graphene-WS_2-graphene photodetector (b) Optical image showing graphene, monolayer WS_2 and bilayer WS_2. Scale bar represents 20 μm (c) Raman spectra of monolayer and bilayer WS_2 under 532 nm laser. A multi-Lorentzian curve fitting of the spectra shows signature peaks of the WS_2 crystal, labeled fitted curves include the $2LA(M)$ (green), $E^1_{2g}(\Gamma)$ (blue) and $A_{1g}(\Gamma)$ (red) peaks. (d) PL spectra of monolayer and bilayer WS_2. The emission signal of bilayer WS_2 is magnified by 20 times. (e) Raman spectra of graphene electrodes. A prominent 2D peak serves as indication of monolayer graphene.

Raman spectroscopy and PL measurements are used to determine the quality and layer numbers of the CVD-grown crystals. **Figure 5.3**a shows a perspective view schematic of a graphene-WS_2-graphene photodetector. An optical image of the sample includes a graphene electrode connected to bilayer WS_2, and a monolayer domain beside the device (Figure 5.3b). By optimizing the contrast of the optical image, one can easily differentiate a monolayer from a bilayer WS_2 domain. Figure 5.3c shows the Raman spectra of both monolayer and bilayer WS_2 under green laser with λ=532 nm. A multi-Lorentzian curve fit was performed to extract the composition peaks attributed to the different vibrational modes within the 2D systems. Here, the analysis focuses on the signals of in-plane $E^1_{2g}(\Gamma)$, out-of-plane $A_{1g}(\Gamma)$, and vibration second-order $2LA(M)$ modes, which are commonly used to determine the thickness of WS_2 crystals.[182,227,228] In monolayer WS_2, the fitted peaks of $E^1_{2g}(\Gamma)$ and $A_{1g}(\Gamma)$ modes are positioned at 354.4 and 415.2 cm^{-1} respectively. As of their counterpart in bilayer, the $E^1_{2g}(\Gamma)$ mode was softened, positioning at 353.8 cm^{-1}, while the $A_{1g}(\Gamma)$ mode experienced stiffening and blue-shifts to a position of 417.7 cm^{-1}, agreeing with previous reports.[182,228] Comparing the frequency difference between the two modes, we find Δω of monolayer and bilayer samples are 60.8 and 63.9 cm^{-1} respectively. This is in good agreement with the reported values in previous studies.[182,185,186] Additionally, the peak intensity ratio of $2LA(M)/A_{1g}(\Gamma)$ rises from 4.3 to 6.2 as layer number decrease from bilayer to monolayer, a trend consistent with a previous layer-dependent Raman study.[182]

PL spectra of both crystals further support this finding, showing prominent PL signal generated from the monolayer WS_2 and little emission from bilayer due to the transition of direct to indirect band gap as layer number of WS_2 increases. The Raman spectra of graphene (Figure 5.3e) shows a 2D/G peak intensity ratio of around 1.5, suggesting that the CVD-grown graphene consists mostly of monolayer regions.[25]

5.2.3 Opto-electrical Characterizations of graphene-WS_2-graphene Photodetectors

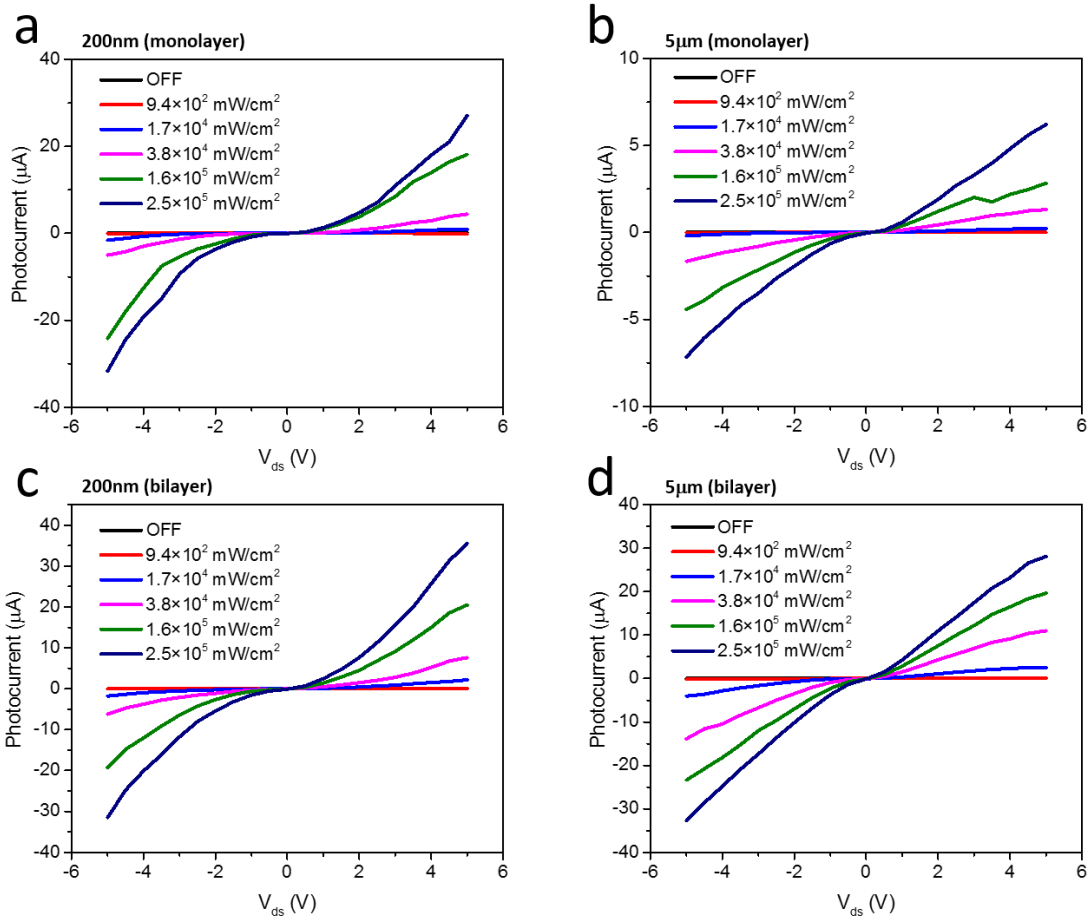


Figure 5.4 Bias dependent photocurrent of graphene-WS_2-graphene photodetectors. (a-d) Photocurrent of four types of devices with varying WS_2 channel length and layer numbers. 532 nm light was used for illumination.

To understand how layer number and channel length affect the photo-generated current, *I-V* measurements are carried on the devices under five different illumination intensities. **Figure 5. 4**a-d show the plots of photocurrent *versus* the applied source-drain voltage on devices from all four groups. The *I-V* plots show a non-linear curve, indicative of Schottky contacts at the metal-semiconductor interface of graphene and WS_2.

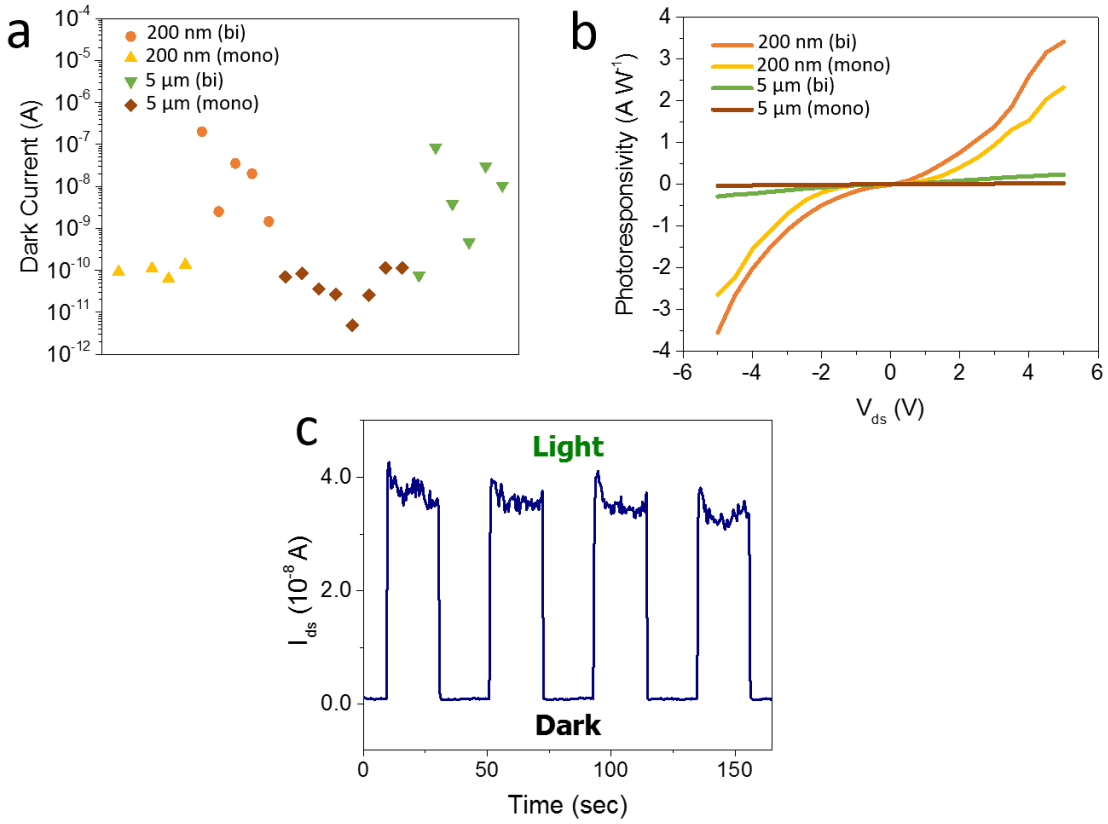


Figure 5.5 Photoinduced current and dark current of graphene-WS_2-graphene photodetector. (a) Dark current distribution of different types of devices under bias of +5 V. (b) Photoresponsivity of the four types of detectors under an incident light density of 3.8×10^4 mW cm^{-2}. (c) Transient photocurrent characteristics obtained from a device (200 nm, monolayer) under bias of +2 V with an incident light density of 3.8×10^4 mW cm^{-2}.

Figure 5.5a depicts the distribution of the dark current of twenty-three photodetectors of all four groups under an applied bias of +5 V. It is observed that the layer number of WS_2 has a large influence on the dark current of each devices. Though the dark current of devices in each category may fluctuate largely, the difference between dark current in monolayer and bilayer WS_2 is clear, with the dark current of bilayer WS_2 to be around 10^{-8} A, which is two orders of magnitude larger than the monolayer's dark current of 10^{-10} A.

To explain the lower resistance of bilayer WS_2 under dark conditions, the following reasons should be considered. Firstly, we take into account the lower resistance brought by an extra channel for carrier transport through the second layer. The doubling of thickness

more than halves the total resistance compared to the monolayer, possibly due to the low resistance edge contact formed between top layer WS_2 and graphene.[217] Secondly, we consider the passivation effect brought by the top layer of WS_2 as a capping layer. Encapsulation of the bottom WS_2 layer would isolate it from extrinsic impurities that would otherwise be introduced under direct exposure of ambient conditions,[115,117,118] which would lead to higher carrier mobility due to dielectric screening.[131]

Photoresponsivity (R), photoconductive gain (G) and specific detectivity (D^*) are important figures of merit in evaluating a photoconductor's performance. Photoresponsivity is a measure of a device's electrical response to incident light, defined as:

$$R = \frac{I_{\text{photo}}}{P_{\text{laser}}} \qquad \textbf{(Eq. 5-1)}$$

where I_{photo} is the measured photocurrent, and P_{laser} is the collected illumination power. Figure 5.5b shows the calculated R of the four types of devices as a function to V_{ds}, under an incident power density of 3.8×10^4 mW cm^{-2}. In all four types of devices, R increased with a larger applied bias, with the largest measured value under a 5 V bias to be over 3.5 A W^{-1} for a bilayer WS_2 device and 2.5 A W^{-1} for monolayer device with short channel length of 200 nm.

In photoconductors, external photoconductive gain (G_{ext}) is defined as the number of photogenerated charge carriers (either electrons or holes) that are collected at the electrodes divided by the number of incident photons on the photoconductor. The relationship of external photoconductive gain and photoresponsivity can be described by the following expression:

$$R = G_{\text{ext}} \cdot e/h\upsilon \qquad \textbf{(Eq. 5-2)}$$

where G_{ext} is the external photoconductive gain, e is the elementary charge unit, h is the Planck's constant and v is the incident photon frequency. We obtain G_{ext} to be as high as 9.3 and 5.8 for bilayer and monolayer devices respectively.

Specific detectivity (D^*) characterizes a photodetector's sensitivity by taking into account the bandwidth, geometry and noise of the device.[137] It is given by $D^* = \frac{R\times(Af)^{1/2}}{i_n}$, where A is the effective area of the detector, f is the electrical bandwidth, and i_n is the noise current. The noise current i_n of photodetectors comes from three main sources: thermal noise, shot noise and *1/f* noise. Thermal noise arises from the fluctuations of current caused by thermal movement of carriers.[229] Shot noise stems from the statistical uncertainty of the electron arrival rate, and is associated with the direct current flowing across potential barriers.[229] It exists in the form of $I_{SN} = (2eI_{dark})^{1/2}$. *1/f* noise has a 1/f dependence and is thus more pronounced under a frequency range below 1 kHz. It is associated with the random trapping and release of carriers by interfacial trap states.[230] For a fast estimation, we assume a low thermal noise and calculate the shot-noise-limited specific detectivity using the following expression:[131,147,231]

$$D^* = RA^{1/2}/(2eI_{dark})^{1/2} \qquad \textbf{(Eq. 5-3)}$$

where I_{dark} is the measured dark current. From **Eq. 5-3** we obtain the shot-noise-limited detectivity of our photodetectors to be 1.6×10^{10} Jones for bilayer devices and 9.9×10^{10} Jones for monolayer devices (Jones = cm $Hz^{1/2}$ W^{-1}). It should be noted that low-dimensional device possess large 1/f noise which should not be neglected.[232,233] The estimation of a shot-noise-limited detectivity may therefore overestimate the true detectivity of 2D photodetectors by a few orders of magnitude under low frequency range (<1 kHz).[137]

Figure 5.5c shows the time-resolved photoresponse of a monolayer WS_2 device with 200 nm channel length. At a fixed bias of +2 V, reproducible low and high impedance states were obtained by switching repeated on-off cycles of light irradiation, with an ON/OFF ratio (defined as I_{photo}/I_{dark}) of 54, allowing such device to act as a high quality photosensitive switch. These photodetectors with graphene electrodes, showing high photoresponsivity and photogain under ambient conditions with zero applied gate potential, are comparable and in many cases outperform reported TMD-based photodetectors with metal electrodes.[129,130,140,141,143,146,234,235] It is worth noting that the photocurrent measurements in this study are carried under an incident light power density as high as ~10^5 mW cm^{-2}, which is a high power intensity compared to intensities used in previous reported measurements.[129,140,235] Under previously reported low excitation power range, a common observation in photodetector study is that photoresponsivity monotonously decreases with the increase of incident power, explained by the shortening of exciton recombination times due to the concomitant increase of generated electron-hole pairs[146] and the influence of trap states between gate oxide and the semiconductor.[127] It is thus necessary to find the possible reasons for the high photoresponsivity of our device under larger illumination power.

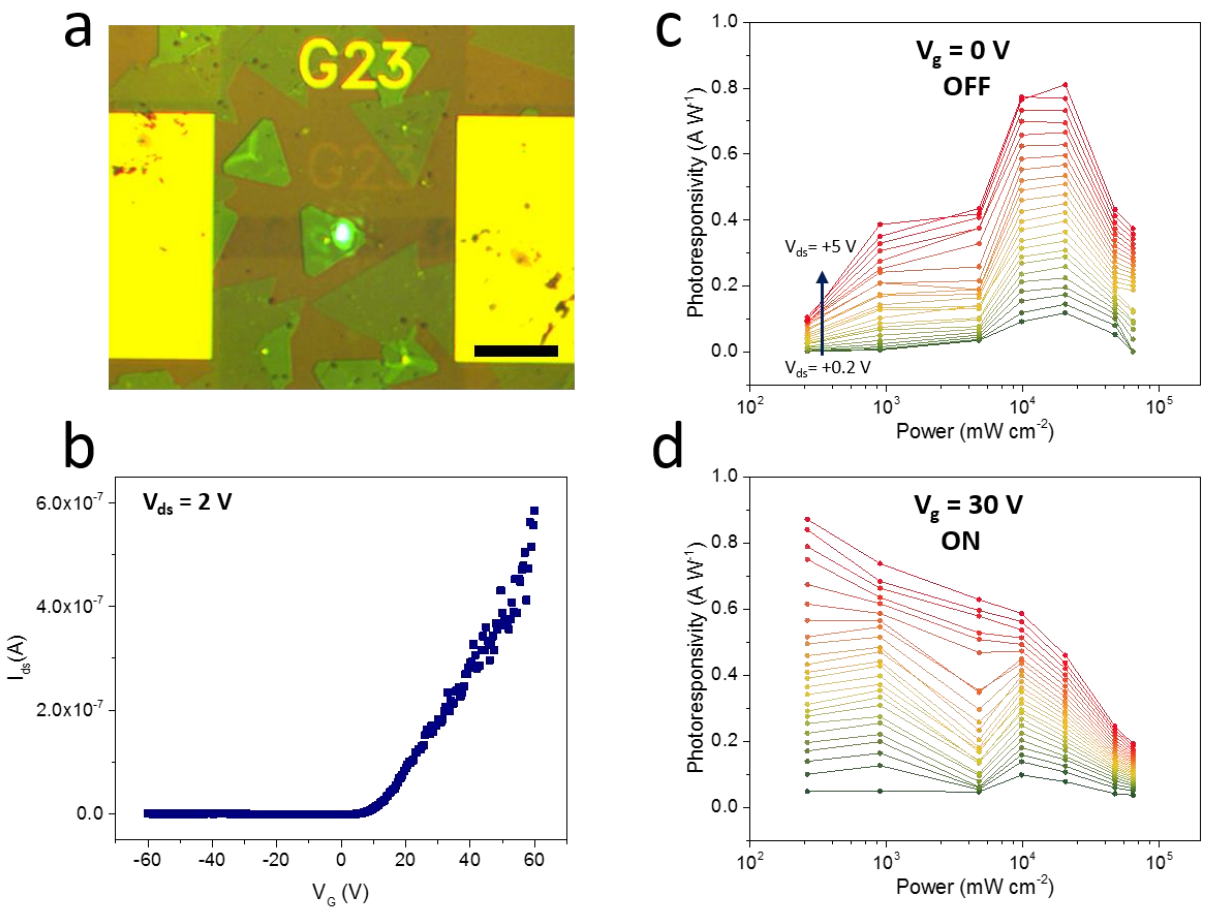


Figure 5.6 Photoresponsivity of WS_2 under influence of gate and illumination power. (a) Optical image of a bilayer WS_2 device illuminated by 532 nm laser. Scale bar represents 50 µm (b) Field effect of a bilayer WS_2 phototransistor. I_{ds}-V_G plot shows the n-type characteristics of the device with a threshold voltage V_{th} of ~10 V. (c-d) Photoresponsivity of bilayer WS_2 device as a function of incident light power under back gate potential of 0 V (OFF state) and 30 V (ON state) respectively.

Figure 5.6a shows an illuminated bilayer WS_2 device (5 µm channel length) that was used for gate and power dependence study. We investigate its photoresponsivity under varying applied gate potential as well as illumination power. A gate sweep measurement was carried first to show the field effect characteristics of the device. As shown in Figure 5.6b, the *I-V* plot shows an n-type transistor with a threshold voltage (V_{th}) of ~10 V. A power dependence study was subsequently carried with a back gate voltage of 0 V and +30 V, under which the phototransistor is tuned to its OFF and ON state respectively. Shown in Figure 5.6c-d, the photoresponsivity of the device show different power dependence pattern under its OFF state and ON state. Under 0 V, photoresponsivity first increases along with

enhanced illumination, from 0.1 A W^{-1} under incident power density of 2×10^2 mW cm^{-2} and reaches a maximum value of 0.8 A W^{-1} at a power density of 2×10^4 mW cm^{-2}. Beyond this point, photoresponsivity starts to decrease with enhanced illumination power. This power dependence trend of graphene-WS_2-graphene photodetector's responsivity is very different compared with the behavior of an Au-WS_2-Au photodetector, which decreased monotonously with increasing incident power (Figure 5.9d). Under 30 V, when the graphene-WS_2-graphene transistor is switched into its ON state, the photoresponsivity then starts to follow a negative correlation with illumination power, exhibiting the highest photoresponse under the lowest applied laser power density of 2×10^2 mW cm^{-2}. Based on our recent findings on light-induced charge transfer between graphene and WS_2,[226] we propose that such an increase in photoresponsivity with enhanced incident light can be attributed to the unique contact between graphene and WS_2.

The presence of the Schottky contact can be confirmed from the nonlinear *I-V* curve of the graphene contacted devices. Schottky barrier results from the band alignment at the metal-semiconductor interface. When the two 2D crystals are brought into contact, electrons pass from n-type WS_2 to p-type graphene, forcing their Fermi levels to align. This creates negative charge on graphene at the heterointerface which n-dopes the graphene (as shown in Chapter 4), and leaves balancing positive charge at the WS_2, which bends its energy band upwards, forming the potential barrier.[218,236] The output characteristics of the device can be described by a modified theory for thermionic emission current through the Schottky barrier. Using a simple model of a back-to-back Schottky diode pair in series, the current of the device can be described using the following set of equations:[237,238]

$$I = I_0 \cdot exp[-\left(1-\frac{1}{n}\right)e\beta V_1] \cdot [exp(\,e\beta V_1) - 1] \qquad \textbf{(Eq. 5-4)}$$

$$I = \frac{V_2}{R} \qquad \textbf{(Eq. 5-5)}$$

$$I = -I_0 \cdot exp[\left(1 - \frac{1}{n}\right) e\beta V_3] \cdot [exp(\ -\ e\beta V_3) - 1] \quad \textbf{(Eq. 5-6)}$$

$$U = V_1 + V_2 + V_3 \quad \textbf{(Eq. 5-7)}$$

where I is the source-drain current, U is the applied voltage bias, I_0 is a constant determined by Schottky barrier height, n is the ideality factor, $\boldsymbol{e}$ is the elementary charge unit, and $\beta = \frac{1}{k_B T}$ is the Boltzmann factor, V_i ($i = 1,2,3$) are the voltage drop across the left diode, middle resistor and right diode. By solving **Eq. 5-4** to **Eq. 5-7**, we obtain the relation between the drain current and applied voltage bias:[239]

$$I = I_0 \left[\frac{cosh\left(\frac{1}{2}\left(1-\frac{1}{n}\right)e\beta(U-IR)\right)}{cosh\left(\frac{1}{2n}e\beta(U-IR)\right)}\right]^{-\left(1-\frac{1}{n}\right)} \cdot \frac{sinh\left(\frac{1}{2}e\beta(U-IR)\right)}{cosh\left(\frac{1}{2n}e\beta(U-IR)\right)} \quad \textbf{(Eq. 5-8)}$$

By fitting the *I-V* curves with equation **Eq. 5-8**, I_0 can be obtained, which is the thermionic current associated with the Schottky barrier of the 2D WS_2 ,which can be described using the following expression:[240,241]

$$I_0 = wA_{2D}^{*}T^{3/2} \cdot \exp(-\beta e\Phi_{SB_eff}) \quad \textbf{(Eq. 5-9)}$$

where w is the contact width of graphene, A_{2D}^{*} is the 2D equivalent of Richardson constant,[241] T is the temperature, and Φ_{SB_eff} is the effective Schottky barrier height. The effective Schottky barrier height can then be calculated by taking the fitting parameter I_0 into **Eq. 5-9**. An example of the fitted curve along with the measured *I-V* result is shown in **Figure 5.7**. The measurement was performed on a bilayer WS_2 transistor with an applied gate voltage of V_G = 70 V.

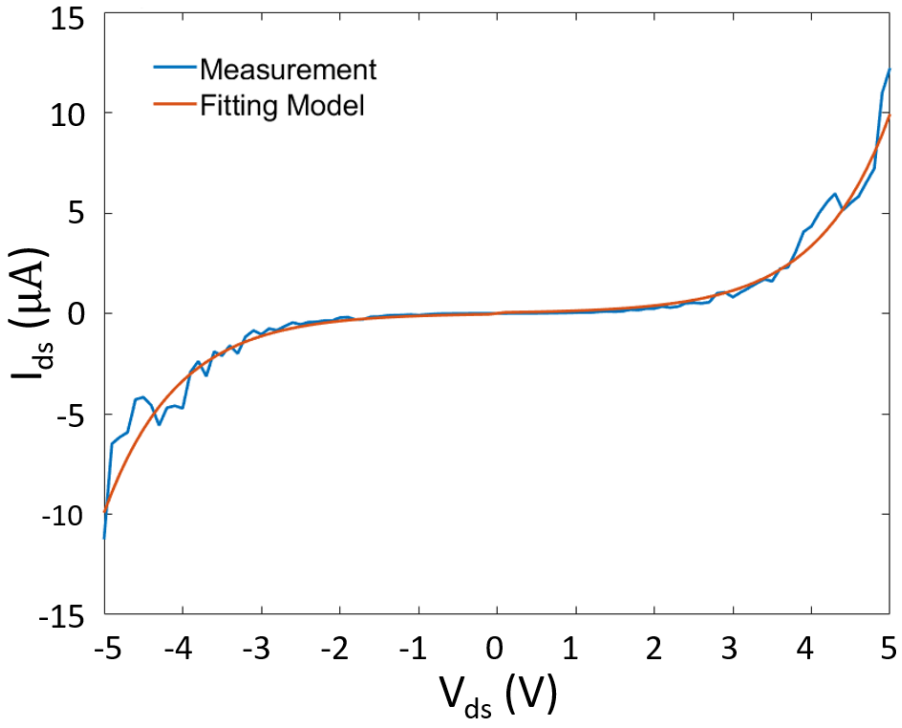


Figure 5.7 Fitting *I-V* curve of graphene-WS_2-graphene transistors using back-to-back Schottky diode model.

Figure 5.8a-c show the band structure schematic of the graphene-WS_2 interface at a non-equilibrium condition. It has been well documented that the resistivity of a metal-semiconductor contact is greatly influenced by the Schottky barrier formed at its heterojunctions.[25] Under the assumption of the Schottky-Mott rule,[25] the height of the Schottky barrier (Φ_{SB}) is determined by the band offset at the graphene/WS_2 interface, which can be expressed as $\Phi_{SB} = \Phi_{Gr} - \chi_{WS_2}$, where Φ_{Gr} is the work function of graphene (~4.6 eV)[222] and χ_{WS_2} the electron affinity of WS_2 (~4.0 eV).[242] Thus a Schottky barrier height of $\Phi_{SB} = 0.6$ eV between graphene and WS_2 can be estimated. As positive gate potential is applied, electrons are induced in graphene which should cause a decrease in graphene's work function, resulting in a lowering of barrier height (Figure 5.6b).

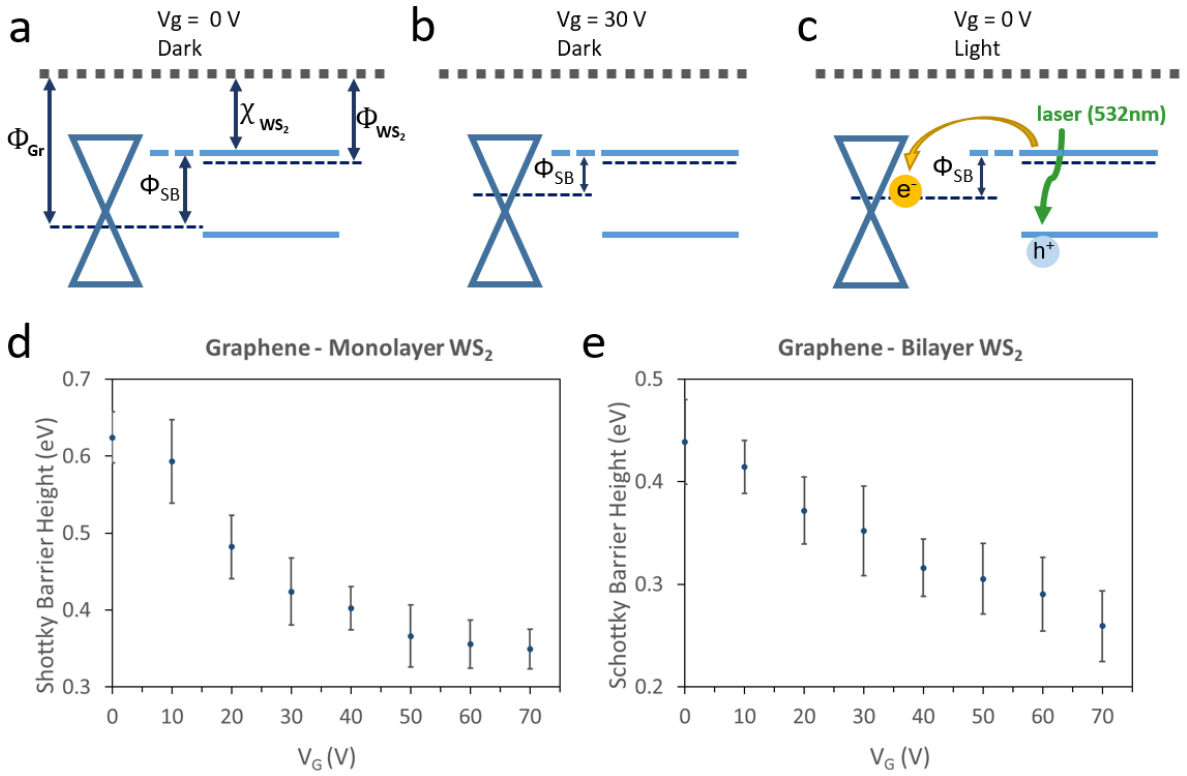


Figure 5.8 Mechanism for photoresponsivity increase with added positive gate and illumination power. (a,b,c) Schematic of band diagram of graphene/WS_2 heterostructure under non-equilibrium condition, depicting the work function of graphene Φ_{Gr} and electron affinity of WS_2 χ_{WS_2} relative to vacuum level under different back gate potential and illumination conditions. Both positive applied gate potential and illumination of the heterostructured regions cause Fermi level of graphene to rise, which results in the lowering of graphene-WS_2 Schottky barrier Φ_{SB}. Calculated effective Schottky barrier height as a function of back gate potential V_G for (d) Graphene-monolayer WS_2, and (e) Graphene-bilayer WS_2. The effective height of Schottky barrier monotonically decreases with increasing positive gate potential.

Using the back-to-back Schottky diode fitting model, it is found that the obtained Φ_{SB_eff} monotonously decreased with increasing positive gate potential, and under V_G = +70 V, reached a minimum value of 0.33 eV and 0.26 eV for monolayer and bilayer devices respectively (**Figure 5.8**d-e). This modification of the Schottky barrier for graphene-TMD contacts due to the tunable work function of graphene has been observed in prior reports and is therefore expected here as well.[164,196,220,236] To explain the light modulated photoresponsivity, we turn to the photo-induced charge transfer in graphene/WS_2 heterostructure which has been observed in a previous study.[226] This surface charge transfer process generates layer-separated electron-hole pairs, with electrons residing in graphene and holes located in WS_2, resulting in the n-doping of graphene (Figure 5.8c). This would

increase the Fermi level of graphene and lower the contact resistance of the photodetector. It is proposed that this photo-gating mechanism could serve as an explanation for our devices' improved photoresponsivity under high illumination power. Once the graphene-WS_2-graphene phototransistor is switched into the ON state under an applied gate potential larger than V_{th}, the influence of illumination on the Fermi level is reduced and thus results in a different power dependence of photoresponsivity shown in Figure 5.6c-d.

5.2.4 Comparative Study with Au-WS_2-Au Photodetectors

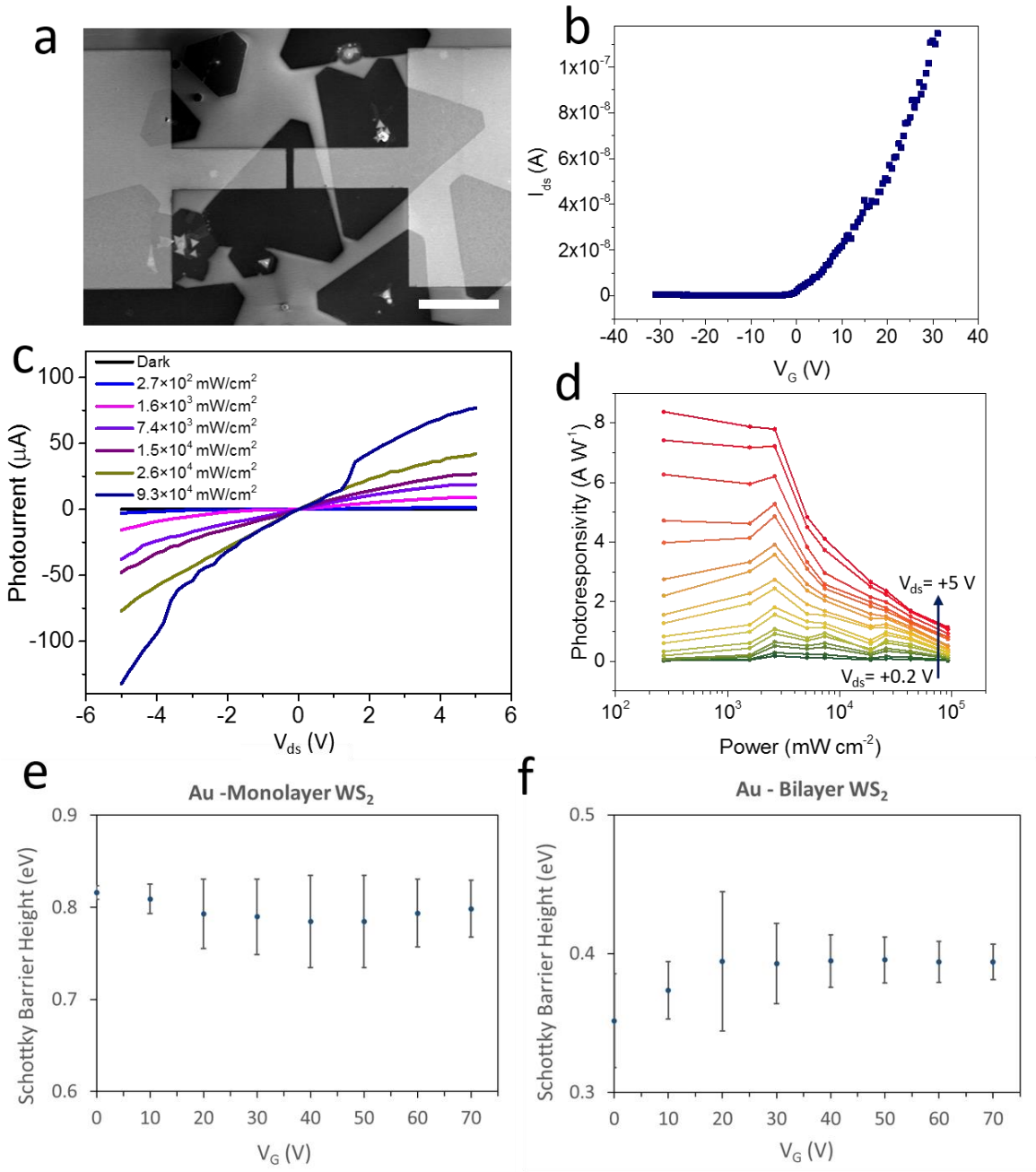


Figure 5.9 Characteristics of an Au-WS_2-Au photodetector. (a) SEM image of an Au-WS_2-Au device with the same geometry as the reported graphene-WS_2-graphene devices. Scale bar represents 50 μm. (b) Field effect of a bilayer WS_2 phototransistor with gold electrodes. I_{ds}-V_G plot shows the n-type characteristics of the device with a threshold voltage V_{th} of ~5 V. (c) Photocurrent of a bilayer Au-WS_2-Au photodetector. (d) Photoresponsivity *versus* incident light power of a bilayer WS_2 photodetector under 0 V gate potential. Calculated effective Schottky barrier height as a function of back gate potential V_G for (e) Au - monolayer WS_2, and (f) Au - bilayer WS_2. Unlike the Schottky barrier of graphene-WS_2, the effective Schottky barrier height does monotonously decrease with increasing back gate potential, this can be attributed to the high density of states of bulk metal and possible Fermi level pinning at the Au-WS_2 interface caused by trap states.[239]

Au-WS_2-Au transistors were fabricated to compare with the measurement results of graphene-contacted photodetectors. An SEM image of an Au-contacted device is shown in **Figure 5.9**a. Figure 5.9b shows the gate sweep measurement which reveals the n-type characteristics of the transistors. The photocurrent measurement is shown in Figure 5.9c, and calculated photoresponsivity *versus* light power shown in Figure 5.9d. It can be observed that unlike the graphene contacted samples, photoresponsivity of an Au-contacted device decreases monotonously with increasing light power. Figure 5.9e-f shows the obtained effective Schottky barrier height Φ_{SB_eff} for both monolayer and bilayer WS_2 devices over varying gate potentials. Both types of devices show that the Φ_{SB_eff} between Au-WS_2 stayed relatively the same over increased positive gate, suggesting that contact resistance of the device is unlikely to be influenced by electrostatic gating. Consequently, one is to expect photogating to play a lesser role in Au-WS_2-Au photodetectors' photocurrent generation process.

5.3 Conclusion

In summary, I have demonstrated the fabrication of ultrathin lateral MSM WS_2 photodetectors using graphene as electrodes. To the best of my knowledge this is the first case in which lateral photodetectors are made entirely from 2D materials grown by CVD, eliminating mechanical exfoliation from the process. The graphene-WS_2-graphene photodetectors exhibit high photoresponse reaching ~3.5 A W^{-1} under ambient atmosphere and high input visible light at 532 nm. The outstanding performance of the device can be attributed to the modulation of the Schottky barrier between graphene and WS_2 under an applied gate and increased illumination power. It can be concluded that graphene electrodes serve as an ideal medium for carrier transport for MSM photodetectors, with a gate and light tunable contact resistance with WS_2 owing to its limited density of states, and enhanced photoresponsivity under increasing illumination power due to efficient light-induced charge

transfer between graphene and WS_2. This interesting behavior could lead to new designs of photodetectors that can maintain a high photoresponse under strong light power detection.

5.4 Contribution Statement

Dr. Ye Fan provided the Au-WS_2-Au control group samples and introduced the back-to-back diode fitting model for Schottky barrier analysis. AFM measurement was carried out by Dr. Benjamin Porter. WS_2 crystals were provided by Miss Yingqiu Zhou and Miss Wenshuo Xu, and graphene was provided by Miss Qu Chen.

Chapter 6 Graphene-contacted WS_2/MoS_2 Hybrid Photodetectors with Large Gain Utilizing Interlayer Charge Transfer

6.1 Introduction

The understanding of interlayer coupling dynamics between 2D materials is essential for better control and design of vdW heterostructure devices. Recently, multiple studies have reported the ultrafast interlayer charge transfer between TMDs, which occurs within a picosecond upon photo-excitation at the heterostructured regions.[153,243] This phenomenon is commonly observed in TMD heterostructures with type-II band alignments.[244–247] The charge transfer between TMDs is known to first form layer-separated electron-hole pairs with excess energy, or hot excitons, as intermediate states before forming tightly bound excitons. The excess energy leads to a lower binding energy and longer electron-hole pair distance compared with tightly bound excitons,[243] which are conducive for dissociation into free charge carriers and may lead to enhanced photocurrent generation. Moreover, studies on TMD heterostructures reveal that interlayer excitonic lifetimes of heterobilayers are over an order of magnitude larger than intralayer excitonic lifetimes,[244,248] implying a long photocarrier lifetime essential for large photoconductive gain. In this way, artificially designed TMD heterostructure is a promising option for ultrathin photodetectors that could outperform monolayer or bilayer TMD crystals by higher light sensitivity.

So far, reports on opto-electronics based on TMD heterostructures have focused mainly on vertical architectures with staggered metal contacts sandwiching 2D heterostacks.[134,135,164,249] Less studied are devices with lateral MSM configurations that involve two or more vdW crystals. This may be due to the difficulty of selective patterning

of 2D crystals without damaging its adjacent layer, or the complicated lithography procedures required to overcome it. Further work is needed to integrate the vertical 2D semiconducting heterostructures with laterally-spaced graphene electrodes to assemble high performance ultrathin devices suitable for electronics and opto-electronics.

In this study, lateral MSM devices based on graphene-contacted WS_2/MoS_2 heterostacks are fabricated and their opto-electronic properties are characterized. This is achieved by using the wet transfer method as described in Chapter 3 to address the aforementioned fabrication challenge. Using this transfer process, arrays of pre-patterned graphene electrodes and metal bond pads can be transferred onto target substrates with pre-transferred TMD domains. The wafer-scale batch transfer of electrodes allow us to fabricate arrays of hybrid TMD devices consisting of a WS_2 layer and MoS_2 layer sandwiching graphene electrodes, *i.e.* a graphene lateral contact to a WS_2/MoS_2 heterostructure. Electrical/opto-electrical measurements are conducted on the lateral graphene-WS_2/MoS_2-graphene devices and compared with other TMD monolayer and bilayer devices.

6.2 Results and Discussions

6.2.1 Device Fabrication

A schematic illustration of a fabricated bilayer TMD device is shown in **Figure 6.1**a. Lateral photodetectors are produced with TMD (A)/TMD (B) sandwiching a pair of graphene electrodes. The TMD bilayer stack bridges a one micron gap between the two graphene (source and drain) electrodes, and thus forms a MSM device with a 1 μm channel length. The main steps for fabricating such a lateral photodetector is shown in Figure 6.1b. TMD (A) is first transferred onto a silicon chip with a 300 nm oxide layer (Figure 6.1b, i). On a separate chip, Au bond pads and graphene electrodes are fabricated using EBL and oxygen plasma for selective etching. The Au/graphene electrodes are subsequently transferred onto the piece of silicon chip with pre-transferred TMD (A) domains (Figure 6.1b, ii). For bilayer devices, this is then followed by an additional transfer of TMD (B) to form a TMD bilayer photodetector array (Figure 6.1b, iii-iv). This study includes 5 types of devices for comparison, with stacking configurations shown in Figure 6.1c. Figure 6.1d is an optical image of one of the fabricated arrays based on WS_2/MoS_2 heterobilayer, and Figure 6.1e shows an enlarged image of one of the devices consisting of WS_2 and MoS_2 domains with graphene electrodes.

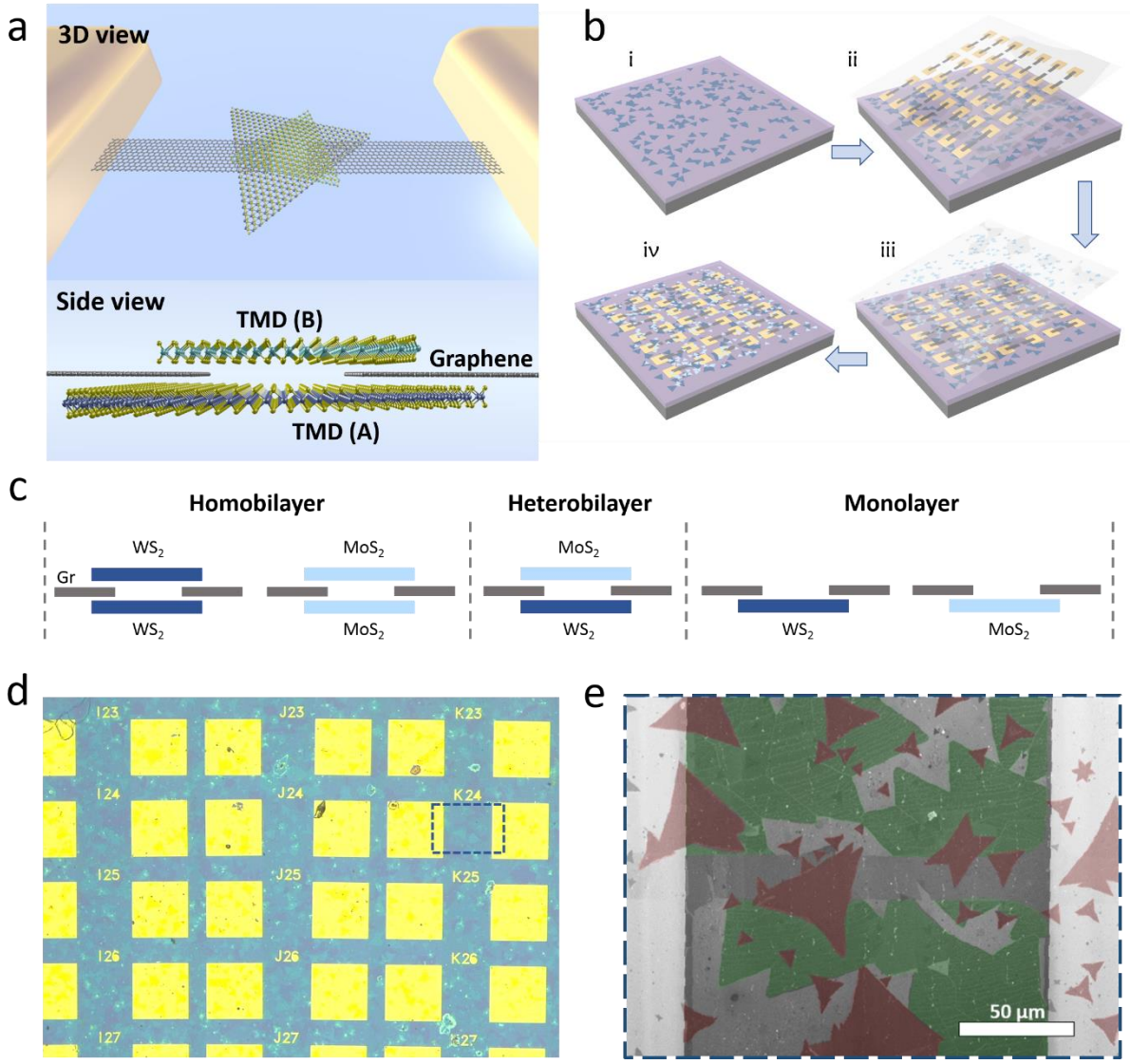


Figure 6.1 Fabrication schematic and images of hybrid WS_2/MoS_2 photodetector array. (a) Schematic 3D and side views of graphene-WS_2/MoS_2-graphene photodetector. (b) Fabrication process schematic of graphene-TMD-graphene photodetector array. Using PMMA thin film support, pre-patterned Au bond pads and graphene electrodes are transferred onto silicon chip with pre-transferred TMD (A) domains. For bilayer devices, an additional layer of TMD (B) crystals are subsequently transferred onto the same chip. (c) Configuration schematic of the 5 types of photodetectors designed for this experiment, including WS_2/MoS_2 heterobilayer, homobilayer and monolayer of WS_2 and MoS_2. (d) Optical image of a heterobilayer photodetector array consisting of WS_2 and MoS_2 contacted by graphene electrodes. (e) SEM image with added false color of framed region (blue dotted line) in (d) showing a hybrid photodetector with MoS_2 (red) and WS_2 domains (green) with graphene contacts (dark grey).

6.2.2 Raman and PL Analysis of WS_2/MoS_2 Heterostructure

Raman and PL spectroscopy are used to characterize layer numbers and quality of the 2D crystals. **Figure 6.2**a shows the PL measurements of monolayer of WS_2, MoS_2 and WS_2/MoS_2 heterobilayer. Compared with monolayer WS_2, the PL signal dropped by 59.2% at the WS_2/MoS_2 heterobilayer region, suggesting a suppressed recombination of photo-excited electron-hole pairs within the heterobilayer due to interlayer charge transfer. However, the PL signal of WS_2/MoS_2 heterobilayer is still larger than that of monolayer MoS_2. This can be explained using first-principle calculations of a prior study,[245] which indicates that interactions between WS_2 and MoS_2 layers would form an indirect band gap at the WS_2 layer yet retain a direct band gap for MoS_2. The result would be a compromise of the photoluminescence quantum yield in WS_2 but not in MoS_2.

Figure 6.2b shows the Raman spectra of the WS_2/MoS_2 heterobilayer. Using Lorentzian fitting, compositional peak are determined and attributed to the vibrational modes within the 2D systems. Peaks corresponding to in-plane (E_{2g}^1) /out-of-plane (A_{1g}) vibrations of WS_2 and MoS_2 are found to be positioned at 353 cm^{-1}/417 cm^{-1} and 384 cm^{-1}/404 cm^{-1} respectively. The $\Delta\omega$ of WS_2 and MoS_2 are calculated to be 64 and 20 cm^{-1} respectively, consistent with the reported values of 63.8 and 20 cm^{-1} of a previous study on as-transferred WS_2/MoS_2 heterobilayer.[186] It is noted that the $\Delta\omega$ of WS_2 in this study is larger than most reported values (~62 cm^{-1}) of monolayer WS_2.[177,182] While this may be the true $\Delta\omega$ value of monolayer WS_2 within the heterostructure, there is also a possibility that the presence of 2LA mode has affected the accurate determination of the E_{2g}^1 peak leading the overestimation of $\Delta\omega$.[183]

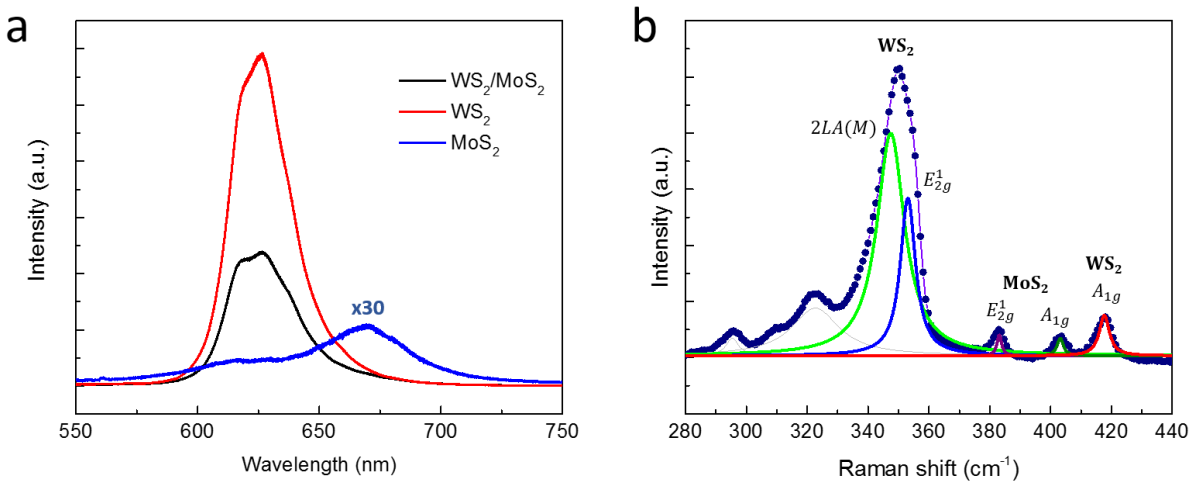


Figure 6.2 Raman and PL characterization of CVD-grown TMDs. (a) PL spectra of monolayer WS_2, MoS_2, and WS_2/MoS_2 bilayer stack. (b) Raman spectra of a WS_2/MoS_2 vertical stack under 532 nm laser. A multi-Lorentzian curve fitting of the spectra shows signature vibrational modes of WS_2 crystals depicted as labelled fitted curves of $2LA$ (green), E^1_{2g} (blue) and A_{1g}(red) peaks and those of MoS_2 crystals including E^1_{2g}(violet) and A_{1g}(dark green) peaks.

6.2.3 Opto-electrical Characterizations

The output characteristics of the 5 sets of TMD photodetectors under different light irradiation powers (λ=532 nm) are displayed in **Figure 6.3**a-e. All of the photodetectors except for the WS_2/MoS_2 heterobilayer device exhibited a non-linear *I-V* curve, indicating a non-ideal contact between the graphene electrodes and the TMD crystals. Under illumination, the WS_2/MoS_2 bilayer device has a near Ohmic response and even shows signs of reaching the saturation region with increasing V_{ds}. The dark currents for each type of device are recorded in Figure 6.3f, under an applied bias of V_{ds}=5 V. The WS_2/MoS_2 bilayer devices have the lowest channel resistance with a dark current of ~10^{-6} A. This is followed by MoS_2 bilayer and WS_2 bilayer devices with dark current ranging from 10^{-9} to 10^{-7} A. The dark current of MoS_2 monolayer (~10^{-8} A) is observed to be slightly larger than WS_2 (10^{-9} A), indicating a lower resistivity of MoS_2 channels compared with WS_2.

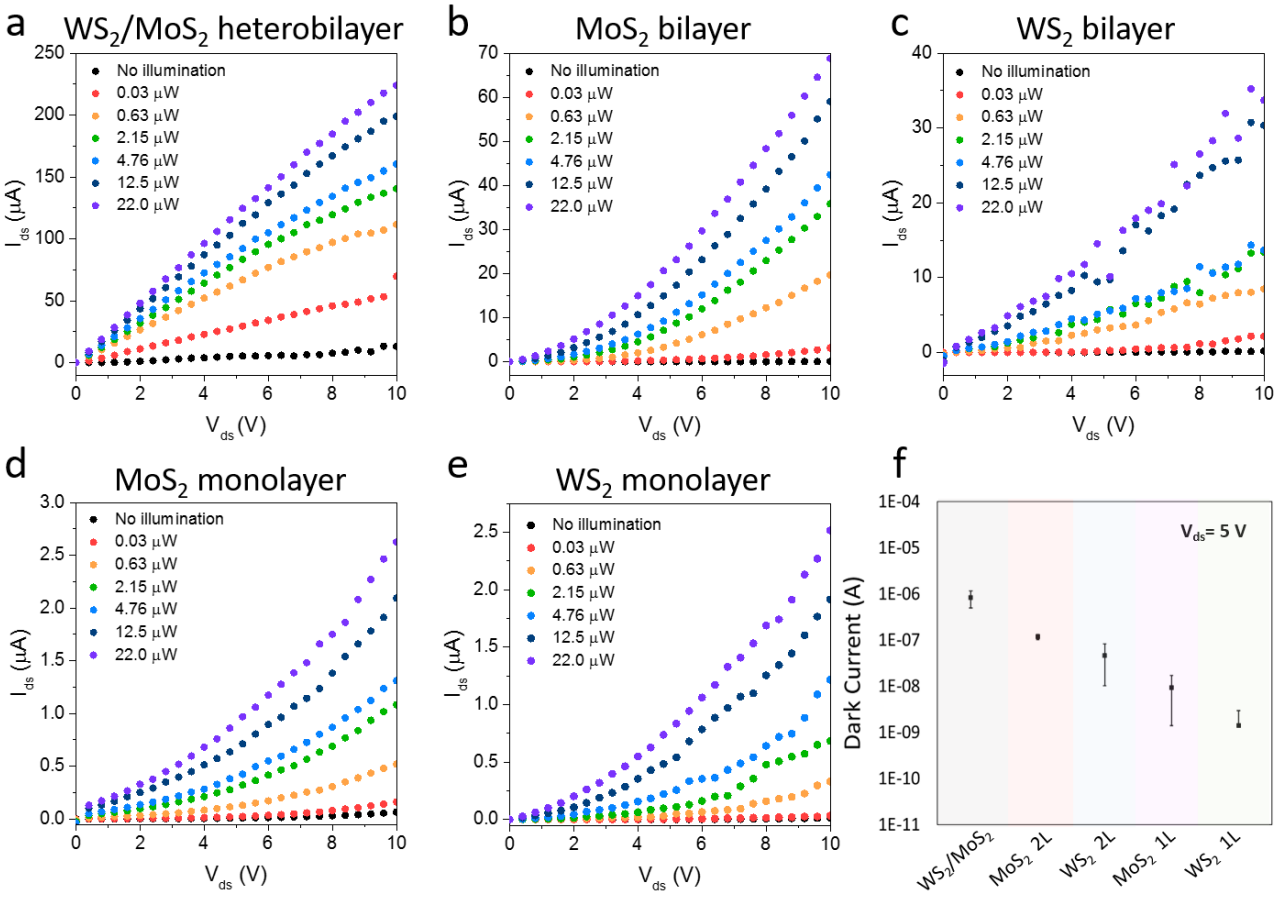


Figure 6.3 Output characteristics of the 5 types of TMD photodetectors. I_{ds}-V_{ds} measurements under different light irradiation powers for (a) WS_2/MoS_2 heterobilayer device (b) MoS_2 bilayer device (c) WS_2 bilayer device (d) MoS_2 monolayer device, and (e) WS_2 monolayer device. (f) The distribution of dark current under V_{ds}=5 V of the 5 types of photodetectors.

The photocurrent generation of a photoconductive material strongly depends on the resistance under differing irradiation intensity. For a lateral photoconductor with a MSM configuration, and especially photodetectors based on 2D crystals, much of the devices' resistance comes from the non-ideal contact, or the Schottky contact, formed at the metal-semiconductor interface. The Schottky barrier inhibits the flow of electrons (holes), allowing limited charge injection through tunneling and thermionic emissions, giving rise to the non-linearity of the output characteristics of the devices. To estimate the effective Schottky barrier height at the graphene-TMD junctions, back-to-back Schottky diode model is introduced as a simple representation of our MSM photodetectors, and the *I*-*V* measurements

under different light intensity are fitted using the modified thermionic emission equation as discussed in Chapter 5.

Figure 6.4a shows the obtained effective Schottky barrier height Φ_{SB_eff} *versus* the incident light intensity of the different devices. The obtained Φ_{SB_eff} of all 5 devices show negative correlation with light power, among which WS_2/MoS_2 bilayer devices exhibited the smallest Φ_{SB_eff} value, reaching below 100 meV under the largest irradiation power. It is also worth noting that the obtained Φ_{SB_eff} corresponds closely with magnitude of current under dark conditions and different light intensity as shown in Figure 6.3, reflecting on the strong influence that graphene-TMD contacts have on the total resistance of the device. The photocurrent $I_{\text{photo}} = I_{\text{light}} - I_{\text{dark}}$, was extracted from the output characteristics of the devices under dark and illuminated conditions. Shown in Figure 6.4b, the photocurrent generated from all devices increased with larger applied bias. Under the same irradiation power, the WS_2/MoS_2 bilayer device generated the largest photocurrent compared with TMD bilayer devices, which were then followed by the TMD monolayer devices.

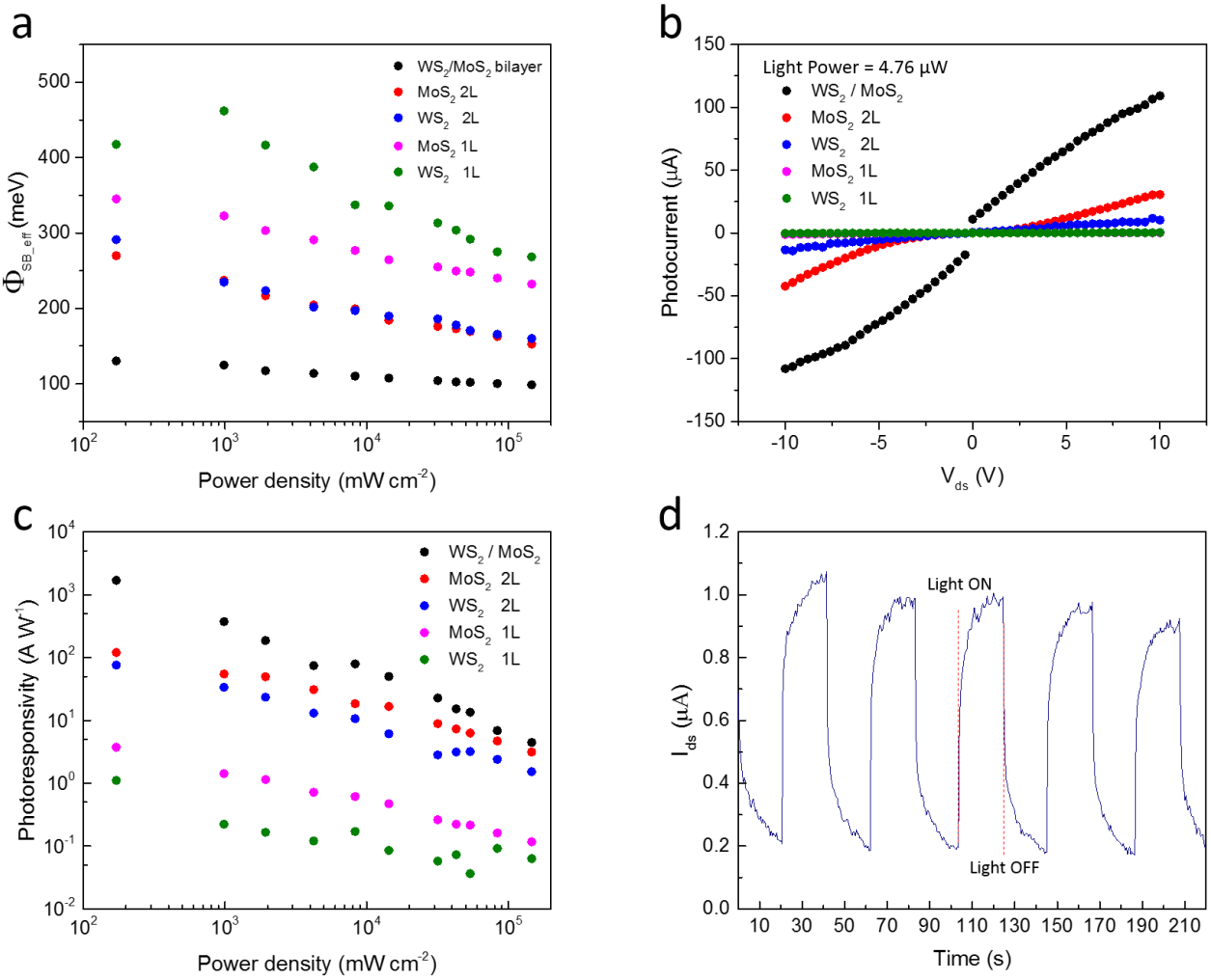


Figure 6.4 Opto-electronics behavior of graphene-TMD-graphene photodetectors. (a) Calculated effective Schottky barrier of graphene-TMD interface *versus* irradiation power density (b) Photocurrent *versus* V_{ds} under illumination power of 127 μW. (c) Photoresponsivity *versus* irradiation power. (d) Transient photocurrent characteristics of WS_2/MoS_2 heterobilayer device under V_{ds} = +1 V, V_G = -30 V under power density of 1.7×10^2 mW/cm^2.

6.2.4 Figures of Merit Comparison

Using the equations (**Eq. 5-1** – **Eq. 5-3**) described in Chapter 5, we calculate the photoresponsivity (R), photoconductive gain (G) and specific detectivity (D^*) of the 5 types of photodetectors. Figure 6.4c shows the power dependence of R under 11 different light intensities for all five types of devices. The negative correlation of R and light intensity reflects the sub-linear photocurrent generation with increasing irradiation power. This is due to the saturation of trap states under high power illumination and also the shortening of

carrier lifetimes due to increased self-collision and quenching as more charge carriers populate the conduction band.[250] The TMD bilayers also show larger photoresponse than their monolayer counterparts, which could be due to the following reasons: increased absorbance due to an extra layer, lower channel resistivity, increased mobility due to encapsulation of the bottom layer, and introduction of new trap sites following an additional layer transfer. Surprisingly, WS_2/MoS_2 heterobilayer devices are found to exhibit a significantly large photoresponsivity as high as 2340 A W^{-1}, which is over 10 times larger than TMD homobilayer devices, and 10^3 factor improvement compared with the TMD monolayer devices (**Table 6.1**).

Considering the absorbed photons of the devices, we can further derive the internal photoconductive gain (G_{int}) based on **Eq. 5-2** using $G_{\text{int}} = {}^{G_{\text{ext}}}/_{QE}$, where *QE* stands for quantum efficiency, and synonymous with light absorbance in cases of photoconductors. An absorbance of 8% and transmittance of 92% for both MoS_2 and WS_2 monolayers are assumed under λ=532 nm light source for the calculation of G_{int}.[124] **Table 6.1** records the device performance statistics of the 5 types of photoconductors.

The top performing device were the WS_2/MoS_2 bilayer photodetectors, which exhibited the highest photoresponsivity of up to 2340 A/W, internal photoconductive gain of over 3.7×10^4, and a shot-noise-limited specific detectivity of 4×10^{11} Jones (Jones = cm $Hz^{1/2}$ W^{-1}). To the best of our knowledge, WS_2/MoS_2 heterobilayer photodetector's responsivity of this study outperforms most reported values of lateral photodetectors based on monolayer or few layer TMDs (0.1~10^3 A/W), [127,129,140,234,251] and are comparable with the optimally reported values of sensitized or encapsulated TMD photodetectors.[131,144]

The transient photocurrent response of WS_2/MoS_2 heterobilayer device is shown in Figure 6.4d, exhibiting an ON/OFF ratio ($I_{\text{photo}}/I_{\text{dark}}$) of ~5 under illuminated and dark

conditions. The large decay time, which is more than a few seconds, is strong indication of the existence of trapped charges across the heterostructured semiconducting channel.

Table 6.1 TMD Photoconductors and their figures of merits. Device performance statistics (number of samples measured, highest recorded photoresponsivity, average photoresponsivity, external gain and shot-noise-limited specific detectivity with calculated standard deviation) under ambient conditions (V_{bias}= 10 V, V_G= 0 V, λ=532 nm, P_{light} = 1.7×10^2 mW cm^{-2}).

Device structure	No. of samples	R_{max} [A W^{-1}]	R [A W^{-1}]	G_{ext}	D^* [Jones]
WS_2/MoS_2 bilayer	16	2340	1173 ± 462	2737 ± 1078	(2.1 ± 0.3)×10^{11}
MoS_2 (2L)	5	120	83 ± 35	194 ± 82	(2.4 ± 0.7)×10^{11}
WS_2 (2L)	10	93	64 ± 36	150 ± 84	(1.2 ± 0.5)×10^{11}
MoS_2 (1L)	8	3.7	2.2 ± 1.1	5.1 ± 2.6	(6.5 ± 1.9)×10^{10}
WS_2 (1L)	6	1.1	0.8 ± 0.2	1.9 ± 0.5	(1.1 ± 0.2)×10^{10}

6.2.5 Gate dependence study

Applying gate potential is the most common and effective way to control the behaviour of semiconductor devices. In our previous studies,[226,252] it was observed that applied back gate is not only tunes the Fermi level of the semiconducting TMD, but can also tune the work function of graphene. As a result, modification the Schottky barrier height at the graphene-TMD interface can be achieved.

The influence of applied gate voltage on our graphene-contacted WS_2/MoS_2 heterobilayer device is further investigated. Gate sweep is performed on the heterobilayer sample to probe its performance as a field-effect transistor. The transfer curve (**Figure 6.5**a) shows a typical n-type behavior of the WS_2/MoS_2 heterobilayer. The estimated mobility of the hybrid device can be extracted using $\mu = \frac{dI_{\mathrm{ds}}}{dV_{\mathrm{G}}} \cdot \frac{L}{w} \cdot \frac{1}{V_{\mathrm{sd}}} \cdot \frac{1}{C_{\mathrm{ox}}}$, where L and w are the channel's length and width respectively, and C_{ox} is the gate capacitance of the SiO_2 substrate.

Using this equation, an effective mobility of μ = 3.16 cm^2 V s^{-1} is obtained. Alongside the I_{ds}-V_G curve on linear scale (blue curve) is the same data plotted against a logarithmic y-scale (green curve), which shows an I_{on}/I_{off} ratio as high as 10^5 in the n-type region. The *SS* is calculated from the slope of subthreshold region (yellow dotted line) to be 7.6 V/decade, which is in a range consistent with previous reports based on CVD-grown TMDs.[142,239] This value of *SS* is quite far from the theoretical limit of 60 mV/decade, indicating non-ideality of the contacts and the existence of trap states.

Figure 6.5b shows that the device photoresponsivity under fixed illumination can be further improved by applying positive gate potential. The photoresponse of our WS_2/MoS_2 heterostructure device under V_{ds}=5 V increases with larger applied positive gate voltage and more than doubles its original value under a gate potential at V_G=+70 V. Our results once again show that Schottky barriers formed between the graphene-TMD are sensitive to photo-illumination and gate potential as is evident in our previous studies,[226,252] and further demonstrates gate modification of Schottky barrier height for optimized device performance of graphene-TMD-graphene photoconductors.

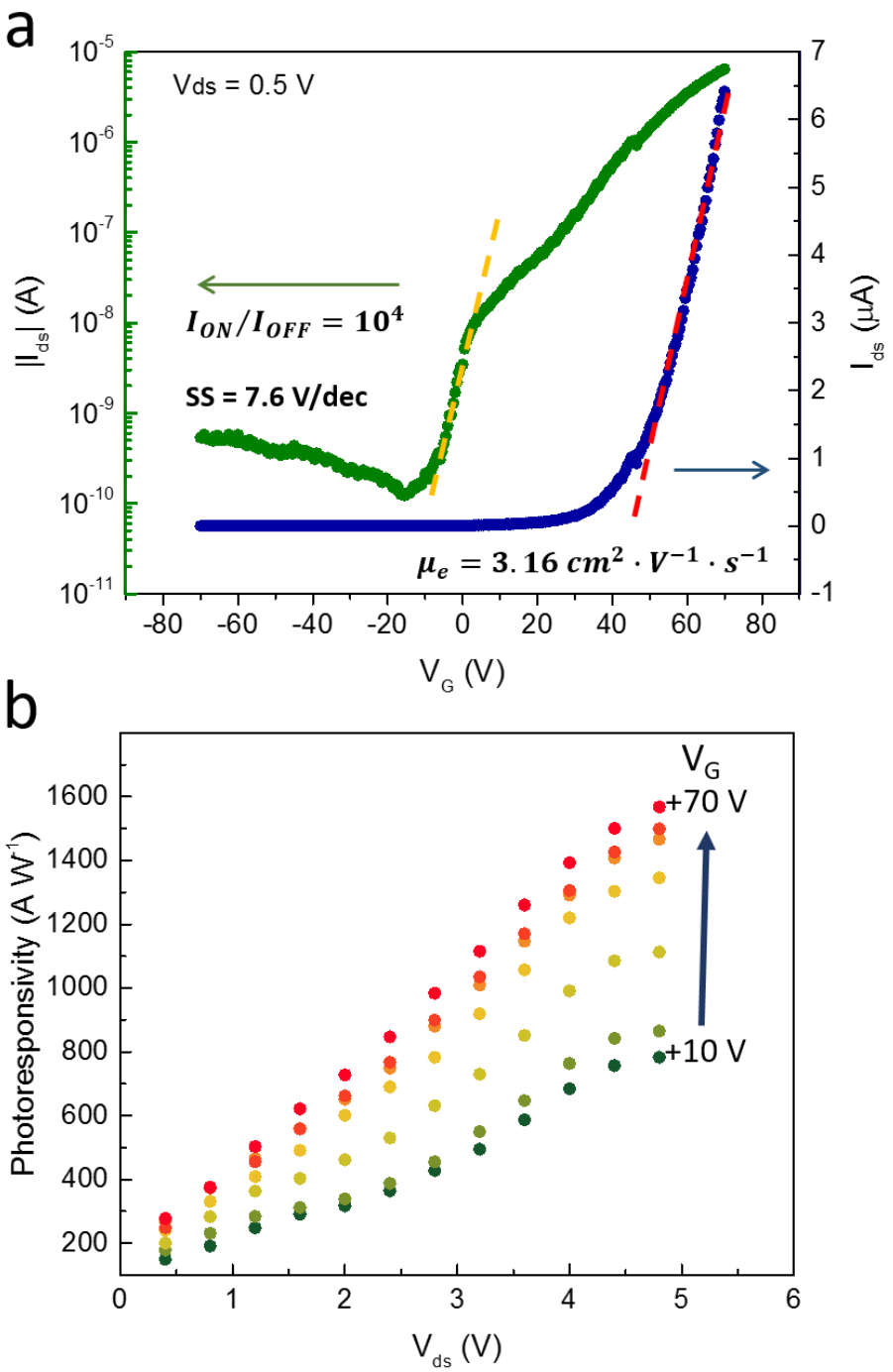


Figure 6.5 Gate dependence characteristics of a WS_2/MoS_2 bilayer device. (a) I_{ds}-V_G plot of hybrid device on linear scale (blue) and logarithmic scale (green) indicating the n-type characteristic of WS_2/MoS_2 heterostructure. An I_{on}/I_{off} ratio of 10^4 and subthreshold swing (SS) of 7.6 V/decade are obtained from the logarithmic plot, and electron mobility extracted from the linear region of the transfer curve shows to be 3.16 $cm^2/(V \cdot s)$. (b) Photoresponsivity *versus* V_{ds} with increasing applied back gate potential under illumination power of 1.7×10^2 mW/cm^2.

6.2.6 Cause of Large Gain in Hybrid graphene-WS_2/MoS_2-graphene Photodetectors

To understand the improved performance in a WS_2/MoS_2 heterobilayer photodetector, we turn to the dynamics of interlayer coupling in a vertically stacked WS_2 and MoS_2 heterostructure. **Figure 6.6**a shows the schematic of a type-II band alignment formed at the WS_2/MoS_2 heterobilayer.[153,253] Upon illumination, photo-excited electrons and holes separate across the two different layers, where the electrons reside at the conduction band of MoS_2 and holes in the WS_2 at the interface.[153] The n-type characteristics of the WS_2/MoS_2 heterobilayer device suggests that MoS_2 may act as the main conductive channel in which the majority carrier (electron) transits within a closed circuit.

Figure 6.6b shows the band diagram of the graphene-WS_2/MoS_2-graphene device under applied gate. The Dirac cones of graphene's band structure result in a work function that is susceptible to gate potential. This implies a gate tunable Schottky barrier, which in this study can be roughly estimated by the band offset at the metal-semiconductor interface expressed as $\Phi_{SB} = \Phi_{Gr} - \chi_{TMD}$. A positive gate will lower the work function of graphene electrodes, and lead to a lowering in Φ_{SB}. Figure 6.6c shows the band diagram of the device under dark and illuminated conditions. Upon illumination, the recombination of electron-hole pairs is suppressed due to the interlayer charge transfer between WS_2 and MoS_2. Under an applied bias $+V_{ds}$, electrons and holes drift towards opposite sides. The electrons are collected at the drain electrode which contributes to the photocurrent, while with the existence of trap states, holes start to accumulate at the source region. The accumulation of holes at the region acts as a positive gate on the source graphene electrode, in effect raising the Fermi level of the graphene electrode and lowering the Φ_{SB}. This lowering of barrier due to photogating effect will facilitate the re-injection of electrons into the TMD channel. Photoconductors rely on such a mechanism to enable photoconductive gain, where minority

carriers are trapped so that majority carriers can recirculate along the channel for each absorbed photon. The interlayer coupling between WS_2 and MoS_2 may therefore facilitate such a long-lived trap state necessary for large photoconductive gain.[244,248] This helps explain the significantly large photoconductive gain and responsivity that is observed in our graphene contacted WS_2/MoS_2 heterobilayer photoconductors.

Unlike vertical graphene-TMD-graphene photodiodes, which are limited to photocurrent generation based on photovoltaic mechanisms or tunneling currents,[134,163,164] our lateral photodetectors rely on photogating mechanism and can thus reach an external quantum efficiency over unity with significantly high photoresponsivity. This photogating effect is attributed to the suppressed recombination of electron-hole pairs at separated layers of the WS_2/MoS_2 heterostructure, resulting in free electrons that acts as carriers and holes that act as positive gate. Moreover, the device architecture of a TMD heterobilayer sandwiching graphene electrodes allows a direct contact between metal-semiconductor and enables a more efficient gating effect to take place during irradiation.

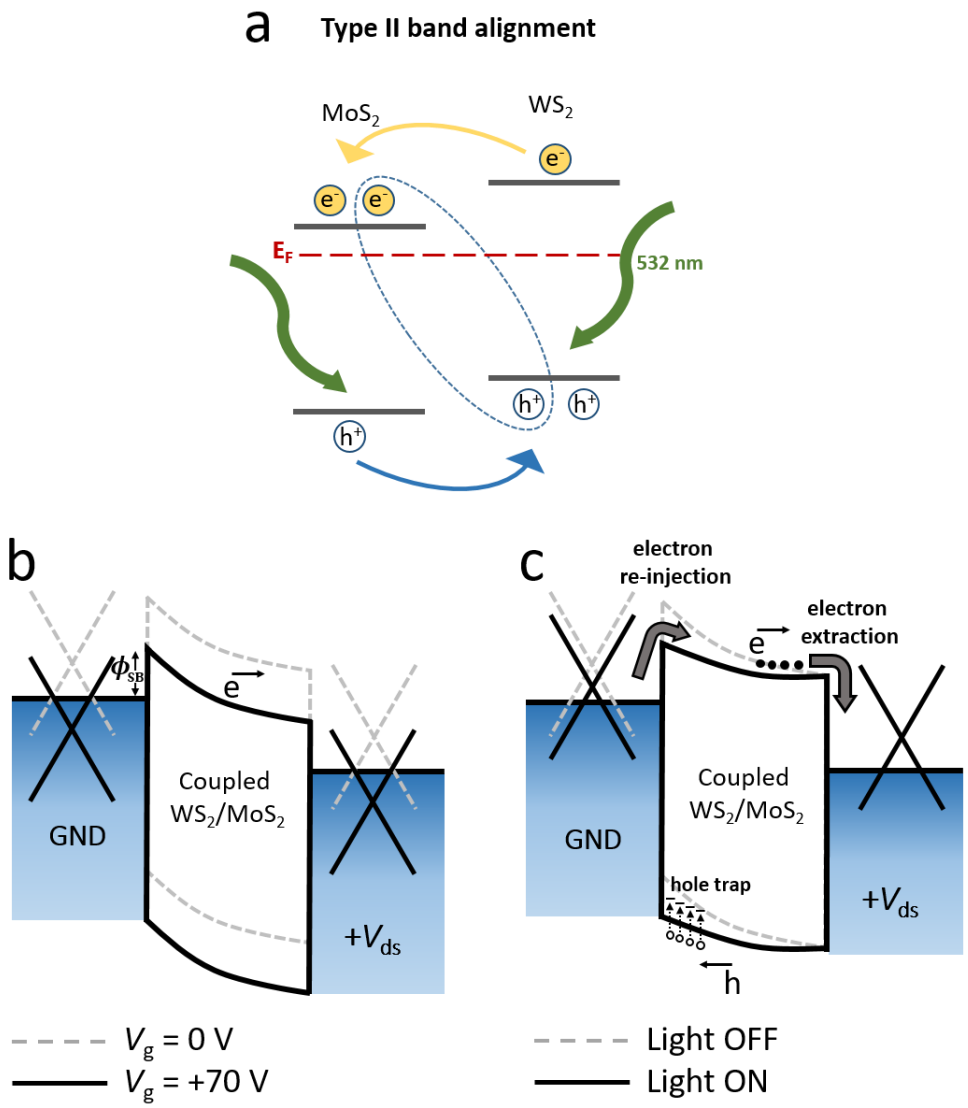


Figure 6.6 Dynamics of interlayer charge transfer and carrier transportation of graphene-WS_2/MoS_2-graphene photodetector. (a) Band schematic of a vertically stacked WS_2/MoS_2 heterostructure. Due to the type-II band alignment, photo-excited electrons and holes tend to accumulate on separate layers. The carrier separation occurs within picoseconds, forming layer-separated excitons with electrons and holes residing at MoS_2 and WS_2 respectively. (b) Band schematic of device while applying positive back-gate potential. Graphene's work function Φ_{Gr} can be tuned by positive gate, leading to lowering of the Schottky barrier at the graphene-TMD interface. (c) Band schematic of device under light irradiation. Upon illumination, formed layer-separated excitons across WS_2 and MoS_2 suppresses electron-hole recombination and further dissociates to free carriers. Under external electric field given by $+V_{ds}$, electrons drift toward the drain electrode which is extracted as photocurrent, while holes drift towards graphene source electrode connected to ground (GND). Trapped states within the TMD bilayer facilitates an accumulation of holes near the graphene-TMD interface at the source region, creating a positive photogating effect on the graphene electrode and lowers the Schottky barrier at the source. This allows increase in thermionic emission over the graphene-TMD Schottky barrier leading to increased injection of electrons from source electrode to the WS_2/MoS_2 channel, and thus facilitates the circulation of electrons within the photodetector.

6.3 Conclusion

In summary, high-performing lateral MSM photodetectors were demonstrated based on graphene-contacted WS_2/MoS_2 heterostacks. Utilizing the efficient interlayer charge transfer between WS_2 and MoS_2, photoresponsivity of up to 2340 A/W and an internal photoconductive gain of over 3.7×10^4 are achieved, improving photoresponsivity by over an order of magnitude compared with the respective TMDs monolayers and bilayers. All the crystals used to fabricate the lateral photodetectors have been synthesized using CVD, eliminating mechanical exfoliation and therefore allowing production of device arrays on a large scale, providing rigorous statistics on device performances to support our conclusions. This demonstration of a hybrid TMD photodetector points to a promising route to optimize photodetectors' performance by controlling interlayer charge transfer between vdW crystals.

6.4 Contribution Statement

Graphene, MoS_2, and WS_2 crystals were provided by Miss Qu Chen, Miss Wenshuo Xu and Mr. Yuewen Sheng respectively. Dr. Chit Siong Lau and Dr. Ye Fan contributed to the ideation and experimental design of this study. Mr. Martin Tweedie established the procedure for the slide transfer of 2D crystals. SEM image was taken by Mr. Xiaochen Wang.

Chapter 7 Conclusion and Future Outlook

In this concluding chapter, the findings of this thesis and their implications are briefly summarized. The prospects of future research, possible opportunities and challenges are then addressed.

7.1 Thesis Summary

In Chapter 4, the fabrication of p+/p isotype junctions was demonstrated by vertically stacking WS_2 domains on graphene FET arrays. A strong regional doping of graphene was realized via charge transfer from the stacked WS_2 domains, which gives rise to two Dirac points in the transistors' field effect measurements. This observed doping of graphene, unlike other conventional doping methods that involve electrostatic modulation or chemical intercalation, relies merely on charge transfer at the interface of the two materials. Moreover, the charge transfer between WS_2 and graphene can be further modulated with light irradiation. This finding offers an alternative method to selectively tune certain regions of graphene channel's Fermi level to form lateral p-n junctions in a controllable manner.

In Chapter 5, all-2D photodetector arrays with an extreme thinness (2 nm) were demonstrated, with graphene used as electrodes and WS_2 monolayers and bilayers as active light-absorbing components. Graphene was found to behave differently compared with bulk metals owing to its finite density of states. The Schottky barrier that was formed between graphene-WS_2 are tunable by both electrostatic gating and input light intensity. This resulted in a high photoresponsivity reaching 2 A W^{-1} under high irradiation power. This work substantiates the validity of using graphene as the electrodes in 2D FETs, and provides a promising solution to the contact engineering challenges of TMD-based optoelectronic devices.

Finally in Chapter 6, a hierarchical device consisting graphene-contacted lateral photoconductors based on vertical WS_2/MoS_2 heterostructure was demonstrated. The design of such a device was based on the gathered insights on the interlayer charge transfer between 2D crystals, and the understanding of the underlying mechanisms of photocurrent generation in photoconductors. Utilizing the interlayer excitonic formation and long photocarrier lifetimes at the WS_2/MoS_2 heterostructure, a high internal photoconductive gain of 3.7×10^4 and photoresponsivity of over 2000 A W^{-1} were achieved. The hybrid devices based on the proposed WS_2/MoS_2 heterobilayer outperformed other lateral devices based on TMD homobilayers and monolayer, by one to three order(s) of magnitudes of improvement in photoresponsivity. This work is among the first attempts to utilize the unique features brought by the type-II band alignment of TMD heterointerfaces for enhanced light sensing applications, and provides a prototype for future high performance 2D photodetectors.

In summary, the achievements of this work can be categorized into three parts: 1) investigated the surface charge transfer between graphene and TMDs, 2) evaluated the validity of graphene electrodes in 2D photoconductors, and 3) proposed and realized a hierarchical device based on 2D crystals for enhanced photoresponsivity.

7.2 Future Outlook

The continued miniaturization of electronics is an inevitable trend as we enter an ever-more-connected world, in which abundant data could be collected and processed. As industry continues to reap the benefits of scaling, new materials and device fabrication processes will be critical for the final realization of nanoscale electronics. 2D materials and their hybrid systems, with their unique electronic/optoelectronic properties as described in previous chapters, are believed to remain relevant to both fundamental research and industrial innovation in the years to come.[254–257]

Further works will be expected in the fabrication of nanoscale devices on unconventional substrates beyond Si chip. For example, the wet transfer method employed in this thesis, which is commonly used for transferring CVD-grown 2D crystals, has been gaining momentum in the fabrication of nano- and micron-scale devices on flexible/stretchable membranes, textiles and fibers.[171,258,259] The high conformability of 2D materials combined with such transfer method will ultimately enable their implementation in wearable and implantable technologies.

However, challenges of realizing real-life 2D electronic devices still remain. Although CVD-grown 2D crystals can be produced on a large scale, they often carry defects and unintended contaminations introduced by both synthesis and device fabrication processes.[260,261] Additionally, both the degradation and their high sensitivity to external environment of 2D crystals may unfavorably impact the performance and operating lifetimes of their devices.[118,262,263] In this regard, controllable synthesis of high quality 2D crystals, optimized cleaning/annealing process, and the passivation/encapsulation of 2D devices will require further study. In conclusion, simultaneous improvements in both materials synthesis and device designs that ensure high reproducibility and reliability will be key to the realization of future generations of electronic devices based on 2D materials.

References

(1) Neto, A. C.; Castro Neto, A. H.; Peres, N. M. R.; Novoselov, K. S.; Geim, A. K.; Guinea, F. The Electronic Properties of Graphene. *Rev. Mod. Phys.* **2009**, *81*, 109–162.

(2) Novoselov, K. S.; Geim, A. K.; Morozov, S. V.; Jiang, D.; Zhang, Y.; Dubonos, S. V.; Grigorieva, I. V.; Firsov, A. A. Electric Field Effect in Atomically Thin Carbon Films. *Science* **2004**, *306*, 666–669.

(3) Geim, A. K.; Novoselov, K. S. The Rise of Graphene. *Nat. Mater.* **2007**, *6*, 183–191.

(4) Lee, C.; Wei, X.; Kysar, J. W.; Hone, J. Measurement of the Elastic Properties and Intrinsic Strength of Monolayer Graphene. *Science* **2008**, *321*, 385–388.

(5) Novoselov, K. S.; Geim, A. K.; Morozov, S. V; Jiang, D.; Katsnelson, M. I.; Grigorieva, I. V.; Dubonos, S. V.; Firsov, A. A. Two-Dimensional Gas of Massless Dirac Fermions in Graphene. *Nature* **2005**, *438*, 197–200.

(6) Du, X.; Skachko, I.; Barker, A.; Andrei, E. Y. Approaching Ballistic Transport in Suspended Graphene. *Nat. Nanotechnol.* **2008**, *3*, 491–495.

(7) Mayorov, A. S.; Gorbachev, R. V; Morozov, S. V; Britnell, L.; Jalil, R.; Ponomarenko, L. A.; Blake, P.; Novoselov, K. S.; Watanabe, K.; Taniguchi, T.; *et al.* Micrometer-Scale Ballistic Transport in Encapsulated Graphene at Room Temperature. *Nano Lett.* **2011**, *11*, 2396–2399.

(8) Neto, A. H. C.; Novoselov, K. New Directions in Science and Technology: Two-Dimensional Crystals. *Reports Prog. Phys.* **2011**, *74*, 82501.

(9) Li, X.; Wang, X.; Zhang, L.; Lee, S.; Dai, H. Chemically Derived, Ultrasmooth Graphene Nanoribbon Semiconductors. *Science* **2008**, *319*, 1229–1232.

(10) Han, M.; Özyilmaz, B.; Zhang, Y.; Kim, P. Energy Band-Gap Engineering of Graphene Nanoribbons. *Phys. Rev. Lett.* **2007**, *98*, 206805.

(11) Ramakrishna Matte, H. S. S.; Gomathi, A.; Manna, A. K.; Late, D. J.; Datta, R.; Pati, S. K.; Rao, C. N. R. MoS2 and WS2 Analogues of Graphene. *Angew. Chemie - Int. Ed.* **2010**, *49*, 4059–4062.

(12) Mak, K. F.; Lee, C.; Hone, J.; Shan, J.; Heinz, T. F. Atomically Thin MoS2: A New Direct-Gap Semiconductor. *Phys. Rev. Lett.* **2010**, *105*, 136805.

(13) Paciĺ, D.; Meyer, J. C.; Girit, Ç.; Zettl, A. The Two-Dimensional Phase of Boron Nitride: Few-Atomic-Layer Sheets and Suspended Membranes. *Appl. Phys. Lett.* **2008**, *92*, 1–4.

(14) Li, L.; Yu, Y.; Ye, G. J.; Ge, Q.; Ou, X.; Wu, H.; Feng, D.; Chen, X. H.; Zhang, Y. Black Phosphorus Field-Effect Transistors. *Nat. Nanotechnol.* **2014**, *9*, 372–377.

(15) Geim, A. K.; Grigorieva, I. V. Van Der Waals Heterostructures. *Nature* **2013**, *499*, 419–425.

(16) Liu, Y.; Weiss, N. O.; Duan, X.; Cheng, H.; Huang, Y.; Duan, X. Van Der Waals

Heterostructures and Devices. *Nat. Rev. Mater.* **2016**, *1*, 16042.

(17) Novoselov, K. S.; Mishchenko, A.; Carvalho, A.; Castro Neto, A. H. 2D Materials and van Der Waals Heterostructures. *Science* **2016**, *353*.

(18) Wang, Q. H.; Kalantar-Zadeh, K.; Kis, A.; Coleman, J. N.; Strano, M. S. Electronics and Optoelectronics of Two-Dimensional Transition Metal Dichalcogenides. *Nat. Nanotechnol.* **2012**, *7*, 699–712.

(19) Duan, X.; Wang, C.; Pan, A.; Yu, R.; Duan, X. Two-Dimensional Transition Metal Dichalcogenides as Atomically Thin Semiconductors: Opportunities and Challenges. *Chem. Soc. Rev.* **2015**, *44*, 8859–8876.

(20) Splendiani, A.; Sun, L.; Zhang, Y.; Li, T.; Kim, J.; Chim, C.-Y.; Galli, G.; Wang, F. Emerging Photoluminescence in Monolayer MoS2. *Nano Lett.* **2010**, *10*, 1271–1275.

(21) Moore, G. E. Cramming More Components onto Integrated Circuits. *Proc. IEEE* **1998**, *86*, 82–85.

(22) Waldrop, M. M. The Chips Are down for Moore's Law. *Nature* **2016**, *530*, 144–147.

(23) Kuhn, K. J.; Avci, U.; Cappellani, A.; Giles, M. D.; Haverty, M.; Kim, S.; Kotlyar, R.; Manipatruni, S.; Nikonov, D.; Pawashe, C.; *et al.* The Ultimate CMOS Device and beyond. In *2012 International Electron Devices Meeting*; 2012; p. 8.1.1-8.1.4.

(24) Schwierz, F. Graphene Transistors. *Nat. Nanotechnol.* **2010**, *5*, 487–496.

(25) Sze, S. M.; Ng, K. K. *Physics of Semiconductor Devices*; John Wiley & Sons, 2006; Vol. 3.

(26) Jim, J. A.; Palma, A. A Simple Subthreshold Swing Model for Short Channel MOSFETs. **2001**, *45*, 391–397.

(27) Lee, C.; Yan, H.; Brus, L. E.; Heinz, T. F.; Hone, J.; Ryu, S. Anomalous Lattice Vibrations of Single- and Few-Layer MoS2. *ACS Nano* **2010**, *4*, 2695–2700.

(28) Bertolazzi, S.; Brivio, J.; Kis, A. Stretching and Breaking of Ultrathin MoS2. *ACS Nano* **2011**, *5*, 9703–9709.

(29) Radisavljevic, B.; Whitwick, M. B.; Kis, A. Integrated Circuits and Logic Operations Based on Single-Layer MoS2. *ACS Nano* **2011**, *5*, 9934–9938.

(30) Coleman, J. N.; Lotya, M.; O'Neill, A.; Bergin, S. D.; King, P. J.; Khan, U.; Young, K.; Gaucher, A.; De, S.; Smith, R. J.; *et al.* Two-Dimensional Nanosheets Produced by Liquid Exfoliation of Layered Materials. *Science* **2011**, *331*, 568–571.

(31) Hernandez, Y.; Nicolosi, V.; Lotya, M.; Blighe, F. M.; Sun, Z.; De, S.; McGovern, I. T.; Holland, B.; Byrne, M.; Gun'Ko, Y. K.; *et al.* High-Yield Production of Graphene by Liquid-Phase Exfoliation of Graphite. *Nat. Nanotechnol.* **2008**, *3*, 563–568.

(32) Zhi, C.; Bando, Y.; Tang, C.; Kuwahara, H.; Goldberg, D. Large Scale Fabrication of Boron Nitride Nanosheets and Their Utilization in Polymeric Composites with Improved Thermal and Mechanical Properties. *Adv. Mater.* **2009**, *21*, 2889–2893.

(33) Benavente, E.; Santa Ana, M. A.; Mendizabal, F.; Gonzalez, G. Intercalation Chemistry of Molybdenum Disulfide. *Coord. Chem. Rev.* **2002**, *224*, 87–109.

(34) Eda, G.; Yamaguchi, H.; Voiry, D.; Fujita, T.; Chen, M.; Chhowalla, M.

Photoluminescence from Chemically Exfoliated MoS2. *Nano Lett.* **2011**, *11*, 5111–5116.

(35) Joensen, P.; Frindt, R. F.; Morrison, S. R. Single-Layer MoS2. *Mater. Res. Bull.* **1986**, *21*, 457–461.

(36) Zeng, Z.; Yin, Z.; Huang, X.; Li, H.; He, Q.; Lu, G.; Boey, F.; Zhang, H. Single-Layer Semiconducting Nanosheets: High-Yield Preparation and Device Fabrication. *Angew. Chemie Int. Ed.* **2011**, *50*, 11093–11097.

(37) Shi, Y.; Li, H.; Li, L.-J. Recent Advances in Controlled Synthesis of Two-Dimensional Transition Metal Dichalcogenides via Vapour Deposition Techniques. *Chem. Soc. Rev.* **2015**, *44*, 2744–2756.

(38) Hass, J.; de Heer, W. A.; Conrad, E. H. The Growth and Morphology of Epitaxial Multilayer Graphene. *J. Phys. Condens. Matter* **2008**, *20*, 323202.

(39) Ma, T.; Ren, W.; Liu, Z.; Huang, L.; Ma, L. P.; Ma, X.; Zhang, Z.; Peng, L. M.; Cheng, H. M. Repeated Growth-Etching-Regrowth for Large-Area Defect-Free Single-Crystal Graphene by Chemical Vapor Deposition. *ACS Nano* **2014**, *8*, 12806–12813.

(40) Addou, R.; Dahal, A.; Sutter, P.; Batzill, M. Monolayer Graphene Growth on Ni(111) by Low Temperature Chemical Vapor Deposition. *Appl. Phys. Lett.* **2012**, *100*, 21601.

(41) Liu, N.; Fu, L.; Dai, B.; Yan, K.; Liu, X.; Zhao, R.; Zhang, Y.; Liu, Z. Universal Segregation Growth Approach to Wafer-Size Graphene from Non-Noble Metals. *Nano Lett.* **2011**, *11*, 297–303.

(42) Yu, Q.; Lian, J.; Siriponglert, S.; Li, H.; Chen, Y. P.; Pei, S. S. Graphene Segregated on Ni Surfaces and Transferred to Insulators. *Appl. Phys. Lett.* **2008**, *93*, 91–94.

(43) Kwon, S. Y.; Ciobanu, C. V.; Petrova, V.; Shenoy, V. B.; Bareño, J.; Gambin, V.; Petrov, I.; Kodambaka, S. Growth of Semiconducting Graphene on Palladium. *Nano Lett.* **2009**, *9*, 3985–3990.

(44) Bae, S.; Kim, H.; Lee, Y.; Xu, X.; Park, J.-S.; Zheng, Y.; Balakrishnan, J.; Lei, T.; Ri Kim, H.; Song, Y. Il; *et al.* Roll-to-Roll Production of 30-Inch Graphene Films for Transparent Electrodes. *Nat. Nanotechnol.* **2010**, *5*, 574–578.

(45) Li, X.; Cai, W.; An, J.; Kim, S.; Nah, J.; Yang, D.; Piner, R.; Velamakanni, A.; Jung, I.; Tutuc, E.; *et al.* Large-Area Synthesis of High-Quality and Uniform Graphene Films on Copper Foils. *Science* **2009**, *324*, 1312–1314.

(46) Zhao, P.; Kumamoto, A.; Kim, S.; Chen, X.; Hou, B.; Chiashi, S.; Einarsson, E.; Ikuhara, Y.; Maruyama, S. Self-Limiting Chemical Vapor Deposition Growth of Monolayer Graphene from Ethanol. *J. Phys. Chem. C* **2013**, *117*, 10755–10763.

(47) Fu, Q.; Xiang, B. Monolayer Transition Metal Disulfide: Synthesis, Characterization and Applications. *Prog. Nat. Sci. Mater. Int.* **2016**, *26*, 221–231.

(48) Lee, Y.-H.; Zhang, X.-Q.; Zhang, W.; Chang, M.-T.; Lin, C.-T.; Chang, K.-D.; Yu, Y.-C.; Wang, J. T.-W.; Chang, C.-S.; Li, L.-J.; *et al.* Synthesis of Large-Area MoS_2 Atomic Layers with Chemical Vapor Deposition. *Adv. Mater.* **2012**, *24*, 2320–2325.

(49) Lee, Y.; Yu, L.; Wang, H.; Shi, Y.; Huang, J.; Chang, T.; Chang, C.; Dresselhaus, M.

S.; Palacios, T.; Li, L.; *et al.* Synthesis and Transfer of Single Layer Transition Metal Disulfides on Diverse Surfaces. *Nano Lett.* **2013**, *13*, 1852–1857.

(50) Zande, A. M. van der; Huang, P. Y.; Chenet, D. A.; Berkelbach, T. C.; You, Y.; Lee, G.; Heinz, T. F.; Reichman, D. R.; Muller, D. A.; Hone, J. C. Grains and Grain Boundaries in Highly Crystalline Monolayer Molybdenum Disulphide. *Nat. Mater.* **2013**, *12*, 554–561.

(51) Zhan, Y.; Liu, Z.; Najmaei, S.; Ajayan, P. M.; Lou, J. Large-Area Vapor-Phase Growth and Characterization of MoS2 Atomic Layers on a SiO2 Substrate. *Small* **2012**, *8*, 966–971.

(52) Lin, Y.-C.; Zhang, W.; Huang, J.-K.; Liu, K.-K.; Lee, Y.-H.; Liang, C.-T.; Chu, C.-W.; Li, L.-J. Wafer-Scale MoS2 Thin Layers Prepared by MoO3 Sulfurization. *Nanoscale* **2012**, *4*, 6637–6641.

(53) Liu, L.; Kumar, S. B.; Ouyang, Y.; Guo, J. Performance Limits of Monolayer Transition Metal Dichalcogenide Transistors. *IEEE Trans. Electron Devices* **2011**, *58*, 3042–3047.

(54) Yoon, Y.; Ganapathi, K.; Salahuddin, S. How Good Can Monolayer MoS_2 Transistors Be? *Nano Lett.* **2011**, *11*, 3768–3773.

(55) Wallace, P. The Band Theory of Graphite. *Phys. Rev.* **1947**, *71*, 622–634.

(56) Chen, Z.; Lin, Y. M.; Rooks, M. J.; Avouris, P. Graphene Nano-Ribbon Electronics. *Phys. E* **2007**, *40*, 228–232.

(57) Kim, K.; Choi, J.-Y.; Kim, T.; Cho, S.-H.; Chung, H.-J. A Role for Graphene in Silicon-Based Semiconductor Devices. *Nature* **2011**, *479*, 338–344.

(58) Nakada, K.; Fujita, M.; Dresselhaus, G.; Dresselhaus, M. S. Edge State in Graphene Ribbons: Nanometer Size Effect and Edge Shape Dependence. *Phys. Rev. B* **1996**, *54*, 17954–17961.

(59) Wakabayashi, K.; Fujita, M.; Ajiki, H.; Sigrist, M. Electronic and Magnetic Properties of Nanographite Ribbons. *Phys. Rev. B* **1998**, *59*, 8271–8282.

(60) Obradovic, B.; Kotlyar, R.; Heinz, F.; Matagne, P.; Rakshit, T.; Giles, M. D.; Stettler, M. A.; Nikonov, D. E. Analysis of Graphene Nanoribbons as a Channel Material for Field-Effect Transistors. *Appl. Phys. Lett.* **2006**, *88*.

(61) Jiao, L.; Wang, X.; Diankov, G.; Wang, H.; Dai, H. Facile Synthesis of High-Quality Graphene Nanoribbons. *Nat. Nanotechnol.* **2010**, *5*, 321–325.

(62) Gava, P.; Lazzeri, M.; Saitta, a.; Mauri, F. Ab Initio Study of Gap Opening and Screening Effects in Gated Bilayer Graphene. *Phys. Rev. B* **2009**, *79*, 165431.

(63) Zhang, Y.; Tang, T.-T.; Girit, C.; Hao, Z.; Martin, M. C.; Zettl, A.; Crommie, M. F.; Shen, Y. R.; Wang, F. Direct Observation of a Widely Tunable Bandgap in Bilayer Graphene. *Nature* **2009**, *459*, 820–823.

(64) Xia, F.; Farmer, D. B.; Lin, Y. M.; Avouris, P. Graphene Field-Effect Transistors with High On/off Current Ratio and Large Transport Band Gap at Room Temperature. *Nano Lett.* **2010**, *10*, 715–718.

(65) Pereira, V. M.; Castro Neto, A. H.; Peres, N. M. R. Tight-Binding Approach to

Uniaxial Strain in Graphene. *Phys. Rev. B* **2009**, *80*, 45401.

(66) Ni, Z. H. Uniaxial Strain on Graphene: Raman Spectroscopy Study and Band-Gap Opening. *ACS Nano* **2008**, *2*, 2301–2305.

(67) Nakaharai, S.; Iijima, T.; Ogawa, S.; Suzuki, S.; Tsukagoshi, K.; Sato, S.; Yokoyama, N. Electrostatically-Reversible Polarity of Dual-Gated Graphene Transistors with He Ion Irradiated Channel: Toward Reconfigurable CMOS Applications. *2012 Int. Electron Devices Meet.* **2012**, *1*, 4.2.1-4.2.4.

(68) Chen, J. H.; Jang, C.; Xiao, S.; Ishigami, M.; Fuhrer, M. S. Intrinsic and Extrinsic Performance Limits of Graphene Devices on SiO2. *Nat. Nanotechnol.* **2008**, *3*, 206–209.

(69) Chen, F.; Xia, J.; Ferry, D. K.; Tao, N. Dielectric Screening Enhanced Performance in Graphene FET. *Nano Lett.* **2009**, *9*, 2571–2574.

(70) Morozov, V. S. Giant Intrinsic Carrier Mobilities in Graphene and Its Bilayer. *Phys. Rev. Lett.* **2008**, *100*, 16602.

(71) Bolotin, K. I.; Sikes, K. J.; Jiang, Z.; Klima, M.; Fudenberg, G.; Hone, J.; Kim, P.; Stormer, H. L. Ultrahigh Electron Mobility in Suspended Graphene. *Solid State Commun.* **2008**, *146*, 351–355.

(72) Raza, H.; Kan, E. C. Armchair Graphene Nanoribbons: Electronic Structure and Electric-Field Modulation. *Phys. Rev. B* **2008**, *77*, 245434.

(73) Wang, J.; Zhao, R.; Yang, M.; Liu, Z.; Liu, Z. Inverse Relationship between Carrier Mobility and Bandgap in Graphene Inverse Relationship between Carrier Mobility and Bandgap in Graphene. **2013**, *84701*, 1–6.

(74) Meric, I.; Han, M. Y.; Young, A. F.; Ozyilmaz, B.; Kim, P. Current Saturation in Zero-Bandgap, Top-Gated Graphene Field-Effect Transistors. *Nat. Nanotechnol.* **2008**, *3*, 654–659.

(75) Shishir, R. S.; Ferry, D. K. Velocity Saturation in Intrinsic Graphene. *J. Phys. Condens. Matter* **2009**, *21*, 344201.

(76) Chauhan, J.; Guo, J. High-Field Transport and Velocity Saturation in Graphene. *Appl. Phys. Lett.* **2009**, *95*, 2007–2010.

(77) Smith, P. M.; Inoue, M.; Frey, J. Electron Velocity in Si and GaAs at Very High Electric Fields. *Appl. Phys. Lett.* **1980**, *37*, 797–798.

(78) Foutz, B. E.; O'Leary, S. K.; Shur, M. S.; Eastman, L. F. Transient Electron Transport in Wurtzite GaN, InN, and AlN. *J. Appl. Phys.* **1999**, *85*, 7727–7734.

(79) Brennan, K.; Hess, K. High Field Transport in GaAs, InP and InAs. *Solid State Electron.* **1984**, *27*, 347–357.

(80) Wilson, J. A.; Yoffe, A. D. Transition Metal Dichalcogenides: Discussion and Interpretation of Observed Optical, Electrical and Structural Properties. *Adv. Phys.* **1969**, *18*, 193–335.

(81) Chhowalla, M.; Shin, H. S.; Eda, G.; Li, L.-J.; Loh, K. P.; Zhang, H. The Chemistry of Two-Dimensional Layered Transition Metal Dichalcogenide Nanosheets. *Nat. Chem.* **2013**, *5*, 263–275.

(82) Kuc, A. Low-Dimensional Transition-Metal Dichalcogenides. In *Chemical Modelling: Volume 11*; The Royal Society of Chemistry, 2015; Vol. 11, pp. 1–29.

(83) Radisavljevic, B.; Radenovic, A.; Brivio, J.; Giacometti, V.; Kis, A. Single-Layer MoS2 Transistors. *Nat. Nanotechnol.* **2011**, *6*, 147–150.

(84) Kuc, a.; Zibouche, N.; Heine, T. Influence of Quantum Confinement on the Electronic Structure of the Transition Metal Sulfide TS2. *Phys. Rev. B* **2011**, *83*, 245213.

(85) Gutiérrez, H. R.; Perea-López, N.; Elías, A. L.; Berkdemir, A.; Wang, B.; Lv, R.; López-Urías, F.; Crespi, V. H.; Terrones, H.; Terrones, M. Extraordinary Room-Temperature Photoluminescence in Triangular WS2 Monolayers. *Nano Lett.* **2013**, *13*, 3447–3454.

(86) Chen, J.-H.; Jang, C.; Adam, S.; Fuhrer, M. S.; Williams, E. D.; Ishigami, M. Charged-Impurity Scattering in Graphene. *Nat. Phys.* **2008**, *4*, 377–381.

(87) Avouris, P.; Dimitrakopoulos, C. Graphene: Synthesis and Applications. *Mater. Today* **2012**, *15*, 86–97.

(88) Lin, Y. M. Operation of Graphene Transistors at Gigahertz Frequencies. *Nano Lett.* **2009**, *9*, 422–426.

(89) Farmer, D. B. Utilization of a Buffered Dielectric to Achieve High Field-Effect Carrier Mobility in Graphene Transistors. *Nano Lett.* **2009**, *9*, 4474–4478.

(90) Emtsev, K. V.; Bostwick, A.; Horn, K.; Jobst, J.; Kellogg, G. L.; Ley, L.; McChesney, J. L.; Ohta, T.; Reshanov, S. A.; Rohrl, J.; *et al.* Towards Wafer-Size Graphene Layers by Atmospheric Pressure Graphitization of Silicon Carbide. *Nat. Mater.* **2009**, *8*, 203–207.

(91) Lin, Y. M. 100-GHz Transistors from Wafer-Scale Epitaxial Graphene. *Science* **2010**, *327*, 662.

(92) Liao, L.; Lin, Y.-C.; Bao, M.; Cheng, R.; Bai, J.; Liu, Y.; Qu, Y.; Wang, K. L.; Huang, Y.; Duan, X. High Speed Graphene Transistors with a Self-Aligned Nanowire Gate. *Nature* **2010**, *467*, 305–308.

(93) Koswatta, S. O.; Valdes-Garcia, A.; Steiner, M. B.; Lin, Y. M.; Avouris, P. Ultimate RF Performance Potential of Carbon Electronics. *IEEE Trans. Microw. Theory Tech.* **2011**, *59*, 2739–2750.

(94) Cheng, R. High Frequency Self-Aligned Graphene Transistors with Transferred Gate Stack. *Proc. Natl Acad. Sci.* **2012**, *109*, 11588–11592.

(95) Han, S.-J.; Garcia, A. V.; Oida, S.; Jenkins, K. a; Haensch, W. Graphene Radio Frequency Receiver Integrated Circuit. *Nat. Commun.* **2014**, *5*, 3086.

(96) Mattheiss, L. F. Band Structures of Transition-Metal-Dichalcogenide Layer Compounds. *Phys. Rev. B* **1973**, *8*, 3719–3740.

(97) Das, S.; Chen, H.-Y.; Penumatcha, A. V.; Appenzeller, J. High Performance Multilayer MoS2 Transistors with Scandium Contacts. *Nano Lett.* **2012**, *13*, 100–105.

(98) Jariwala, D.; Sangwan, V. K.; Late, D. J.; Johns, J. E.; Dravid, V. P.; Marks, T. J.; Lauhon, L. J.; Hersam, M. C. Band-like Transport in High Mobility Unencapsulated

Single-Layer MoS2 Transistors. *Appl. Phys. Lett.* **2013**, *102*, 173107.

(99) Ghatak, S.; Pal, A. N.; Ghosh, A. Nature of Electronic States in Atomically Thin MoS_2 Field-Effect Transistors. *ACS Nano* **2011**, *5*, 7707–7712.

(100) Jariwala, D.; Sangwan, V. K.; Lauhon, L. J.; Marks, T. J.; Hersam, M. C. Emerging Device Applications for Semiconducting Two-Dimensional Transition Metal Dichalcogenides. *ACS Nano* **2014**, *8*, 1102–1120.

(101) Fuhrer, M. S.; Hone, J. Measurement of Mobility in Dual-Gated MoS_2 Transistors. *Nat. Nanotechnol.* **2013**, *8*, 146–147.

(102) Braga, D.; Gutiérrez Lezama, I.; Berger, H.; Morpurgo, A. F. Quantitative Determination of the Band Gap of WS2 with Ambipolar Ionic Liquid-Gated Transistors. *Nano Lett.* **2012**, *12*, 5218–5223.

(103) Radisavljevic, B.; Kis, A. Mobility Engineering and a Metal-Insulator Transition in Monolayer MoS_2. *Nat. Mater.* **2013**, *12*, 815–820.

(104) Fang, H.; Tosun, M.; Seol, G.; Chang, T. C.; Takei, K.; Guo, J.; Javey, A. Degenerate N-Doping of Few-Layer Transition Metal Dichalcogenides by Potassium. *Nano Lett.* **2013**, *13*, 1991–1995.

(105) Roy, T.; Tosun, M.; Kang, J. S.; Sachid, A. B.; Desai, S. B.; Hettick, M.; Hu, C. C.; Javey, A. Field-Effect Transistors Built from All Two-Dimensional Material Components. *ACS Nano* **2014**, *8*, 6259–6264.

(106) Chuang, H.-J.; Tan, X.; Ghimire, N. J.; Perera, M. M.; Chamlagain, B.; Cheng, M. M.-C.; Yan, J.; Mandrus, D.; Tománek, D.; Zhou, Z. High Mobility WSe2 P- and N-Type Field-Effect Transistors Contacted by Highly Doped Graphene for Low-Resistance Contacts. *Nano Lett.* **2014**, *14*, 3594–3601.

(107) Wang, S.; Wang, X.; Warner, J. H. All Chemical Vapor Deposition Growth of MoS2 :h-BN Vertical van Der Waals Heterostructures. *ACS Nano* **2015**, *9*, 5246–5254.

(108) Gong, Y.; Li, B.; Ye, G.; Yang, S.; Zou, X.; Lei, S.; Jin, Z.; Bianco, E.; Vinod, S.; Yakobson, B. I.; *et al.* Direct Growth of MoS2 Single Crystals on Polyimide Substrates. *2D Mater.* **2017**, *4*, 21028.

(109) Zhang, K.; Feng, S.; Wang, J.; Azcatl, A.; Lu, N.; Addou, R.; Wang, N.; Zhou, C.; Lerach, J.; Bojan, V.; *et al.* Manganese Doping of Monolayer MoS2: The Substrate Is Critical. *Nano Lett.* **2015**, *15*, 6586–6591.

(110) Liu, K. K.; Zhang, W.; Lee, Y. H.; Lin, Y. C.; Chang, M. T.; Su, C. Y.; Chang, C. S.; Li, H.; Shi, Y.; Zhang, H.; *et al.* Growth of Large-Area and Highly Crystalline MoS2 Thin Layers on Insulating Substrates. *Nano Lett.* **2012**, *12*, 1538–1544.

(111) Li, Y.; Wang, H.; Xie, L.; Liang, Y.; Hong, G.; Dai, H. MoS2 Nanoparticles Grown on Graphene: An Advanced Catalyst for the Hydrogen Evolution Reaction. *J. Am. Chem. Soc.* **2011**, *133*, 7296–7299.

(112) Bao, W.; Cai, X.; Kim, D.; Sridhara, K.; Fuhrer, M. S. High Mobility Ambipolar MoS2 Field-Effect Transistors: Substrate and Dielectric Effects. *Appl. Phys. Lett.* **2013**, *102*, 42104.

(113) Shi, H.; Yan, R.; Bertolazzi, S.; Brivio, J.; Gao, B.; Kis, A.; Jena, D.; Xing, H. G.; Huang, L. Exciton Dynamics in Suspended Monolayer and Few-Layer MoS2 2D Crystals. *ACS Nano* **2013**, *7*, 1072–1080.

(114) Robinson, B. J.; Giusca, C. E.; Gonzalez, Y. T.; DKay, N.; Kazakova, O.; Kolosov, O. V. Structural, Optical and Electrostatic Properties of Single and Few Layers MoS2: Effect of Substrate. *2D Mater.* **2015**, *2*, 15005.

(115) Withers, F.; Bointon, T. H.; Hudson, D. C.; Craciun, M. F.; Russo, S. Electron Transport of WS2 Transistors in a Hexagonal Boron Nitride Dielectric Environment. *Sci. Rep.* **2014**, *4*, 4967.

(116) Qiu, H.; Pan, L.; Yao, Z.; Li, J.; Shi, Y. Electrical Characterization of Back-Gated Bi-Layer MoS2 Field-Effect Transistors and the Effect of Ambient on Their Performances. *Appl. Phys. Lett.* **2012**, *100*, 123104.

(117) Ovchinnikov, D.; Allain, A.; Huang, Y. S.; Dumcenco, D.; Kis, A. Electrical Transport Properties of Single-Layer WS2. *ACS Nano* **2014**, *8*, 8174–8181.

(118) Late, D. J.; Liu, B.; Matte, H. S. S. R.; Dravid, V. P.; Rao, C. N. R. Hysteresis in Single-Layer MoS2 Field Effect Transistors. *ACS Nano* **2012**, *6*, 5635–5641.

(119) Gorbachev, R. V; Riaz, I.; Nair, R. R.; Jalil, R.; Britnell, L.; Belle, B. D.; Hill, E. W.; Novoselov, K. S.; Watanabe, K.; Taniguchi, T.; *et al.* Hunting for Monolayer Boron Nitride: Optical and Raman Signatures. *Small* **2011**, *7*, 465–468.

(120) Yang, H.; Heo, J.; Park, S.; Song, H. J.; Seo, D. H.; Byun, K.-E.; Kim, P.; Yoo, I.; Chung, H.-J.; Kim, K. Graphene Barristor, a Triode Device with a Gate-Controlled Schottky Barrier. *Science* **2012**, *336*, 1140–1143.

(121) Das, S.; Prakash, A.; Salazar, R.; Appenzeller, J. Toward Low-Power Electronics: Tunneling Phenomena in Transition Metal Dichalcogenides. *ACS Nano* **2014**, *8*, 1681–1689.

(122) Georgiou, T.; Jalil, R.; Belle, B. D.; Britnell, L.; Gorbachev, R. V; Morozov, S. V; Kim, Y.-J.; Gholinia, A.; Haigh, S. J.; Makarovsky, O.; *et al.* Vertical Field-Effect Transistor Based on Graphene-WS2 Heterostructures for Flexible and Transparent Electronics. *Nat. Nanotechnol.* **2013**, *8*, 100–103.

(123) Koppens, F. H. L.; Mueller, T.; Avouris, P.; Ferrari, A. C.; Vitiello, M. S.; Polini, M. Photodetectors Based on Graphene, Other Two-Dimensional Materials and Hybrid Systems. *Nat. Nanotechnol.* **2014**, *9*, 780–793.

(124) Bernardi, M.; Palummo, M.; Grossman, J. C. Extraordinary Sunlight Absorption and One Nanometer Thick Photovoltaics Using Two-Dimensional Monolayer Materials. *Nano Lett.* **2013**, *13*, 3664–3670.

(125) Furchi, M. M.; Polyushkin, D. K.; Pospischil, A.; Mueller, T. Mechanisms of Photoconductivity in Atomically Thin MoS2. *Nano Lett.* **2014**, *11*, 6165–6170.

(126) Buscema, M.; Barkelid, M.; Zwiller, V.; van der Zant, H. S. J.; Steele, G. A.; Castellanos-Gomez, A. Large and Tunable Photothermoelectric Effect in Single-Layer MoS2. *Nano Lett.* **2013**, *13*, 358–363.

(127) Lopez-Sanchez, O.; Lembke, D.; Kayci, M.; Radenovic, A.; Kis, A. Ultrasensitive Photodetectors Based on Monolayer MoS2. *Nat. Nanotechnol.* **2013**, *8*, 497–501.

(128) Hee Sung Lee; Min, S.-W.; Chang, Y.-G.; Park, M. K.; Nam, T.; Kim, H.; Kim, J. H.; Ryu, S.; Im, S.; Lee, S. H. MoS2 Phototransistors with Thickness-Modulated Optical Energy Gap. *Nano Lett.* **2012**, *12*, 3695–3700.

(129) Zhang, W.; Huang, J. K.; Chen, C. H.; Chang, Y. H.; Cheng, Y. J.; Li, L. J. High-Gain Phototransistors Based on a CVD MoS2 Monolayer. *Adv. Mater.* **2013**, *25*, 3456–3461.

(130) Yin, Z.; Li, H.; Li, H.; Jiang, L.; Shi, Y.; Sun, Y.; Lu, G.; Zhang, Q.; Chen, X.; Zhang, H. Single-Layer MoS2 Phototransistors. *ACS Nano* **2012**, *6*, 74–80.

(131) Kufer, D.; Konstantatos, G. Highly Sensitive, Encapsulated MoS2 Photodetector with Gate Controllable Gain and Speed. *Nano Lett.* **2015**, *15*, 7307–7313.

(132) Pospischil, A.; Furchi, M. M.; Mueller, T. Solar-Energy Conversion and Light Emission in an Atomic Monolayer P-N Diode. *Nat. Nanotechnol.* **2014**, *9*, 257–261.

(133) Baugher, B. W. H.; Churchill, H. O. H.; Yang, Y.; Jarillo-Herrero, P. Optoelectronic Devices Based on Electrically Tunable P-N Diodes in a Monolayer Dichalcogenide. *Nat. Nanotechnol.* **2014**, *9*, 262–267.

(134) Furchi, M. M.; Pospischil, A.; Libisch, F.; Burgdörfer, J.; Mueller, T. Photovoltaic Effect in an Electrically Tunable van Der Waals Heterojunction. *Nano Lett.* **2014**, *14*, 4785–4791.

(135) Lee, C.-H. H.; Lee, G.-H.; van der Zande, A. M.; Chen, W.; Li, Y.; Han, M.; Cui, X.; Arefe, G.; Nuckolls, C.; Heinz, T. F.; *et al.* Atomically Thin P-N Junctions with van Der Waals Heterointerfaces. *Nat. Nanotechnol.* **2014**, *9*, 676–681.

(136) Fontana, M.; Deppe, T.; Boyd, A. K.; Rinzan, M.; Liu, A. Y.; Paranjape, M.; Barbara, P. Electron-Hole Transport and Photovoltaic Effect in Gated MoS2 Schottky Junctions. *Sci. Rep.* **2013**, *3*, 1634.

(137) Kufer, D.; Konstantatos, G. Photo-FETs: Phototransistors Enabled by 2D and 0D Nanomaterials. *ACS Photonics* **2016**, *3*, 2197–2210.

(138) Buscema, M.; Island, J. O.; Groenendijk, D. J.; Blanter, S. I.; Steele, G. A.; van der Zant, H. S.; Castellanos-Gomez, A. Photocurrent Generation with Two-Dimensional van Der Waals Semiconductors. *Chem Soc Rev* **2015**, *44*, 3691–3718.

(139) Xie, C.; Mak, C.; Tao, X.; Yan, F. Photodetectors Based on Two-Dimensional Layered Materials Beyond Graphene. *Adv. Funct. Mater.* **2017**, *27*, 1603886.

(140) Huo, N.; Yang, S.; Wei, Z.; Li, S.-S.; Xia, J.-B.; Li, J. Photoresponsive and Gas Sensing Field-Effect Transistors Based on Multilayer WS2 Nanoflakes. *Sci. Rep.* **2014**, *4*, 5209.

(141) Perea-López, N.; Elías, A. L.; Berkdemir, A.; Castro-Beltran, A.; Gutiérrez, H. R.; Feng, S.; Lv, R.; Hayashi, T.; López-Urías, F.; Ghosh, S.; *et al.* Photosensor Device Based on Few-Layered WS2 Films. *Adv. Funct. Mater.* **2013**, *23*, 5511–5517.

(142) Lan, C.; Li, C.; Yin, Y.; Liu, Y. Large-Area Synthesis of Monolayer WS2 and Its Ambient-Sensitive Photo-Detecting Performance. *Nanoscale* **2015**, *7*, 5974–5980.

(143) Xia, J.; Huang, X.; Liu, L. Z.; Wang, M.; Wang, L.; Huang, B.; Zhu, D. D.; Li, J. J.; Gu, C. Z.; Meng, X. M. CVD Synthesis of Large-Area, Highly Crystalline MoSe2

Atomic Layers on Diverse Substrates and Application to Photodetectors. *Nanoscale* **2014**, *6*, 8949–8955.

(144) Kang, D.-H.; Kim, M.-S.; Shim, J.; Jeon, J.; Park, H.-Y.; Jung, W.-S.; Yu, H.-Y.; Pang, C.-H.; Lee, S.; Park, J.-H. High-Performance Transition Metal Dichalcogenide Photodetectors Enhanced by Self-Assembled Monolayer Doping. *Adv. Funct. Mater.* **2015**, *25*, 4219–4227.

(145) Jo, S. H.; Kang, D. H.; Shim, J.; Jeon, J.; Jeon, M. H.; Yoo, G.; Kim, J.; Lee, J.; Yeom, G. Y.; Lee, S.; *et al.* A High-Performance WSe2/h-BN Photodetector Using a Triphenylphosphine (PPh3)-Based N-Doping Technique. *Adv. Mater.* **2016**, 4824–4831.

(146) Pradhan, N.; Ludwig, J.; Lu, Z.; Rhodes, D.; Bishop, M. M.; Thirunavukkuarasu, K.; McGill, S.; Smirnov, D.; Balicas, L. High Photoresponsivity and Short Photo Response Times in Few-Layered WSe2 Transistors. *ACS Appl. Mater. Interfaces* **2015**, *7*, 12080–12088.

(147) Zhang, W.; Chiu, M. H.; Chen, C. H.; Chen, W.; Li, L. J.; Wee, A. T. S. Role of Metal Contacts in High-Performance Phototransistors Based on WSe2 Monolayers. *ACS Nano* **2014**, *8*, 8653–8661.

(148) Zhang, W.; Chuu, C.-P.; Huang, J.-K.; Chen, C.-H.; Tsai, M.-L.; Chang, Y.-H.; Liang, C.-T.; Chen, Y.-Z.; Chueh, Y.-L.; He, J.-H.; *et al.* Ultrahigh-Gain Photodetectors Based on Atomically Thin Graphene-MoS2 Heterostructures. *Sci. Rep.* **2014**, *4*, 3826.

(149) Wang, X.; Wang, P.; Wang, J.; Hu, W.; Zhou, X.; Guo, N.; Huang, H.; Sun, S.; Shen, H.; Lin, T.; *et al.* Ultrasensitive and Broadband MoS2 Photodetector Driven by Ferroelectrics. *Adv. Mater.* **2015**, *27*, 6575–6581.

(150) Pospischil, A.; Mueller, T. Optoelectronic Devices Based on Atomically Thin Transition Metal Dichalcogenides. *Appl. Sci.* **2016**, *6*, 78.

(151) Groenendijk, D. J.; Buscema, M.; Steele, G. A.; Bratschitsch, R.; Zant, H. S. J. Van Der; Castellanos-gomez, A. Photovoltaic and Photothermoelectric Effect in a Double-Gated WSe2 Device. *Nano Lett.* **2014**, *14*, 5846–5852.

(152) Buscema, M.; Groenendijk, D. J.; Steele, G. A.; van der Zant, H. S. J.; Castellanos-Gomez, A. Photovoltaic Effect in Few-Layer Black Phosphorus PN Junctions Defined by Local Electrostatic Gating. *Nat. Commun.* **2014**, *5*, 4651.

(153) Hong, X.; Kim, J.; Shi, S.-F.; Zhang, Y.; Jin, C.; Sun, Y.; Tongay, S.; Wu, J.; Zhang, Y.; Wang, F. Ultrafast Charge Transfer in Atomically Thin MoS2/WS2 Heterostructures. *Nat. Nanotechnol.* **2014**, *9*, 682–686.

(154) Ceballos, F.; Bellus, M. Z.; Chiu, H.-Y.; Zhao, H. Ultrafast Charge Separation and Indirect Exciton Formation in a MoS2–MoSe2 van Der Waals Heterostructure. *ACS Nano* **2014**, *8*, 12717–12724.

(155) Long, R.; Prezhdo, O. V. Quantum Coherence Facilitates Efficient Charge Separation at a MoS2/MoSe2 van Der Waals Junction. *Nano Lett.* **2016**, *16*, 1996–2003.

(156) Huo, N.; Kang, J.; Wei, Z.; Li, S.-S.; Li, J.; Wei, S.-H. Novel and Enhanced Optoelectronic Performances of Multilayer MoS2-WS2 Heterostructure Transistors. *Adv. Funct. Mater.* **2014**, *24*, 7025–7031.

(157) Flöry, N.; Jain, A.; Bharadwaj, P.; Parzefall, M.; Taniguchi, T.; Watanabe, K.; Novotny, L. A WSe2/MoSe2 Heterostructure Photovoltaic Device. *Appl. Phys. Lett.* **2015**, *107*, 123106.

(158) Huo, N.; Yang, J.; Huang, L.; Wei, Z.; Li, S.-S.; Wei, S.-H.; Li, J. Tunable Polarity Behavior and Self-Driven Photoswitching in P-WSe2 / N-WS2 Heterojunctions. *Small* **2015**, *11*, 5430–5438.

(159) Gong, Y.; Lin, J.; Wang, X.; Shi, G.; Lei, S.; Lin, Z.; Zou, X.; Ye, G.; Yakobson, R. V. B. I.; Terrones, H.; *et al.* Vertical and in-Plane Heterostructures from WS2/MoS2 Monolayers. *Nat. Mater.* **2014**, *13*, 1135–1142.

(160) Li, M.-Y.; Shi, Y.; Cheng, C.-C.; Lu, L.-S.; Lin, Y.-C.; Tang, H.-L.; Tsai, M.-L.; Chu, C.-W.; Wei, K.-H.; He, J.-H.; *et al.* Epitaxial Growth of a Monolayer WSe2/MoS2 Lateral P-N Junction with an Atomically Sharp Interface. *Science* **2015**, *349*, 524–529.

(161) Gong, Y.; Lei, S.; Ye, G.; Li, B.; He, Y.; Keyshar, K.; Zhang, X.; Wang, Q.; Lou, J.; Liu, Z.; *et al.* Two-Step Growth of Two-Dimensional WSe2/MoSe2 Heterostructures. *Nano Lett.* **2015**, *15*, 6135–6141.

(162) Duan, X.; Wang, C.; Shaw, J. C.; Cheng, R.; Chen, Y.; Li, H.; Wu, X.; Tang, Y.; Zhang, Q.; Pan, A.; *et al.* Lateral Epitaxial Growth of Two-Dimensional Layered Semiconductor Heterojunctions. *Nat. Nanotechnol.* **2014**, *9*, 1024–1030.

(163) Britnell, L.; Ribeiro, R. M.; Eckmann, A.; Jalil, R.; Belle, B. D.; Mishchenko, A.; Kim, Y.-J.; Gorbachev, R. V; Georgiou, T.; Morozov, S. V; *et al.* Strong Light-Matter Interactions in Heterostructures of Atomically Thin Films. *Science* **2013**, *340*, 1311–1314.

(164) Yu, W. J.; Liu, Y.; Zhou, H.; Yin, A.; Li, Z.; Huang, Y.; Duan, X. Highly Efficient Gate-Tunable Photocurrent Generation in Vertical Heterostructures of Layered Materials. *Nat. Nanotechnol.* **2013**, *8*, 952–958.

(165) Massicotte, M.; Schmidt, P.; Vialla, F.; Schädler, K. G.; Reserbat-Plantey, A.; Watanabe, K.; Taniguchi, T.; Tielrooij, K. J.; Koppens, F. H. L. Picosecond Photoresponse in van Der Waals Heterostructures. *Nat. Nanotechnol.* **2015**, *11*, 42–46.

(166) Wu, Y. A.; Fan, Y.; Speller, S.; Creeth, G. L.; Sadowski, J. T.; He, K.; Robertson, A. W.; Allen, C. S.; Warner, J. H. Large Single Crystals of Graphene on Melted Copper Using Chemical Vapor Deposition. *ACS Nano* **2012**, *6*, 5010–5017.

(167) Fan, Y.; He, K.; Tan, H.; Speller, S.; Warner, J. H. Crack-Free Growth and Transfer of Continuous Monolayer Graphene Grown on Melted Copper. *Chem. Mater.* **2014**, *26*, 4984–4991.

(168) Wang, S.; Rong, Y.; Fan, Y.; Pacios, M.; Bhaskaran, H.; He, K.; Warner, J. H. Shape Evolution of Monolayer MoS2 Crystals Grown by Chemical Vapor Deposition. *Chem. Mater.* **2014**, *26*, 6371–6379.

(169) Rong, Y.; Fan, Y.; Leen Koh, A.; Robertson, A. W.; He, K.; Wang, S.; Tan, H.; Sinclair, R.; Warner, J. H. Controlling Sulphur Precursor Addition for Large Single Crystal Domains of WS2. *Nanoscale* **2014**, *6*, 12096–12103.

(170) Sheng, Y.; Tan, H.; Wang, X.; Warner, J. H. Hydrogen Addition for Centimeter-Sized

Monolayer Tungsten Disulfide Continuous Films by Ambient Pressure Chemical Vapor Deposition. *Chem. Mater.* **2017**, *29*, 4904–4911.

(171) Kim, K. S.; Zhao, Y.; Jang, H.; Lee, S. Y.; Kim, J. M.; Kim, K. S.; Ahn, J. H.; Kim, P.; Choi, J. Y.; Hong, B. H. Large-Scale Pattern Growth of Graphene Films for Stretchable Transparent Electrodes. *Nature* **2009**, *457*, 706–710.

(172) Reina, A.; Son, H.; Jiao, L.; Fan, B.; Dresselhaus, M. S.; Liu, Z.; Kong, J. Transferring and Identification of Single- and Few-Layer Graphene on Arbitrary Substrates. *J. Phys. Chem. C* **2008**, *112*, 17741–17744.

(173) Cardinaud, C.; Peignon, M.-C.; Tessier, P.-Y. Plasma Etching: Principles, Mechanisms, Application to Micro- and Nano-Technologies. *Appl. Surf. Sci.* **2000**, *164*, 72–83.

(174) Seiler, H. Secondary Electron Emission in the Scanning Electron Microscope. *J. Appl. Phys.* **1983**, *54*, R1–R18.

(175) Li, H.; Zhang, Q.; Yap, C. C. R.; Tay, B. K.; Edwin, T. H. T.; Olivier, A.; Baillargeat, D. From Bulk to Monolayer MoS2: Evolution of Raman Scattering. *Adv. Funct. Mater.* **2012**, *22*, 1385–1390.

(176) Das, A.; Pisana, S.; Chakraborty, B.; Piscanec, S.; Saha, S. K.; Waghmare, U. V; Novoselov, K. S.; Krishnamurthy, H. R.; Geim, A. K.; Ferrari, A. C.; *et al.* Monitoring Dopants by Raman Scattering in an Electrochemically Top-Gated Graphene Transistor. *Nat. Nanotechnol.* **2008**, *3*, 210–215.

(177) Peimyoo, N.; Yang, W.; Shang, J.; Shen, X.; Wang, Y.; Yu, T. Chemically Driven Tunable Light Emission of Charged and Neutral Excitons in Monolayer WS2. *ACS Nano* **2014**, *8*, 11320–11329.

(178) Buscema, M.; Steele, G. A.; van der Zant, H. S. J.; Castellanos-Gomez, A. The Effect of the Substrate on the Raman and Photoluminescence Emission of Single-Layer MoS2. *Nano Res.* **2014**, *7*, 1–11.

(179) Mlack, J. T.; Masih Das, P.; Danda, G.; Chou, Y. C.; Naylor, C. H.; Lin, Z.; López, N. P.; Zhang, T.; Terrones, M.; Johnson, A. T. C.; *et al.* Transfer of Monolayer TMD WS 2 and Raman Study of Substrate Effects. *Sci. Rep.* **2017**, *7*, 1–8.

(180) Rice, C.; Young, R. J.; Zan, R.; Bangert, U.; Wolverson, D.; Georgiou, T.; Jalil, R.; Novoselov, K. S. Raman-Scattering Measurements and First-Principles Calculations of Strain-Induced Phonon Shifts in Monolayer MoS2. *Phys. Rev. B* **2013**, *87*, 1–5.

(181) Ferrari, A. C.; Meyer, J. C.; Scardaci, V.; Casiraghi, C.; Lazzeri, M.; Mauri, F.; Piscanec, S.; Jiang, D.; Novoselov, K. S.; Roth, S.; *et al.* Raman Spectrum of Graphene and Graphene Layers. *Phys. Rev. Lett.* **2006**, *97*, 187401.

(182) Berkdemir, A.; Gutiérrez, H. R.; Botello-Méndez, A. R.; Perea-López, N.; Elías, A. L.; Chia, C.-I.; Wang, B.; Crespi, V. H.; López-Urías, F.; Charlier, J.-C.; *et al.* Identification of Individual and Few Layers of WS2 Using Raman Spectroscopy. *Sci. Rep.* **2013**, *3*, 1755.

(183) Mitioglu, A. A.; Plochocka, P.; Deligeorgis, G.; Anghel, S.; Kulyuk, L.; Maude, D. K. Second-Order Resonant Raman Scattering in Single-Layer Tungsten Disulfide WS2. *Phys. Rev. B - Condens. Matter Mater. Phys.* **2014**, *89*, 1–5.

(184) Molina-Sánchez, A.; Wirtz, L. Phonons in Single-Layer and Few-Layer MoS2 and WS2. *Phys. Rev. B - Condens. Matter Mater. Phys.* **2011**, *84*, 1–8.

(185) Peimyoo, N.; Shang, J.; Yang, W.; Wang, Y.; Cong, C.; Yu, T. Thermal Conductivity Determination of Suspended Mono- and Bilayer WS2 by Raman Spectroscopy. *Nano Res.* **2015**, *8*, 1210–1221.

(186) Zhang, J.; Wang, J.; Chen, P.; Sun, Y.; Wu, S.; Jia, Z.; Lu, X.; Yu, H.; Chen, W.; Zhu, J.; *et al.* Observation of Strong Interlayer Coupling in MoS2/WS2 Heterostructures. *Adv. Mater.* **2016**, *28*, 1950–1956.

(187) Zhou, K.; Withers, F.; Cao, Y.; Hu, S.; Yu, G.; Casiraghi, C. Raman Modes of MoS2 Used as Fingerprint of van Der Waals Interactions in 2D Crystal-Based Heterostructures. *ACS Nano* **2014**, *8*, 9914–9924.

(188) Zhao, W.; Ghorannevis, Z.; Amara, K. K.; Pang, J. R.; Toh, M.; Zhang, X.; Kloc, C.; Tan, P. H.; Eda, G. Lattice Dynamics in Mono- and Few-Layer Sheets of WS2 and WSe2. *Nanoscale* **2013**, *5*, 9677.

(189) Binnig, G.; Quate, C. F. Atomic Force Microscope. *Phys. Rev. Lett.* **1986**, *56*, 930–933.

(190) Meyer, E. Atomic Force Microscopy. *Prog. Surf. Sci.* **1992**, *41*, 3–49.

(191) Giessibl, F. J. Advances in Atomic Force Microscopy. *Rev. Mod. Phys.* **2003**, *75*, 949–983.

(192) Britnell, L.; Gorbachev, R. V; Jalil, R.; Belle, B. D.; Schedin, F.; Mishchenko, A.; Georgiou, T.; Katsnelson, M. I.; Eaves, L.; Morozov, S. V; *et al.* Field-Effect Tunneling Transistor Based on Vertical Graphene Heterostructures. *Science* **2012**, *335*, 947–950.

(193) Loan, P. T. K.; Zhang, W.; Lin, C.-T.; Wei, K.-H.; Li, L.-J.; Chen, C.-H. Graphene/MoS2 Heterostructures for Ultrasensitive Detection of DNA Hybridisation. *Adv. Mater.* **2014**, *26*, 4838–4844.

(194) Roy, K.; Padmanabhan, M.; Goswami, S.; Sai, T. P.; Ramalingam, G.; Raghavan, S.; Ghosh, A. Graphene-MoS2 Hybrid Structures for Multifunctional Photoresponsive Memory Devices. *Nat. Nanotechnol.* **2013**, *8*, 826–830.

(195) Huo, N.; Wei, Z.; Meng, X.; Kang, J.; Wu, F.; Li, S.-S.; Wei, S.-H.; Li, J. Interlayer Coupling and Optoelectronic Properties of Ultrathin Two-Dimensional Heterostructures Based on Graphene, MoS2 and WS2. *J. Mater. Chem. C* **2015**, *3*, 5467–5473.

(196) Rathi, S.; Lee, I.; Lim, D.; Wang, J.; Ochiai, Y.; Aoki, N.; Watanabe, K.; Taniguchi, T.; Lee, G.-H.; Yu, Y.-J.; *et al.* Tunable Electrical and Optical Characteristics in Monolayer Graphene and Few-Layer MoS2 Heterostructure Devices. *Nano Lett.* **2015**, *15*, 5017–5024.

(197) Williams, J. R.; Dicarlo, L.; Marcus, C. M. Quantum Hall Effect in a Gate-Controlled P-N Junction of Graphene. *Science* **2007**, *317*, 638–641.

(198) Özyilmaz, B.; Jarillo-Herrero, P.; Efetov, D.; Abanin, D. a.; Levitov, L. S.; Kim, P. Electronic Transport and Quantum Hall Effect in Bipolar Graphene P-N-P Junctions. *Phys. Rev. Lett.* **2007**, *99*, 2–5.

(199) Chiu, H.-Y. Y.; Perebeinos, V.; Lin, Y.-M. M.; Avouris, P. Controllable P-N Junction Formation in Monolayer Graphene Using Electrostatic Substrate Engineering. *Nano Lett.* **2010**, *10*, 4634–4639.

(200) Wang, X.; Jiang, X.; Wang, T.; Shi, J.; Liu, M.; Zeng, Q.; Cheng, Z.; Qiu, X. Electrically Configurable Graphene Field-Effect Transistors with a Graded-Potential Gate. *Nano Lett.* **2015**, *15*, 3212–3216.

(201) Brenner, K.; Murali, R. Single Step, Complementary Doping of Graphene. *Appl. Phys. Lett.* **2010**, *96*, 2009–2011.

(202) Usachov, D.; Vilkov, O.; Grüneis, A.; Haberer, D.; Fedorov, A.; Adamchuk, V. K.; Preobrajenski, A. B.; Dudin, P.; Barinov, A.; Oehzelt, M.; *et al.* Nitrogen-Doped Graphene: Efficient Growth, Structure, and Electronic Properties. *Nano Lett.* **2011**, *11*, 5401–5407.

(203) Xiang, D.; Han, C.; Wu, J.; Zhong, S.; Liu, Y.; Lin, J.; Zhang, X.-A.; Ping Hu, W.; Özyilmaz, B.; Neto, A. H. C.; *et al.* Surface Transfer Doping Induced Effective Modulation on Ambipolar Characteristics of Few-Layer Black Phosphorus. *Nat. Commun.* **2015**, *6*, 6485.

(204) Lemme, M. C.; Koppens, F. H. L.; Falk, A. L.; Rudner, M. S.; Park, H.; Levitov, L. S.; Marcus, C. M. Gate-Activated Photoresponse in a Graphene P-N Junction. *Nano Lett.* **2011**, *11*, 4134–4137.

(205) Sun, D.; Aivazian, G.; Jones, A. M.; Ross, J. S.; Yao, W.; Cobden, D.; Xu, X. Ultrafast Hot-Carrier-Dominated Photocurrent in Graphene. *Nat. Nanotechnol.* **2012**, *7*, 114–118.

(206) Freitag, M.; Low, T.; Xia, F.; Avouris, P. Photoconductivity of Biased Graphene. *Nat. Photonics* **2012**, *7*, 53–59.

(207) Liu, N.; Tian, H.; Schwartz, G.; Tok, J. B.-H. H.; Ren, T.-L. L.; Bao, Z. Large-Area, Transparent, and Flexible Infrared Photodetector Fabricated Using P-N Junctions Formed by N-Doping Chemical Vapor Deposition Grown Graphene. *Nano Lett.* **2014**, *14*, 3702–3708.

(208) Rong, Y.; He, K.; Pacios, M.; Robertson, A. W.; Bhaskaran, H.; Warner, J. H. Controlled Preferential Oxidation of Grain Boundaries in Monolayer Tungsten Disulfide for Direct Optical Imaging. *ACS Nano* **2015**, *9*, 3695–3703.

(209) Bhanu, U.; Islam, M. R.; Tetard, L.; Khondaker, S. I. Photoluminescence Quenching in Gold - MoS2 Hybrid Nanoflakes. *Sci. Rep.* **2014**, *4*, 5575.

(210) Chernikov, A.; Berkelbach, T. C.; Hill, H. M.; Rigosi, A.; Li, Y.; Aslan, O. B.; Reichman, D. R.; Hybertsen, M. S.; Heinz, T. F. Exciton Binding Energy and Nonhydrogenic Rydberg Series in Monolayer WS2. *Phys. Rev. Lett.* **2014**, *113*, 76802.

(211) Mitioglu, A.; Plochocka, P.; Jadczak, J.; Escoffier, W.; Rikken, G.; Kulyuk, L.; Maude, D. Optical Manipulation of the Exciton Charge State in Single-Layer Tungsten Disulfide. *Phys. Rev. B* **2013**, *88*, 245403.

(212) Zhu, B.; Chen, X.; Cui, X. Exciton Binding Energy of Monolayer WS2. *Sci. Rep.* **2014**, *5*, 9218.

(213) Nistor, R. A.; Kuroda, M. A.; Maarouf, A. A.; Martyna, G. J. Doping of Adsorbed

Graphene from Defects and Impurities in SiO2 Substrates. *Phys. Rev. B - Condens. Matter Mater. Phys.* **2012**, *86*, 1–5.

(214) Kretinin, A. V.; Cao, Y.; Tu, J. S.; Yu, G. L.; Jalil, R.; Novoselov, K. S.; Haigh, S. J.; Gholinia, A.; Mishchenko, A.; Lozada, M.; *et al.* Electronic Properties of Graphene Encapsulated with Different Two-Dimensional Atomic Crystals. *Nano Lett.* **2014**, *14*, 3270–3276.

(215) Haigh, S. J.; Gholinia, A.; Jalil, R.; Romani, S.; Britnell, L.; Elias, D. C.; Novoselov, K. S.; Ponomarenko, L. A.; Geim, A. K.; Gorbachev, R. Cross-Sectional Imaging of Individual Layers and Buried Interfaces of Graphene-Based Heterostructures and Superlattices. *Nat. Mater.* **2012**, *11*, 764–767.

(216) Wang, W.; Liu, Y.; Tang, L.; Jin, Y.; Zhao, T.; Xiu, F. Controllable Schottky Barriers between MoS2 and Permalloy. *Sci. Rep.* **2014**, *4*, 6928.

(217) Allain, A.; Kang, J.; Banerjee, K.; Kis, A. Electrical Contacts to Two-Dimensional Semiconductors. *Nat. Mater.* **2015**, *14*, 1195–1205.

(218) Yu, L.; Lee, Y. H.; Ling, X.; Santos, E. J. G.; Shin, Y. C.; Lin, Y.; Dubey, M.; Kaxiras, E.; Kong, J.; Wang, H.; *et al.* Graphene/MoS2 Hybrid Technology for Large-Scale Two-Dimensional Electronics. *Nano Lett.* **2014**, *14*, 3055–3063.

(219) Mcdonnell, S.; Addou, R.; Buie, C.; Wallace, R. M.; Hinkle, C. L. Defect-Dominated Doping and Contact Resistance in MoS2. *ACS Nano* **2014**, *8*, 2880–2888.

(220) Shih, C. J.; Wang, Q. H.; Son, Y.; Jin, Z.; Blankschtein, D.; Strano, M. S. Tuning on-off Current Ratio and Field-Effect Mobility in a MoS2-Graphene Heterostructure via Schottky Barrier Modulation. *ACS Nano* **2014**, *8*, 5790–5798.

(221) Liu, Y.; Wu, H.; Cheng, H. C.; Yang, S.; Zhu, E.; He, Q.; Ding, M.; Li, D.; Guo, J.; Weiss, N. O.; *et al.* Toward Barrier Free Contact to Molybdenum Disulfide Using Graphene Electrodes. *Nano Lett.* **2015**, *15*, 3030–3034.

(222) Yu, Y.-J.; Zhao, Y.; Ryu, S.; Brus, L. E.; Kim, K. S.; Kim, P. Tuning the Graphene Work Function by Electric Field Effect. *Nano Lett.* **2009**, *9*, 3430–3434.

(223) Chen, W.; Chen, S.; Qi, D. C.; Gao, X. Y.; Wee, A. T. S. Surface Transfer P-Type Doping of Epitaxial Graphene. *J. Am. Chem. Soc.* **2007**, *129*, 10418–10422.

(224) Konstantatos, G.; Badioli, M.; Gaudreau, L.; Osmond, J.; Bernechea, M.; de Arquer, F. P. G.; Gatti, F.; Koppens, F. H. L. Hybrid Graphene-Quantum Dot Phototransistors with Ultrahigh Gain. *Nat Nano* **2012**, *7*, 363–368.

(225) Ju, L.; Velasco, J.; Huang, E.; Kahn, S.; Nosiglia, C.; Tsai, H.-Z.; Yang, W.; Taniguchi, T.; Watanabe, K.; Zhang, Y.; *et al.* Photoinduced Doping in Heterostructures of Graphene and Boron Nitride. *Nat. Nanotechnol.* **2014**, *9*, 348–352.

(226) Tan, H.; Fan, Y.; Rong, Y.; Porter, B.; Lau, C. S.; Zhou, Y.; He, Z.; Wang, S.; Bhaskaran, H.; Warner, J. H. Doping Graphene Transistors Using Vertical Stacked Monolayer WS2 Heterostructures Grown by Chemical Vapor Deposition. *ACS Appl. Mater. Interfaces* **2016**, *8*, 1644–1652.

(227) Zeng, H.; Liu, G.-B.; Dai, J.; Yan, Y.; Zhu, B.; He, R.; Xie, L.; Xu, S.; Chen, X.; Yao, W.; *et al.* Optical Signature of Symmetry Variations and Spin-Valley Coupling in

Atomically Thin Tungsten Dichalcogenides. *Sci. Rep.* **2013**, *3*, 1608.

(228) He, Z.; Xu, W.; Zhou, Y.; Wang, X.; Sheng, Y.; Rong, Y.; Guo, S.; Zhang, J.; Smith, J. M.; Warner, J. H. Biexciton Formation in Bilayer Tungsten Disulfide. *ACS Nano* **2016**, *10*, 2176–2183.

(229) Blanter, Y. M.; Büttiker, M. Shot Noise in Mesoscopic Conductors. *Phys. Rep.* **2000**, *336*, 1–166.

(230) Frahm, R.; Mautner, P.; Wilhelm, W. Evidence That Similar Point Defects Cause I/f Noise and Radiation-Induced-Hole Trapping in Metal-Oxide-Semiconductor Transistors. *Phys. Rev. Lett.* **1990**, *64*, 579–582.

(231) Choi, W.; Cho, M. Y.; Konar, A.; Lee, J. H.; Cha, G. B.; Hong, S. C.; Kim, S.; Kim, J.; Jena, D.; Joo, J.; *et al.* High-Detectivity Multilayer MoS2 Phototransistors with Spectral Response from Ultraviolet to Infrared. *Adv. Mater.* **2012**, *24*, 5832–5836.

(232) Renteria, J.; Samnakay, R.; Rumyantsev, S. L.; Jiang, C.; Samnakay, R.; Shur, M. S.; Balandin, A. A. Low-Frequency 1 / F Noise in MoS2 Thin-Film Transistors : Comparison of Single and Multilayer Structures. *Appl. Phys. Lett.* **2014**, *104*, 153104.

(233) Kwon, H.; Kang, H.; Jang, J.; Kim, S.; Grigoropoulos, C. P.; Kwon, H.; Kang, H.; Jang, J.; Kim, S. Analysis of Flicker Noise in Two-Dimensional Multilayer MoS2 Transistors. *Appl. Phys. Lett.* **2014**, *104*, 83110.

(234) Tsai, D.-S.; Liu, K.-K.; Lien, D.-H.; Tsai, M.-L.; Kang, C.-F.; Lin, C.-A.; Li, L.-J.; He, J.-H. Few Layer MoS2 with Broadband High Photogain and Fast Optical Switching for Use in Harsh Environments. *ACS Nano* **2013**, 3905–3911.

(235) Abderrahmane, A.; Ko, P. J.; Thu, T. V; Ishizawa, S.; Takamura, T.; Sandhu, A. High Photosensitivity Few-Layered MoSe2 Back-Gated Field-Effect Phototransistors. *Nanotechnology* **2014**, *25*, 365202.

(236) Tian, H.; Tan, Z.; Wu, C.; Wang, X.; Mohammad, M. A.; Xie, D.; Yang, Y.; Wang, J.; Li, L.-J.; Xu, J.; *et al.* Novel Field-Effect Schottky Barrier Transistors Based on Graphene-MoS2 Heterojunctions. *Sci. Rep.* **2014**, *4*, 5951.

(237) Chiquito, A. J.; Amorim, C. A.; Berengue, O. M.; Araujo, L. S.; Bernardo, E. P.; Leite, E. R. Back-to-Back Schottky Diodes: The Generalization of the Diode Theory in Analysis and Extraction of Electrical Parameters of Nanodevices. *J. Phys. Condens. Matter* **2012**, *24*, 225303.

(238) Ohta, Y.; Kubozono, Y.; Fujiwara, A. Transport Properties in C60 Field-Effect Transistor with a Single Schottky Barrier. *Appl. Phys. Lett.* **2008**, *92*, 1–4.

(239) Fan, Y.; Zhou, Y.; Wang, X.; Tan, H.; Rong, Y.; Warner, J. H. Photoinduced Schottky Barrier Lowering in 2D Monolayer WS_2 Photodetectors. *Adv. Opt. Mater.* **2016**, *4*, 1573–1581.

(240) Liu, W.; Sarkar, D.; Kang, J.; Cao, W.; Banerjee, K. Impact of Contact on the Operation and Performance of Back-Gated Monolayer MoS2 Field-Effect-Transistors. *ACS Nano* **2015**, *9*, 7904–7912.

(241) Anwar, A.; Nabet, B.; Culp, J.; Castro, F.; Anwar, A.; Nabet, B.; Culp, J.; Castro, F. Effects of Electron Confinement on Thermionic Emission Current in a Modulation Doped Heterostructure. *J. Appl. Phys.* **1999**, *85*, 2663.

(242) Yamaguchi, T.; Moriya, R.; Inoue, Y.; Morikawa, S.; Masubuchi, S.; Watanabe, K.; Taniguchi, T.; Machida, T. Tunneling Transport in a Few Monolayer-Thick WS2/graphene Heterojunction. *Appl. Phys. Lett.* **2014**, *105*, 223109.

(243) Chen, H.; Wen, X.; Zhang, J.; Wu, T.; Gong, Y.; Zhang, X.; Yuan, J.; Yi, C.; Lou, J.; Ajayan, P. M.; *et al.* Ultrafast Formation of Interlayer Hot Excitons in Atomically Thin MoS2/WS2 Heterostructures. *Nat. Commun.* **2016**, *7*, 12512.

(244) Rivera, P.; Schaibley, J. R.; Jones, A. M.; Ross, J. S.; Wu, S.; Aivazian, G.; Klement, P.; Seyler, K.; Clark, G.; Ghimire, N. J.; *et al.* Observation of Long-Lived Interlayer Excitons in Monolayer MoSe2–WSe2 Heterostructures. *Nat. Commun.* **2015**, *6*, 6242.

(245) Yuan, J.; Najmaei, S.; Zhang, Z.; Zhang, J.; Lei, S.; M Ajayan, P.; Yakobson, B. I.; Lou, J. Photoluminescence Quenching and Charge Transfer in Artificial Heterostacks of Monolayer Transition Metal Dichalcogenides and Few-Layer Black Phosphorus. *ACS Nano* **2015**, *9*, 555–563.

(246) Fang, H.; Battaglia, C.; Carraro, C.; Nemsak, S.; Ozdol, B.; Kang, J. S.; Bechtel, H. A.; Desai, S. B.; Kronast, F.; Unal, A. A.; *et al.* Strong Interlayer Coupling in van Der Waals Heterostructures Built from Single-Layer Chalcogenides. *Proc. Nati. Acad. Sci. Usa* **2014**, *111*, 6198–6202.

(247) Tongay, S.; Fan, W.; Kang, J.; Park, J.; Koldemir, U.; Suh, J.; Narang, D. S.; Liu, K.; Ji, J.; Li, J.; *et al.* Tuning Interlayer Coupling in Large-Area Heterostructures with CVD-Grown MoS2 and WS2 Monolayers. *Nano Lett.* **2014**, *14*, 3185–3190.

(248) Palummo, M.; Bernardi, M.; Grossman, C.; Grossman, J. C. Exciton Radiative Lifetimes in Two-Dimensional Transition Metal Dichalcogenides. *Nano Lett.* **2015**, *15*, 2794–2800.

(249) Withers, F.; Del Pozo-Zamudio, O.; Mishchenko, A.; Rooney, A. P.; Gholinia, A.; Watanabe, K.; Taniguchi, T.; Haigh, S. J.; Geim, A. K.; Tartakovskii, A. I.; *et al.* Light-Emitting Diodes by Band-Structure Engineering in van Der Waals Heterostructures. *Nat Mater* **2015**, *14*, 301–306.

(250) Liu, F.; Shimotani, H.; Shang, H.; Kanagasekaran, T.; Zo, V.; Drummond, N.; Fal, V. I.; La, L.; Kingdom, U.; Zólyomi, V.; *et al.* High-Sensitivity Photodetectors Based on Multilayer GaTe Flakes. *ACS Nano* **2014**, *8*, 752–760.

(251) Chen, J.; Liu, B.; Liu, Y.; Tang, W.; Nai, C. T.; Li, L.; Zheng, J.; Gao, L.; Zheng, Y.; Shin, H. S.; *et al.* Chemical Vapor Deposition of Large-Sized Hexagonal WSe2 Crystals on Dielectric Substrates. *Adv. Mater.* **2015**, *27*, 6722–6727.

(252) Tan, H.; Fan, Y.; Zhou, Y.; Chen, Q.; Xu, W.; Warner, J. H. Ultrathin 2D Photodetectors Utilizing Chemical Vapor Deposition Grown WS2 With Graphene Electrodes. *ACS Nano* **2016**, *10*, 7866–7873.

(253) Hill, H. M.; Rigosi, A. F.; Rim, K. T.; Flynn, G. W.; Heinz, T. F. Band Alignment in MoS2/WS2 Transition Metal Dichalcogenide Heterostructures Probed by Scanning Tunneling Microscopy and Spectroscopy. *Nano Lett.* **2016**, *16*, 4831–4837.

(254) Fiori, G.; Bonaccorso, F.; Iannaccone, G.; Palacios, T.; Neumaier, D.; Seabaugh, A.; Banerjee, S. K.; Colombo, L. Electronics Based on Two-Dimensional Materials. *Nat. Nanotechnol.* **2014**, *9*, 768–779.

(255) Xiao, X.; Li, Y.; Liu, Z. Graphene Commercialization. *Nat. Mater.* **2016**, *15*, 697–

698.

(256) Novoselov, K. S.; Fal'ko, V. I.; Colombo, L.; Gellert, P. R.; Schwab, M. G.; Kim, K. A Roadmap for Graphene. *Nature* **2012**, *490*, 192–200.

(257) Ferrari, A. C.; Bonaccorso, F.; Fal'ko, V.; Novoselov, K. S.; Roche, S.; Bøggild, P.; Borini, S.; Koppens, F. H. L.; Palermo, V.; Pugno, N.; *et al.* Science and Technology Roadmap for Graphene, Related Two-Dimensional Crystals, and Hybrid Systems. *Nanoscale* **2015**, *7*, 4598–4810.

(258) Neves, A. I. S.; Bointon, T. H.; Melo, L. V.; Russo, S.; De Schrijver, I.; Craciun, M. F.; Alves, H. Transparent Conductive Graphene Textile Fibers. *Sci. Rep.* **2015**, *5*, 1–7.

(259) Kim, J. A.; Hwang, T.; Dugasani, S. R.; Amin, R.; Kulkarni, A.; Park, S. H.; Kim, T. Graphene Based Fiber Optic Surface Plasmon Resonance for Bio-Chemical Sensor Applications. *Sensors Actuators, B Chem.* **2013**, *187*, 426–433.

(260) Zhang, Y.; Zhang, H.; Li, F.; Shu, H.; Chen, Z.; Sui, Y.; Zhang, Y.; Ge, X.; Yu, G.; Jin, Z.; *et al.* Invisible Growth of Microstructural Defects in Graphene Chemical Vapor Deposition on Copper Foil. *Carbon N. Y.* **2016**, *96*, 237–242.

(261) Ambrosi, A.; Pumera, M. The CVD Graphene Transfer Procedure Introduces Metallic Impurities Which Alter the Graphene Electrochemical Properties. *Nanoscale* **2014**, *6*, 472–476.

(262) Wang, H.; Wu, Y.; Cong, C.; Shang, J.; Yu, T. Hysteresis of Electronic Transport in Graphene Transistors. *ACS Nano* **2010**, *4*, 13.

(263) He, Z.; Wang, X.; Xu, W.; Zhou, Y.; Sheng, Y.; Rong, Y.; Smith, J. M.; Warner, J. H. Revealing Defect-State Photoluminescence in Monolayer WS2 by Cryogenic Laser Processing. *ACS Nano* **2016**, *10*, 5847–5855.